ANKARA YILDIRIM BEYAZIT UNIVERSITY

GRADUATE SCHOOL OF NATURAL AND APPLIED SCIENCES



SYNTHESIS OF ALUMINUM BORATE POWDER, FABRICATION AND CHARACTERIZATION OF ALUMINUM BORATE-BASED CERAMICS

M. Sc. Thesis by

Başak ÖZGÜR

Department of Materials Engineering

April, 2022

ANKARA

SYNTHESIS OF ALUMINUM BORATE POWDER, FABRICATION AND CHARACTERIZATION OF ALUMINUM BORATE-BASED CERAMICS

A Thesis Submitted to
The Graduate School of Natural and Applied Sciences of Ankara Yıldırım Beyazıt University

In Partial Fulfillment of the Requirements for the Degree of Master of Science in Department of Materials Engineering

by

Başak ÖZGÜR

April, 2022

ANKARA

M. Sc. THESIS EXAMINATION RESULT FORM

We have read the thesis entitled **"SYNTHESIS OF ALUMINUM BORATE POWDER, FABRICATION AND CHARACTERIZATION OF ALUMINUM BORATE-BASED CERAMICS"** completed by **BAŞAK ÖZGÜR** under supervision of **PROF. DR. CİHANGIR DURAN** and we certify that in our opinion it is fully adequate, in scope and in quality, as a thesis for the degree of Master of Science.

Prof. Dr. Cihangir DURAN

Supervisor

Prof. Dr. Hüseyin YILMAZ

Jury Member

Doç. Dr. Gülsüm TOPATEŞ

Jury Member

Prof. Dr. Sadettin ORHAN

Director

Graduate School of Natural and Applied Sciences

ETHICAL DECLARATION

I hereby declare that, in this thesis, which has been prepared in accordance with the Thesis Writing Manual of Graduate School of Natural and Applied Sciences,

- All data, information, and documents were obtained in the framework of academic and ethical rules,
- All information, documents, and assessments are presented in accordance with scientific ethics and morals,
- All of the materials that have been utilized are fully cited and referenced,
- No changes have been made in the utilized materials,
- All of the work presented is original,

and in any contrary case of the above statements, I agree to renounce all of my legal rights.

Date: 27/04/2022 **Signature:**

Name & Surname: Başak ÖZGÜR

ACKNOWLEDGMENTS

Firstly, I would like to express my deepest gratitude to my supervisor Prof. Dr. Cihangir Duran who contributed in making this project possible with his valuable guidance, support and advice. I am thankful for his constructive comments and kind help.

I would like to thank to Oğuzhan Bilaç and Melike Dönmez for their supports during my experiments.

I am also very thankful for Ankara Yildirim Beyazit University for the BAP project FYL-2020-2043.

Last, but not at least, I wish to thank my mother İnci Özgür and my father Ercan Özgür for supporting and encouraging me all the way.

2022, 27 April **Başak ÖZGÜR**

SYNTHESIS OF ALUMINUM BORATE POWDER, FABRICATION AND CHARACTERIZATION OF ALUMINUM BORATE-BASED CERAMICS

ABSTRACT

Aluminum borate is a suitable ceramic for structural applications due to its low thermal expansion coefficient (4.5×10^{-6}/°C), high elastic modulus (400 GPa), low density (2.93 gr/cm^3). In particular, it is used as thermal insulator due to its low thermal conductivity (4 - 6 W/m.K up to 1000°C). However, its acicular particle shape makes densification difficult during sintering. In this thesis, Al_2O_3 and domestic B_2O_3 source were utilized to synthetize $Al_{18}B_4O_{33}$ powders by solid state calcination technique and then basic characterizations (phase formation, microstructural evolution, mechanical, thermal, dielectric properties) were completed. Seven formulations (10.7, 13.4, 18.1, 27.9, 34.4, 44, 54.1 wt% B_2O_3) were prepared and then calcined at 1300°C for 1h to synthesize $Al_{18}B_4O_{33}$ powders. Full $Al_{18}B_4O_{33}$ formation was obtained at 44 wt% B_2O_3 (e.g., rather than the stoichiometric ratio of 13.17 wt% B_2O_3). Our results show that 44 wt% B_2O_3 (e.g., Al_2O_3/ B_2O_3 mole ratio of 0.87) was required to obtain a melt that was required to induce nucleation or crystallization of $Al_{18}B_4O_{33}$ phase at calcination temperatures ≥1200°C. Acicular $Al_{18}B_4O_{33}$ particles were fully obtained for the 44 wt% and 54.1 wt% B_2O_3 mixtures when Al_2O_3 was all consumed. However, its acicular particle shape made densification difficult during sintering. Therefore, its densification was controlled by a composite approach with mullite due to its similar crystal structure. $Al_{18}B_4O_{33}$+2 wt% CaO (named as AB), %100 $Al_{18}B_4O_{33}$ (named as PAB), %35 $Al_{18}B_4O_{33}$+%35 mullite+%30 glass composite (named as AMG) and %70 $Al_{18}B_4O_{33}$ +%30 glass composite (named as ABG) were prepared by gel casting method. Glass and CaO were added to enhance densification by means of a liquid phase sintering mechanism. The PAB sample sintered at 1350°C for 1h had a relative density of 59.7 %, but 2 wt% CaO addition improved densification to 95.4% (the AB sample). The AMG ceramics reached 94.8% relative density with near-zero open porosity and water absorption levels. The ABG ceramics reached a limited densification of 89.4%. Dielectric constant of the samples varied between the 4 and 6.6 at 5 MHz. The PAB ceramic had the lowest (4.05) and the ABG ceramic had the highest value (6.58) dielectric constant. Vickers hardness values were 924±118 for the AMG, 998±52 for

the AB, 825±120 for the ABG and 98 ±10 for the PAB ceramics. The AB sample had a thermal conductivity of 7.26 W/m.K but the PAB sample had 2.7 W/m.K due to its low densification. The crystalline phases (e.g., $Al_{18}B_4O_{33}$ and/or mullite) were embraced by amorphous glassy phase, which caused a sharp decrease in overall thermal conductivity (1.73 W/m.K) of the AMG and ABG composites. In this study, Al borate-glass (AB) and Al borate-mullite-glass (AMG) composites were investigated for the first time in literature. The ABG ceramics reached a limited densification of 89.4% due to insufficient filling of glass phase thru the porous network, but the AMG ceramics reached 94.8% relative density with near-zero open porosity and water absorption levels due to mullite addition. These results suggest that Al borate-based ceramics can be used for such applications as reinforcement material in metal matrix composites, filter, thermal insulator, substrate and radome materials.

Keywords: Al borate powder synthesis, densification, dielectric properties, mechanical properties, thermal properties.

ALÜMİNYUM BORAT TOZLARININ SENTEZLENMESİ, ALÜMİNYUM BORAT ESASLI SERAMİKLERİN ÜRETİLMESİ VE KARAKTERİZASYONLARI

ÖZ

Alüminyum borat sahip olduğu düşük ısısal genleşme katsayısı (4.5×10^{-6}/°C), yüksek elastik modülü (400 GPa) ve düşük yoğunluk (2.93 gr/cm^3) özelliklerinden dolayı yapısal uygulamalar için uygun bir seramiktir. Bilhassa, sahip olduğu düşük termal iletkenlik değerinden dolayı (1000°C'e kadar 4 - 6 W/m.K) termal yalıtkan olarak kullanılmaktadır. Ancak, sahip olduğu iğnesel partikül şekli sinterleme esnasında yoğunlaşmayı zorlaştırmaktadır. Bu tez çalışmasında, Al_2O_3 and yerli B_2O_3 kaynakları kullanılarak katı hal methodu ile $Al_{18}B_4O_{33}$ tozu sentezlenmiş ve sonrasında temel karakterizasyonlar (faz oluşumu, mikroyapı gelişimi, mekanik, termal, dielektrik özellikler) tamamlanmıştır., 7 farklı kompozisyon (ağırlıkça %10.7, %13.4, %18.1, %27.9, %34.4, %44, %54.1 B_2O_3) hazırlanmış ve daha sonra $Al_{18}B_4O_{33}$ tozlarını sentezlemek için 1300°C'de 1 saat kalsine edilmişlerdir. Tam $Al_{18}B_4O_{33}$ oluşumu ağırlıkça %44 B_2O_3 oranında (sitokiyometrik oran olan ağırlıkça %13.17 B_2O_3'den farklı olarak) elde edilmiştir. Elde edilen sonuçlar, 1200°C ve üstü kalsinasyon sıcaklıklarında $Al_{18}B_4O_{33}$ kristalleşmesi ya da çekirdeklenmesini başlatmak için ağırlıkça %44 oranında B_2O_3 (yada, Al_2O_3/B_2O_3 mol oranı 0.87) ihtiva eden bir eriyiğin gerekli olduğunu göstermiştir. İğnesel $Al_{18}B_4O_{33}$ partikülleri, tam olarak ağırlıkça %44 ve %54.1 B_2O_3 içeren karışımlarda, Al_2O_3 tamamen tüketildiğinde elde edilmiştir. Ancak, sahip olduğu iğnesel partikül şekli sinterleme esnasında yoğunlaşmayı zorlaştırmaktadır. Bu nedenle, yoğunlaşma kristal yapılarının benzerliğinden dolayı mullit ile kompozit yapı oluşturma yöntemi ile kontrol edilmiştir. $Al_{18}B_4O_{33}$+%2 CaO (numune ismi AB), %100 $Al_{18}B_4O_{33}$ (numune ismi PAB), %35 $Al_{18}B_4O_{33}$+%35 müllit+%30 cam kompozit (numune ismi AMG) ve %70 $Al_{18}B_4O_{33}$+%30 cam kompozit (numune ismi ABG) jel döküm ile hazırlanmıştır. Sıvı faz sinterleme mekanizması ile yoğunlaşmayı arttırmak için cam faz ve CaO eklenmiştir. 1350°C'de 1 saat sinterlenen PAB numunesinin göreceli yoğunluğu %59.7 olarak ölçülmüştür, fakat %2 CaO ilavesi ile yoğunluk %95.4'e yükselmiştir (AB numunesi). AMG seramikleri %94.8 göreceli yoğunluğa ve sıfıra yakın açık gözenek ve su emme değerlerine ulaşmıştır. ABG seramikleri %89.4 gibi sınırlı bir

yoğunluğa ulaşmıştır. Numunelerin dielektrik sabitleri 5 MHz'de 4 ile 6.6 arasında ölçülmüştür. PAB numunesi en düşük (4.05), ABG numunesi ise en yüksek dielektrik sabiti değerine (6.58) sahip olmuştur. Vickers sertlik değerleri, AMG kompozit numunesi için 924±118, AB için 998±52, ABG kompozit numunesi için 825 ± 120 ve PAB numunesi için 98 ± 10 olarak ölçülmüştür. AB numunesinin termal iletkenliği 7.26 W/m.K iken, PAB numunesi düşük yoğunluğundan dolayı termal iletkenliği 2.7 W/m.K olarak ölçülmüştür. Kristal fazların (örneğin, $Al_{18}B_4O_{33}$ ve/veya mullit) amorf cam faz tarafından çevrelenmiş olmasında dolayı AMG ve ABG numunelerinin termal iletkenlik değerlerinde (1.73 W/m.K) sert bir düşüş meydana gelmiştir. Bu çalışmada, Al borat-cam (ABG) ve Al borat- müllit-cam (AMG) kompozitleri literatürde ilk kez araştırılmıştır. ABG seramiklerinde cam fazın gözenekli yapıyı yeteri kadar dolduramamasından dolayı yoğunluk %89.4 gibi sınırlı bir göreceli yoğunluğa ulaşmıştır, fakat AMG seramiklerinde müllit eklenmesinden dolayı %94.8 oranında göreceli yoğunluğa ve sıfıra yakın açık gözenek ve su emme değerlerine ulaşmıştır. Bu sonuçlar, alüminyum borat esaslı seramiklerin, metal matrisli kompozit uygulamalarda takviye faz olarak, termal yalıtkan, filtre, altlık ve radom uygulamalarında kullanılabileceğini göstermektedir.

Anahtar kelimeler: Al borat toz sentezi, yoğunlaşma, dielektrik özellikler, mekanik özellikler, ısısal özellikler.

CONTENTS

M. Sc. THESIS EXAMINATION RESULT FORM ii
ETHICAL DECLARATION iii
ACKNOWLEDGMENTS iv
ABSTRACT v
ÖZ vii
CONTENTS ix
NOMENCLATURE x
LIST OF TABLES xii
LIST OF FIGURES xiii

CHAPTER 1-INTRODUCTION **1**
1.1 Aluminum Borate 1
1.2 Mullite 6
1.3 Gel Casting 8
1.4 Literature Review on Aluminum Borate Ceramics 16
1.5 Objective 18

CHAPTER 2-EXPERIMENTAL METHODS 19

CHAPTER 3-RESULTS AND DISCUSSION 25
3.1 Powder Synthesis and Phase Formation 25
3.2 Sintering and Densification 49
3.3 Dielectric, Mechanical and Thermal Properties 64
3.4 Possible Applications 67

CHAPTER 4-CONCLUSION **70**

REFERENCES 74

CURRICULUM VITAE 81

NOMENCLATURE

Abbreviations

°	Degree
μm	Micrometer
2θ	Diffraction angle
$3Al_2O_3.2SiO_2$	Mullite
3D	3-Dimension
$Al_{18}B_4O_{33}$	Aluminum borate
Al_2O_3	Alumina
Al_5BO_9	Aluminum borate
AM	Acrylamide
APS	Ammoniumpersulfate
B_2O_3	Boron trioxide
C	Capacitance
CaO	Calcium Oxide
C_p	Specific heat
d_{50}	Median particle size
E	Young's modulus
E	Electric field
EDS	Energy Dispersive Spectrometry
GHz	Gigahertz
GPa	Giga Pascal
h	hour
HMAM	Hydroxymethylacrylamide
HV	Vickers Hardness
Hz	Hertz
K	Dielectric constant
K_c	Fracture toughness
KHz	Kilohertz
LPS	Liquid Phase Sintering
m	Meter
m	Mass
MBAM	Methylenebisacrylamide
MgO	Magnesium oxide
MHz	Megahertz
MPa	Mega Pascal
MPEGMA	Methoxypoly (ethyleneglycol) monomethacrylate

N	Newton
NVP	N-vinylpyrrolidone
Pa	Pascal
P_e	Volume friction of porosity
PEG600	Polyethylene glycol 600
ppm	Part per million
R	Thermal shock resistance
rpm	Round per minute
s	second
SEM	Scanning Electron Microscopy
SiO_2	Silica
TBA	Tert-butyl alcohol
TEMED	Tetramethylenediamine
TG-DTA	Thermogravimetric-Differential Thermal Analysis
TiO_2	Titanium oxide
V	Volume
vol%	Volume percent
W	Watt
wt%	Weight percent
XRD	X-ray Diffraction
ZrO_2	Zirconium dioxide
α	Thermal expansion coefficient
Δ	Difference
ε_0	Permittivity of space (8.8542x 10^{-12} $F.m^{-1}$)
ρ	Density
σ_f	Flexural strength
Δ	Difference
ε_0	Permittivity of space (8.8542x 10^{-12} $F.m^{-1}$)
ρ	Density
σ_f	Flexural strength

LIST OF TABLES

Table 1.1 Properties of aluminum borate ($Al_{18}B_4O_{33}$) 5
Table 1.2 Properties of mullite 8
Table 2.1 Properties of Al_2O_3 powder 19
Table 2.2 Mole ratios of Al_2O_3/B_2O_3 and amounts of B_2O_3 used in the powder mixtures 20
Table 2.3 Properties of the mullite powder 21
Table 2.4 Composition of the glass phase 21
Table 2.5 Amount of chemical constituents used in gel casting 22
Table 3.1 Stoichiometric elemental ratios (wt%) in the aluminum borate compounds 40
Table 3.2 Sintering and densification parameters for the sintered samples 58
Table 3.3 Calculated elemental ratios in the AMG composition 60
Table 3.4 Dielectric properties of the ceramics measured at 5 MHz 65
Table 3.5 The Vickers hardness values (HV) of the ceramic samples 66
Table 3.6 Thermal conductivity values of the samples measured at room temperature 67
Table 3.7 Properties of all ceramics sintered at 1350°C for 1h 69

LIST OF FIGURES

Figure 1.1 The binary phase diagram of the Al_2O_3-B_2O_3 2

Figure 1.2 The crystal structure of $Al_{18}B_4O_{33}$ and $Al_4B_2O_9$. Blue polyhedra: AlO_6 octahedra, yellow spheres: Al (in AlO_4 or AlO_5 polyhedra), green spheres: B (in BO_3 or BO_4 polyhedra), red spheres: O..... 5

Figure 1.3 The Al_2O_3-SiO_2 system as described by Aksay and Pask 7

Figure 1.4 Crystal structure of mullite in a projection of c-axis 7

Figure 1.5 General concept of gel casting process..... 10

Figure 1.6 Polymerization mechanism of acrylamide by the aid of TEMED and APS 10

Figure 1.7 The effect of TEMED/APS concentration on the curing time 12

Figure 1.8 The effect of APS and temperature on gelation time 12

Figure 1.9 Ceramic forming methods 15

Figure 1.10 Ceramic products formed by gel casting..... 15

Figure 2.1 Burnout schedule of the green samples 23

Figure 3.1 Particle size distribution of Al_2O_3 powder after ball milling for 24 hours 25

Figure 3.2 XRD pattern of initial B_2O_3 powder 26

Figure 3.3 The TG-DTA analysis of the initial B_2O_3 powder..... 27

Figure 3.4 The prepared powder mixtures marked on the phase diagram..... 28

Figure 3.5 XRD pattern of the mixture at a mole ratio of 5.73 (10.7 wt% B_2O_3) prepared by ZrO_2 balls..... 29

Figure 3.6 XRD pattern of the mixture at a mole ratio of 5.73 (10.7 wt% B_2O_3) prepared by Al_2O_3 balls 29

Figure 3.7 XRD pattern of the mixture at a mole ratio of 4.41 (13.4 wt% B_2O_3)..... 30

Figure 3.8 XRD pattern of the mixture at a mole ratio of 3.09 (18.1 wt% B_2O_3)..... 31

Figure 3.9 XRD pattern of the mixture at a mole ratio of 1.77 (27.9 wt% B_2O_3)..... 31

Figure 3.10 XRD pattern of the mixture at a mole ratio of 1.3 (34.4 wt% B_2O_3)..... 32

Figure 3.11 XRD pattern of the mixture at a mole ratio of 0.87 (44 wt% B_2O_3)..... 33

Figure 3.12 XRD pattern of the mixture at a mole ratio of 0.58 (54.1 wt% B_2O_3)..... 33

Figure 3.13 XRD patterns of all prepared compositions calcined at 1300°C for 1h. 34

Figure 3.14 TG-DTA analysis of the powder mixture at a mole ratio of 0.87 (44 wt% B_2O_3)..... 35

Figure 3.15 XRD patterns of the powders prepared at a mole ratio of 0.87 (44 wt% B_2O_3) and calcined at various temperatures 38

Figure 3.16 SEM pictures of the powder mixture prepared at a mole ratio of 5.73 (10.7 wt% B2O3) and calcined at 1300°C for 1h 40

Figure 3.17 SEM pictures of the mixture prepared at a mole ratio of 4.41 (13.4 wt% B_2O_3) and calcined at 1300°C for 1h..... 41

Figure 3.18 SEM pictures of the mixture prepared at a mole ratio of 3.09 (18.1 wt% B_2O_3) and calcined at 1300°C for 1h..... 41

Figure 3.19 SEM pictures of the mixture prepared at a mole ratio of 1.77 (27.9 wt% B_2O_3) and calcined at 1300°C for 1h..... 42

Figure 3.20 SEM pictures of the mixture prepared at a mole ratio of 1.3 (34.4 wt% B_2O_3) and calcined at 1300C for 1h 42

Figure 3.21 SEM pictures of the mixture prepared at a mole ratio of 0.87 (44 wt% B_2O_3) and calcined at 1300°C for 1h..... 43

Figure 3.22 SEM pictures of the mixture prepared at a mole ratio of 0.58 (54.1 wt% B_2O_3) and calcined at 1300°C for 1h..... 44

Figure 3.23 SEM-EDS analysis of the mixture prepared at a mole ratio of 0.87 (44 wt% B_2O_3) and calcined at 1300°C for 1h..... 45

Figure 3.24 SEM-EDS pictures of the mixture prepared at a mole ratio of 0.58 (54.1 wt% B_2O_3) and calcined at 1300°C for 1h..... 45

Figure 3.25 SEM pictures of the powders synthetized from the mixture prepared at a mole ratio of 0.87 (44 wt% B_2O_3) at various calcination temperatures; (a) 1100°C, (b) 1200°C, (c) 1300°C and (d) 1400°C for 1 h..... 47

Figure 3.26 Particle size distribution of mullite [66]..... 50

Figure 3.27 Particle size distribution of glass [59]..... 50

Figure 3.28 Samples after burn out process 51

Figure 3.29 XRD patterns of the AB samples; (top) XRD patterns taken from the as-sintered ceramic surfaces as a function of sintering temperature, (bottom) comparison of the XRD patterns taken from the as-sintered and polished surfaces of the ceramic sintered at 1350°C. 53

Figure 3.30 XRD patterns of the AMG samples; (top) XRD patterns taken from the as-sintered ceramic surfaces as a function of sintering temperature, (bottom) comparison of the XRD patterns taken from the as-sintered and polished surfaces of the ceramic sintered at 1350°C. 54

Figure 3.31 XRD patterns of the ABG sample sintered at 1350°C for 1h 55

Figure 3.32 XRD patterns of the PAB sample sintered at 1350°C for 1h 56

Figure 3.33 Comparison of the XRD patterns of the ceramics sintered at 1350°C for 1 h; (left) XRD patterns taken from the as-sintered ceramic surfaces, (right) XRD patterns taken from the polished ceramic surfaces 57

Figure 3.34 SEM pictures of the (a) PAB, (b) AB, (c) ABG and (d) AMG ceramics sintered at 1350°C for 1h. 61

Figure 3.35 SEM-EDS elemental mapping of the AMG ceramic sintered at 1350C for 1h. 61

CHAPTER 1

INTRODUCTION

1.1 Aluminum Borate

Aluminum borate has thermodynamically stable two crystalline phases with mullite-type structures which are $Al_{18}B_4O_{33}$ ($9Al_2O_3.2B_2O_3$ or A_9B_2) and $Al_4B_2O_9$ ($2Al_2O_3.B_2O_3$ or A_2B) in the binary system Al_20_3-B_2O_3 phase diagram as given in Figure 1.1. Samples were sealed in platinum tubes to eliminate volatilization losses and to ensure a water-free environment. The samples were held for 16-24 h at specified temperatures, and occasionally up to 120 h, and then they were quenched in air or mercury. Finally, the phases formed were identified with the polarizing microscope and the X-ray diffractometer. Phase diagram indicates that $Al_4B_2O_9$ melts incongruently to yield $Al_{18}B_4O_{33}$ and liquid at 1035°C. $Al_{18}B_4O_{33}$ melts incongruently at 1950°C and B_2O_3 melts at 470°C [1]. Although this was the binary phase diagram constructed in 1962, almost all researchers have referenced this diagram in their studies. Stoichiometric composition of $Al_{18}B_4O_{33}$ was discussed in detail by Fisch et al. [2]. They explained that orthorhombic Al_2O_3-rich aluminum borate has two slightly different phases of Al_5BO_9 ($5Al_2O_3.B_2O_3$) and $Al_{18}B_4O_{33}$ ($\approx Al_{4.91}B_{1.09}O_9$). The formula of $Al_{18}B_4O_{33}$ was first determined from chemical analysis results in the absence of crystal structure data, but structural studies indicated that Al_5BO_9 was the idealized composition. However, $Al_{18}B_4O_{33}$ is still accepted as an idealized stoichiometric composition considering that tetrahedrally coordinated B replaces 9% Al vacancies in the crystal structure. They prepared both compositions and one with excess B by solid state reactions at temperatures above 1100ºC in a lid-covered platinum crucible in air, using $Al(NO_3)_3.9H_2O$ or α-Al_2O_3 and B_2O_3 or H_3BO_3. All structural analyses indicated that the idealized compound should be reported as $Al_{5-x}B_{1+x}O_9$ with $x<0.038$ which was close to Al_5BO_9 (Note that although they are compositionally very close to each other, Al_5BO_9 has 12.01 wt% B_2O_3 and $Al_{18}B_4O_{33}$ has 13.17 wt% B_2O_3). It was concluded that Al_2O_3-rich mullite-type aluminoborates

synthesized above 1100°C did not have $Al_{18}B_4O_{33}$ composition and the exact stoichiometry was close to Al_5BO_9.

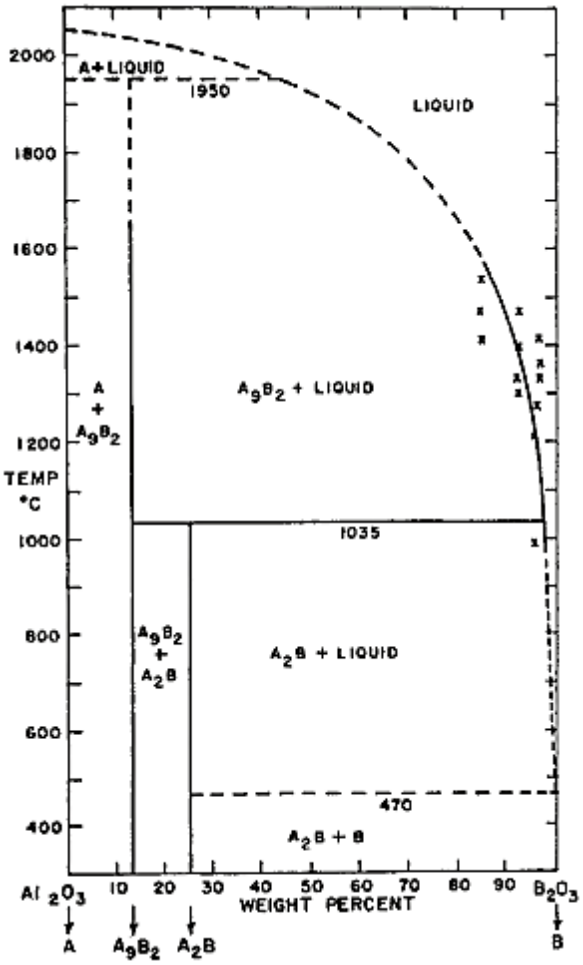

Figure 1.1 The binary phase diagram of the Al_2O_3-B_2O_3 [1]

Hoffman et al. [3] characterized mullite-type $Al_{6-x}B_xO_9$ compounds in terms of powder diffraction and spectroscopic methods. They also mentioned about the ambiguity of the chemical composition of Al borate phase, but they preferred $Al_{18}B_4O_{33}$ as the exact stoichiometric composition. Series of powder samples were prepared using nitrate decomposition method as a function of boron oxide content (i.e., 5 to 90 wt% B_2O_3) in the precursor, using $Al(NO_3)_3.9H_2O$ and $B(OH)_3$. The samples were calcined at 1000°C for 72 h or 900°C for 6 h, using covered platinum crucibles and then quenched to room temperature. $Al_{6-x}B_xO_9$ phases were found to crystallize between 13.17 and 25.45 wt% B_2O_3 in the precursor phase (corresponding to (A_9B_2) $1.09 \leq x \leq 2$ (A_2B)). Furthermore, lattice parameters successively decreased with increasing B_2O_3 content

and NMR spectroscopy indicated a complete solid solution series for the $Al_{6-x}B_xO_9$ phases. XRD results indicated that at least three different alumina diffraction peaks (α,γ,θ) were observed in the low B_2O_3 region (e.g., <13.17 wt% B_2O_3). Furthermore, aluminum-rich phases were obtained due to highly volatile B_2O_3 upon extended heating period during powder synthesis. Phase formation studies by XRD and DSC indicated that first exothermic signal was observed at 890°C for 13.17 wt% B_2O_3 and 830°C for 30 wt% B_2O_3, resulting in the crystallization process in the phase field A_2B–A_9B_2, whereas another DTA signal was observed above about 1000°C, belonging to a probable phase transformation of $Al_{6-x}B_xO_9$ into A_9B_2. Higher B_2O_3 content reduced glass phase viscosity, resulting in enhanced atomic diffusion as well as lower crystallization temperature. A signal above 1000°C was not observed for the exact initial composition of A_9B_2 (13.17 wt% B_2O_3).

Ray [4] synthesized Al borate powders using stoichiometric mixture of Al_2O_3 and B_2O_3 (13.17 wt% B_2O_3). A_2B started to form at 800°C (about 10%) and then A_9B_2 phase formation was completed at 1100°C with a trace amount of α-Al_2O_3 left. The following phase formation reaction was reported to take place with increasing calcination temperature;

$$2(2Al_2O_3.B_2O_3) + 5Al_2O_3 \rightarrow Al_{18}B_4O_{33} \quad \textbf{(1.1)}$$

Even though the powder mixture was prepared at the stoichiometric ratio of A_9B_2, other stoichiometric phase A_2B formed as the intermediate step during phase formation in addition to the trace amount of Al_2O_3.

Many researchers studied $Al_{18}B_4O_{33}$ composition but chemical and crystallographic analysis of the same composition yielded close-but-different mole ratios. Mazza et al. [5] used H_3BO_3 and $Al(NO_3)_3.9H_2O$ precursors and proposed a solid solution $Al_{6-x}B_xO_9$ with $1 \leq x \leq 3$. They consider Al_5BO_9 as being stable in the temperature regime between 900 and 1000°C. Garsche et al. [6] grew single-crystals by fusion of Al_2O_3 and B_2O_3 in a sealed platinum capsule at 1500C, and reported the phase as $Al_{18}B_4O_{33}$. Sokolova et al. [7] grew single crystals by cooling an $Al_2O_3 – B_2O_3 – Y_2O_3 – K_2O – MoO_3$ melt from 1150 to 950°C. Although cell dimensions and orthorhombic symmetry were in accordance with the $Al_{18}B_4O_{33}$, single crystal X-ray structure refinement yielded

Al_5BO_9 composition instead of $Al_{18}B_4O_{33}$. In brief, afore-mentioned results indicate that crystal-chemical studies varied as for the exact Al_2O_3:B_2O_3 ratios probably because Al borate applications were thought to be more important than its exact chemical characterization.

$Al_{18}B_4O_{33}$ has an orthorhombic crystal structure and is given in Figure 1.2. Mullite-type Al borates are determined by chains of edge-sharing AlO_6 octahedra aligned in the *c* direction and is cross-linked by corner-shared AlO_4 tetrahedra. Its lattice parameters are *a*=7.6874 A˚, *b*=15.0127 A˚, *c*=5.6643 A˚ [8] closely match the *a* parameter and are twice the *b* and *c* parameters of mullite (i.e., *a*=7.5456 A˚, *b*=7.6898 A˚, *c*=2.8842 A˚) [9]. $Al_{18}B_4O_{33}$ and Al_5BO_9 consists of only trivalent cations Al^{3+} and B^{3+} in four-fold coordination. Therefore, both Al and B may form a solid solution at a tetrahedrally coordinated site of the mullite-type structure [2, 3].

Al borate has unique properties as summarized in Table 1.1. In particular, it has a low density of 2.93 gr/cm^3, good stability up to 1300°C and thermal expansion coefficients of ≈4.4 and ≈1.9 ($\times10^{-6}$/°C) in the axial and radial directions, respectively. $Al_{18}B_4O_{33}$ has been used in several applications such as optical electronics, structural applications and tribology due to its outstanding properties. Therefore, Al borate ceramics are strong alternative materials for oxidation-resistant reinforced composites, chemical and heat-insulating materials, and filters [10, 11]. Lithium-doped Al borate with low permittivity (3.9), near-zero shrinkage at low sintering temperatures (e.g., 0.4% at 700°C and 2.4% at 750°C) was proposed as low temperature cofired ceramics [12]. Al borate whiskers have also used as an effective reinforcement in aluminum matrix composites in order to enhance mechanical properties. The flexural strength of 172 MPa and compression strength of 324 MPa were obtained at 10 wt% Al borate whisker reinforcement due to lower porosity and better reinforcement dispersion, which was attributed to good interfacial bonds, less porosity and uniform distribution in the composite microstructure [13]. Lin et al. [14] also prepared $Al_{18}B_4O_{33}$ whiskers reinforced Al matrix composites. The composites with homogeneously distributed whiskers were produced by semi-solid stirring at 610°C for 30 min. They reported enhanced mechanical properties such as ultimate tensile strength of 264 MPa and elastic modulus of 86 GPa for the ZnO-coated $Al_{18}B_4O_{33}$/6061Al composites as

compared to ultimate tensile strength of 124 MPa and elastic modulus of 70 GPa for the 6061Al. ZnO coating improved the wettability between whiskers and matrix, and hence enhanced the tensile properties of the composites. Other applications include construction components in the nuclear reactors due to neutron absorbing capabilities, and in refractory linings due to high resistance against boron-rich glass melts [15], low thermal expansion and low dielectric constant electronic ceramic packages [4].

Table 1.1 Properties of aluminum borate ($Al_{18}B_4O_{33}$) [4, 16]

Properties	**Values**
Density (gr/cm^3)	2.93
Tensile Strength (GPa) at 25°C	~8
Young's modulus (GPa)	400
Hardness (Mohs)	7
Thermal conductivity (W/m.K) at 25°C	≈ 6.5 (hot pressed) – 8 (cold-pressed and sintered)
Thermal expansion coefficient (10^{-6}/K)	≈ 4.4 axial and ≈ 1.9 radial directions
Dielectric Constant up to 14 GHz	5.6

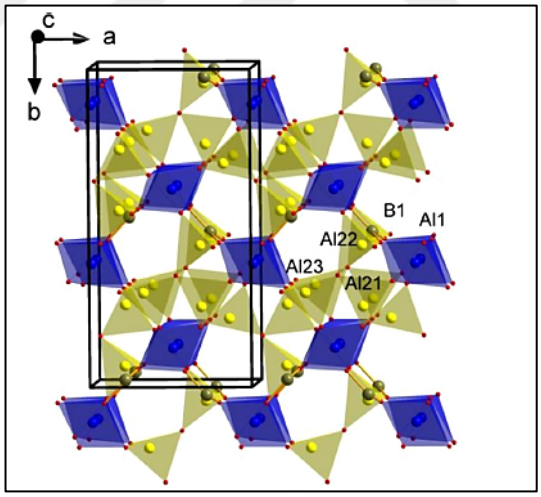

Figure 1.2 The crystal structure of $Al_{18}B_4O_{33}$ and $Al_4B_2O_9$. Blue polyhedra: AlO_6 octahedra, yellow spheres: Al (in AlO_4 or AlO_5 polyhedra), green spheres: B (in BO_3 or BO_4 polyhedra), red spheres: O [3]

Aluminum borate has been prepared via various methods including thermal evaporation, flux-combustion [17] and catalyst synthesis, solid-state reaction, chemical vapor deposition and sol-gel preparation [18-20]. Molten salt synthesis method was used to synthesize single-phase $Al_{18}B_4O_{33}$ whiskers with an orthorhombic structure [21]. Traditional chemical flux method was used to synthesize nanowires

made of $Al_{18}B_4O_{33}$ with fibrous structure. Flux method was one of the simple methods for preparing ceramics with preferential orientation [17]. Zhou et al. [22] obtained orthorhombic $Al_4B_2O_9$ nanorods with uniform diameters of 20-30 nm by low-heating-temperature solid state precursor method. Wang et al. [23] prepared $Al_{18}B_4O_{33}$ whiskers with an average diameter distribution of 400 nm by a high-temperature solid-state reaction. Solid state sintering is mostly preferential route among these synthesis methods due to its ease of applicability and low-cost [4,24].

1.2 Mullite

Mullite is favorable ceramic materials because of its excellent features in terms of mechanical and thermal properties [25,26]. Mullite is in the family of orthorhombic aluminasilicates with a general composition of $Al_2(Al_{2+2x}Si_{2-2x})O_{10-x}$. The stoichiometric composition of mullite is $3Al_2O_3.2SiO_2$ which is only stable compound under atmospheric conditions [27].

There was a controversial case about the melting behavior of the mullite whether congruently or incongruently in the past years. The first binary phase diagram of the Al_2O_3-SiO2 system described by Bowen and Grieg [28] indicates that mullite melts incongruently at 1810ºC. The other Al_2O_3-SiO_2 phase diagram described by. The recently modified compositional range of mullite explained by Aksay and Pask [29] is shown in Figure 1.3. It indicates that the phase diagram involves stable phases and two meta-stable phases and mullite incongruently melting to a liquid at 53 wt% Al_2O_3 at 1828ºC and products are Al_2O_3 and liquid [29]. Presence of corundum dominates the melting behavior of the mullite in the phase diagram because precipitation of α-Al_2O_3 is assisted by α-Al_2O_3 nuclei [29].

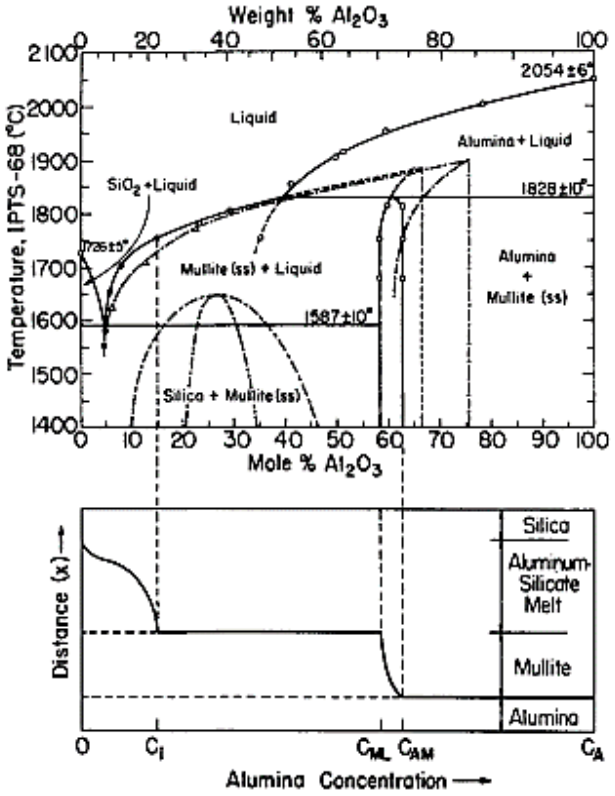

Figure 1.3 The Al_2O_3-SiO_2 system as described by Aksay and Pask [29]

The characteristics of mullite-type structure is orthorhombic containing single parallel chains of edge sharing AlO_6 octahedra in a tetragonal arrangement. The crystal structure is given in Figure 1.4 [30].

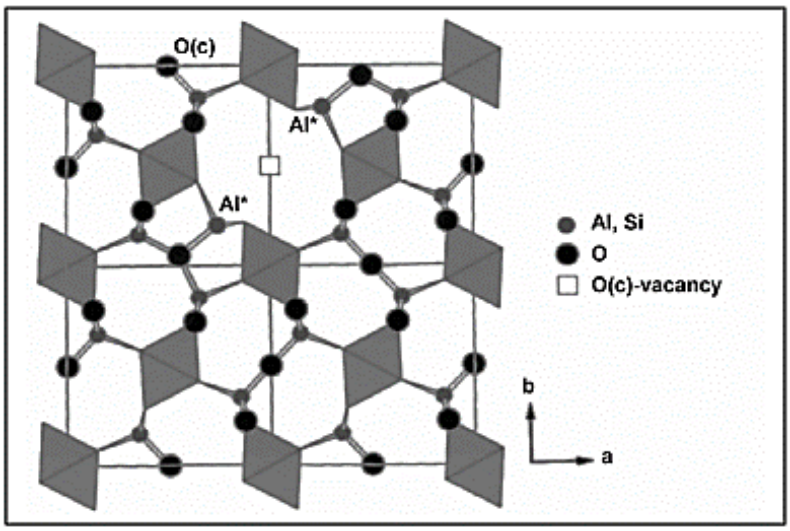

Figure 1.4 Crystal structure of mullite in a projection of c-axis [30]

Mullite ceramics are notable for advanced structural and electronic applications owing to their suitable properties as summarized in Table 1.2. Limiting factor for usage of

the mullite ceramics is its low fracture toughness but its excellent creep resistance and thermal shock resistance at high temperatures as compared to other ceramic materials (e.g., Al_2O_3) dominates this restrictive features of mullite [31]. Hence, it's commonly used for high temperature applications. Mullite material also has excellent creep resistance at above 1500°C with limited plastic deformation [31, 32].

Table 1.2 Properties of mullite [33, 34, 35, 36, 37]

Properties	Values
Hardness (HV)	1070-1120
Strength (MPa) 25°C	~200
Young's modulus (GPa)	143-230
Thermal conductivity (W/m.K) (full crystalline ceramic)	6 at 20°C 3 at 1400°C
Thermal expansion coefficient (10^{-6}/K) (20-1400°C)	4.5
Dielectric constant up to 14 GHz	6.5-8.1
Dielectric loss (25°C,10-40 GHz)	<0.001
Poisson's ratio	0.23-0.26
Fracture toughness, MPa.√ m	2.25-2.55

1.3 Gel Casting

Ceramics that have a wide range of properties such as brittle, wear-resistant, stability at higher temperatures, thermal insulation etc. are classified as an inorganic and non-metallic materials. Traditional ceramic forming routes of dry pressing, slip casting, tape casting are commonly used in variety of industrial applications. Recently, gel casting is favorable advanced method which offers the production of high performance ceramic materials with a complex and near-net shape. Produced ceramic materials via gel casting method have improved microstructure in terms of less agglomerates and higher homogeneity [38].

The main concept of the gel casting process is presented in Figure 1.5 [39]. A slurry consisting of ceramic powder and a solvent/monomer solution is prepared by using appropriate mechanisms (e.g., speed mixer, stirring, ball milling or similar ones). The

gel system composed of acrylamide (AM, -C_3H_5NO-) as a monomer, methylene bisacrylamide (MBAM, $C_7H_{10}N_2O_2$) as a difunctional monomer cross-linker, and ammonium persulfate (APS, $(NH_4)_2S_2O_8$) as a free radical initiator [38, 40, 41]. Tetramethylethylenediamine (TEMED, $C_6H_{16}N_2$) was added as a catalyst to increase the rate of cross-linking reaction [40, 41]. Other common monomers are hydroxymethylacrylamide (HMAM), N-vinylpyrrolidone (NVP), methoxypoly (ethyleneglycol) monomethacrylate (MPEGMA) [40, 41]. Gel casting technique strongly related with the formation of a cross-linked polymer-solvent gel system. The polymerization of solution produces a rigid gel, which deactivates the motion of ceramic particles and solidifies in the mold [40, 41]. Ball milling process generally is preferred for preparation of gel casting slurries because ball milling offers effective mixing of powders and allows required aging time for hydroxylation of particle surfaces to obtain stable slurry dispersions. Ball milling also allows for controlled particle size reduction, if required [39, 40, 41]. First, monomer solution, solvent, dispersant and powder mixture are mixed to form a stable slurry. Water is generally preferred as a solvent for most gel casting applications to improve dispersion of ceramic powders in the presence of a dispersant. Then, APS and TEMED are added and mixed for several minutes. During mixing of the ceramic slurry by ball milling, the slurry is de-aired under vacuum using a mechanical pump. Also, a defoamer is used to facilitate deairing. De-airing is necessary during gel casting process in order to obtain pore-free ceramics [40]. The prepared ceramic slurries are then cast into appropriate molds to obtain desired shaped parts. Poured ceramics are aged at 50^oC for 30-60 minutes. Gelation is accelerated at room temperature by adding TEMED [42,44]. The cross-linking process of acrylamide monomers occurs by TEMED and APS. Figure 1.6 represents the polymerization of a polyacrylamide matrix [43]. APS generates oxygen free radicals due to reduction of APS by TEMED. Then, the process is triggered by generated oxygen free radicals. After that, the double bonds between CH_2 and CH in the AM and MBAM are broken and turn into single bonds**.** At the same time, crosslinking of the bisacrylamide monomers occur after curing of slurry is completed within the mold, then, sample is quickly removed from the mold [40-45]. The green body is dried in a drying oven. Humidity should be controlled during drying of the green body to avoid cracking [41].

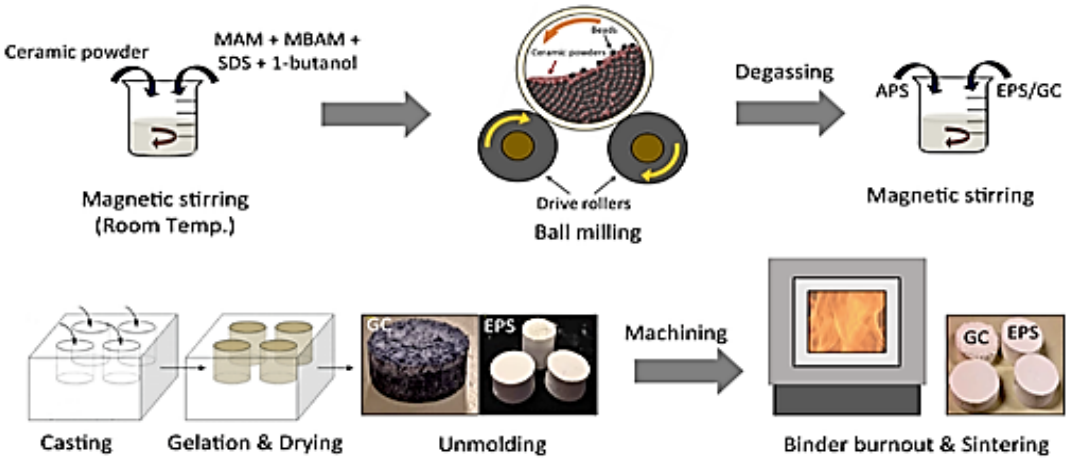

Figure 1.5 General concept of gel casting process [39]

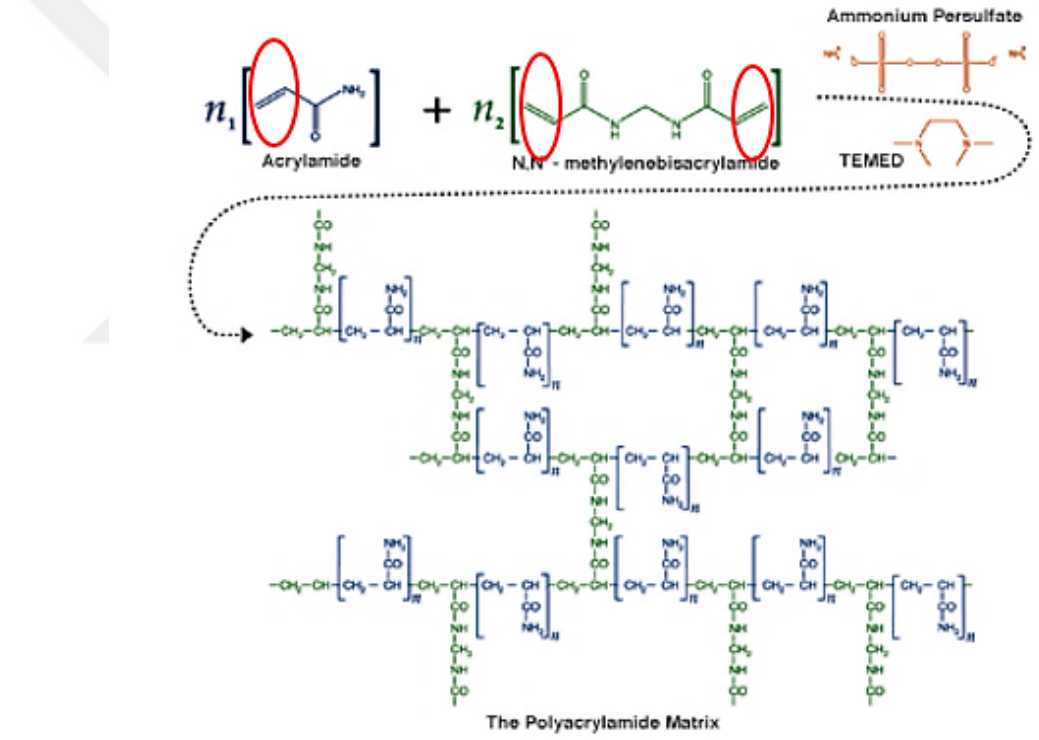

Figure 1.6 Polymerization mechanism of acrylamide by the aid of TEMED and APS [43]

One of the critical parameters during gel casting is the solid content loading. In ceramic slurries involving higher solid content can result in final ceramic products having higher density [38]. Besides, the solid loading parameter can be controlled at a certain level because final properties of ceramic products depend on a ceramic slurry with a low viscosity such that slurry has ability to flow easily with as high solid loading as possible. Therefore, optimization of the solid content and viscosity of the ceramic

slurry is very important parameter [42]. Higher solid content in ceramic slurry decreases the risk of excessive shrinkage in the ceramic green body which causes problems such as cracking and warping. But, ceramic slurry involving too much high solid content generally causes higher viscosity which makes the slurry difficult to cast into the mold [41, 42]. Ceramic suspension consist of 50 vol% solid content as a minimum results in good fluidity. Also, convenient dispersant mechanisms have important effect to obtain ceramic slurry which has good fluidity with high solid loading [38].

Amounts of TEMED and APS used in ceramic slurries influence process parameters during gel casting. For instance, when concentration of initiator APS is raised, shorter average polymer chain length of AM and MBAM forms, producing higher gel turbidity and lower gel elasticity, and vice versa [38-41]. The gel elasticity directly has a strong effect on demolding of the samples; for example, tearing in the gel cast green sample or cracking during burnout and sintering processes due to the formation of stress gradients on sample's surface [41, 42]. The effect of TEMED and APS concentration on curing time is shown in Figure 1.7 [46]. A higher amount of APS and TEMED results in higher amount of free radicals. To summarize, shorter gelation time occurs when cross-linking of the monomers is accelerated [42]. Also, the gelation time decreases with increasing temperature due to accelerated generation of the free radicals, which then accelerates cross-linking polymerization process [47]. The mixed effect of APS and temperature on gelation time is represented in Figure 1.8 [41].

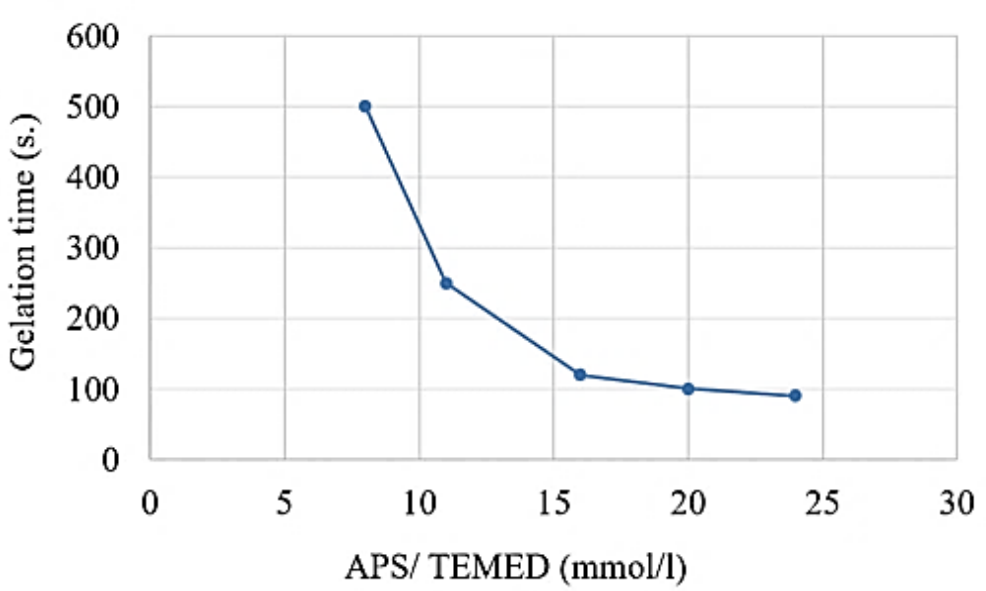

Figure 1.7 The effect of TEMED/APS concentration on the curing time [46]

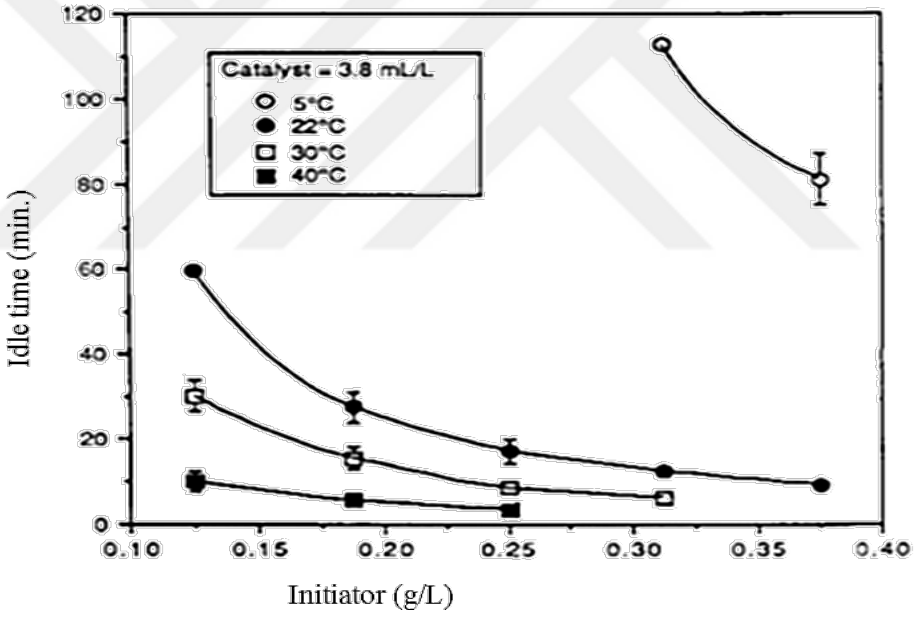

Figure 1.8 The effect of APS and temperature on gelation time [41]

Mold selection is another critical parameter to attain effective gel casting process. Mostly used mold materials are aluminum, PVC, glass, polystyrene (PS), and polyethylene (PE) [47, 48]. Aluminum has an advantage in terms of ease of machining capability and its low-cost as compared with other mold materials. In details, anodized aluminum offers good surface properties. Glass molds are generally appropriate for casting of thin films and tubes [49, 50]. Gel casts have ability to be removed from glass surfaces readily owing to the existence of smooth glass surfaces. In addition to these

advantages, machining of glass material is a hard process which makes the usage of glass molds difficult for large scale productions [47-50]. PVC or polymer molds are generally convenient for forming of bars, tubes and rings because a thin ungelled layer as a lubricant agent forms on the surface of gel cast product, which assists the gel cast part to be removed from the mold easily acting. This formed ungelled layer does not grow on the surface of the gel cast part if neoprene is selected as a mold material. PE and PS molds are generally used to produce test samples [49, 50]. Also, PE and PS may lead to the growth of an ungelled layer on the surface of the gel cast piece. In addition to the mold materials explained above, there are some special mold materials such as graphite, meltable core materials, plaster and other polymeric materials [47-50]. To summarize, selection of the mold directly related with desired shape of the gel cast parts.

As a summary, there are several critical parameters to perform effective gel casting. One of them is the preparation of a gel casting slurry with high solid loading. Green body should have a high packing density with well-dispersed and highly-packed powders in the prepared ceramic slurry [38]. So, selected method for dispersing and choice of the dispersing agent used in slip preparation are critical. Another one is the selection of a convenient combination of monomer and cross linker. Chemical features of monomer and cross-linker and their relative amounts have strong effect on mechanical characteristics of the green body [38, 40]. Third parameter is choice of appropriate initiator type and its concentration which affects the casting time [38, 40]. Another important factor is the drying stage of the green bodies without causing stress gradient and cracking. If rate of liquid evaporation is rapid, stresses are induced in the ceramic structure, which easily causes to the formation of cracks [40, 41, 47]. Optimum rate of liquid evaporation must be experimentally determined to avoid the formation of cracks and warpage caused by rapid drying. Therefore, drying should be carried out to cause a minimum level of stress formation. Another factor is the choice of an appropriate mold material used for casting of ceramic slurries [40, 41, 47]. This provides us to remove green body from the mold easily.

Several ceramic forming methods are present which are pressing, colloidal and plastic methods as shown in Figure 1.9 [51]. The limiting factor of forming of ceramic parts

is the limited part geometries particularly for mostly used die pressing method. Gel casting is considered as a colloidal process to produce 3-D complex parts with near-net shaping [47]. The products having complex shapes which are produced by gel-casting is given in Figure 1.10 [52]. Table 1.3 compares the gel casting process with the other traditional ceramic forming methods [47]. Gel casting is a rapid process and allows the formation of ceramic products which have higher strength as compared to other ceramic forming methods [41, 47]. The distinctive feature of gel casting is to allow the formation of high quality final ceramics with minimum molding defects by attaining high degree of homogeneity in the ceramic slurry owing to cross-linking of the monomers [41, 47]. Less molding defects offer high-quality final ceramic products [41, 47]. The amount of binder used in gel casting process is less as compared to other forming processes (other than pressing) so removal of the binder occurs in a shorter time [41, 47]. Ceramic products in a wide range of dimensions can be produced by gel casting. When other traditional processes are considered, injection molding can provide formation of complex shaped ceramic products. However, binder removal process consuming a lot of time, size limitation and defects are disadvantages of the injection molding process [41, 47]. Slip casting has some limitations related to maximum achievable thickness and long forming times. Pressure casting provides a rapid rate of casting and less molding time [41, 47].

Additive Manufacturing (AM) or 3D Printing processes are used to create parts by adding materials layer-by-layer. Novel additive manufacturing processes have been developed for complex ceramic parts which have no cracks or large pores. The disadvantage of this method is that equipment cost is expensive and it requires long printing periods [53]. There are generally two different methods of AM which are direct process and indirect processes. For direct process, parts are produced in a single-step in which the geometrical shape and material characteristics of part are obtained simultaneously. For indirect process, parts are produced in two or more steps in which first step is related with geometrical shape of parts and the following step provides material characteristics of the part. Mostly used AM method is indirect process that uses a sacrificial binder material to form ceramics. Indirect process is more available method to fabricate different type of ceramics while direct AM method provides to shape ceramics more rapidly [53, 54].

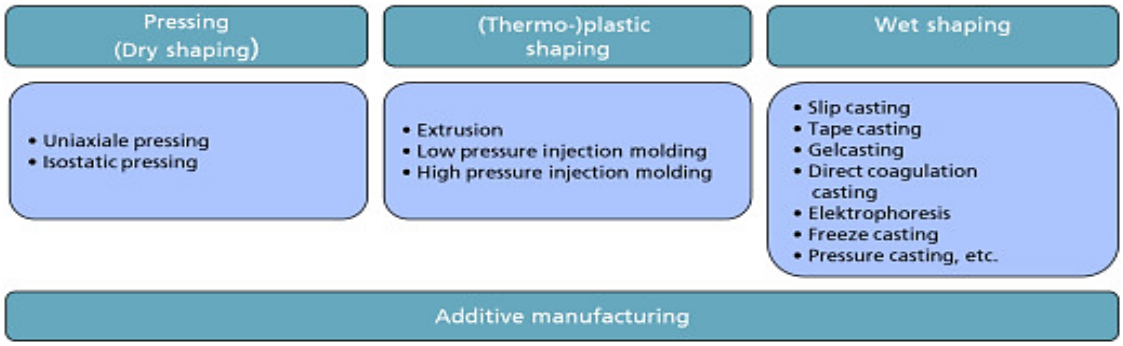

Figure 1.9 Ceramic forming methods [51]



Figure 1.10 Ceramic products formed by gel casting [52]

Table 1.2 The comparison between gel casting and other traditional ceramic forming processes [47]

Property	**Gel casting**	**Slip casting**	**Injection molding**	**Pressure casting**
Molding time	5-60 minutes	1-10 hours	10-60 seconds	10 minutes- 5 hours
Strength (dried)	Very high	Low	N/A	Low
Mold materials	Metal, glass, polymer, wax	Plaster	Metal	Porous plastic
Binder burnout	2-3 hours	2-3 hours	7 days	2-3 hours
Molding defects	Minimal	Minimal	Significant	Minimal
Maximum part dimension	>1 meter	>1 meter	About 30 cm, 1 dimension must =<1 cm	About 1 meter

Table 1.3 (continued) The comparison between gel casting and other traditional ceramic forming processes [47]

Property	Gel casting	Slip casting	Injection molding	Pressure casting
Warpage during drying/ binder burnout	Minimal	Minimal	Possibly be severe	Minimal
Thick/thin sections	Both are OK	Thick section needs longer casting time	Problem with binder removal for thick section	Thick section needs longer casting time
Advantages	Inexpensive molds, Manufacturing of hallow and solid as well as complex parts, High green density and stiffness	Inexpensive molds, Manufacturing of hallow and solid parts	Mass production of complex parts	Inexpensive molds, Less molding time
Disadvantages	Binder removal prior to sintering	Large tolerances	Binder removal prior to sintering	Limited part size

1.4 Literature Review on Aluminum Borate Ceramics

Ray [4] synthesized Al borate powders mixing 9 moles Al_2O_3 and 2 moles B_2O_3 (i.e., stoichiometric ratio). It was reported that formation of A_9B_2 phase totally took place at 1100°C with a trace amount of α-Al_2O_3. The samples sintered without any sintering additive did not achieve adequate densification (e.g., a relative density of 61.2%) while a relative density of 97.6% was obtained for the samples with 1 wt% CaO and sintered at 1450°C for 1 h. CaO caused liquid phase sintering (likely by forming $CaAl_2B_2O_7$ phase that melted at 1098°C) and enhanced densification. Flexural strength of 242 MPa and hardness of 11 GPa were obtained. The mean thermal expansion coefficients were measured as $3.8x10^{-6}$/°C (24-227°C) and as $5.1x10^{-6}$/°C (24-827°C). The dielectric constant of the sample sintered at 1350°C for 1 h with 2 wt% CaO was measured as 5.6 at 2 MHz. Samples without any additive were also prepared by hot pressing at 1100°C and densified to 99.6% relative density. Flexural strength of 310-324 MPa, hardness of 13-14 GPa, thermal expansion coefficients of $3.5x10^{-6}$/°C (24-227°C) and $4.2x10^{-6}$/°C (24-827°C) were obtained. The relative densities were 94.1% and 96.6% for the samples prepared with 4 wt% $CaAl_2B_2O_7$ (sintered at 1350°C for 1h) and 1 wt% MgO (sintered at 1450°C for 1h), respectively.

Hernandez et al. [55] prepared monolithic porous $Al_{18}B_4O_{33}$ ceramics for structural, insulating or filtering applications by reactive sintering mixture of calcined Al_2O_3 and H_3BO_3 prepared at various ratios of 13 (A_9B_2), 20.5 and 26 (A_2B) wt% B_2O_3. They reported for the 26.0 wt% B_2O_3 composition that Al_2O_3, $2Al_2O_3.B_2O_3$ and $Al_{18}B_4O_{33}$ were all present between 800°C and 1000°C, and phase-pure $Al_{18}B_4O_{33}$ was obtained at T≥1300°C. $Al_4B_2O_9$ was found to be an intermediate phase. All tree compositions had open porosities between 35% and 50% after being sintered between 1100°C-1400°C due to needle-like form of the Al borate powders. Stoichiometric A_9B_2 and A_2B mixtures exhibited the highest porosity. The sample with 20.5 wt% B_2O_3 and sintered at 1200°C for 2h had the highest diametric compression strength of 16.2 MPa. These porous structures were offered to be infiltrated by molten aluminum or aluminum alloys for metal-ceramic composites.

Hernandez et al. [56] also prepared dense A_9B_2 ceramics using calcined Al_2O_3 and H_3BO_3. The powders were mixed, then calcined at 1200°C for 1 h, and finally attrition-milled to break whisker particles up to aspect ratios between 1 and 4. Dry-pressed $Al_{18}B_4O_{33}$ ceramics started to decompose at T≥1350°C and only Al_2O_3 phase remained after sintering at 1400°C. The best densification was obtained at 1300°C for 5 h (2.52 gr/cm^3 with open porosity of 10.91 %). The Vickers hardness of 6.12 GPa was measured.

Al_2O_3 and Al borate composite structures were fabricated by reaction sintering of calcined alumina and H_3BO_3 in air (initial B_2O_3 amounts were 13 wt% and 26 wt%, corresponding to almost A_9B_2 and A_2B phases given in Figure 1.1, respectively) [16]. The ceramics with 13 wt% B_2O_3 and sintered at 1300°C for 2 h had a density of 1.91 g/cm3 (39.3 % open porosity), a crystalline phase ratio (as wt%) of $Al_2O_3/A_9B_2/A_2B$ =58/42/trace, and an effective thermal conductivity (i.e., calculated using parallel mixing rule) of 6.9 W/m.K. The ceramics with 26 wt% B_2O_3 and sintered at 1300°C for 2 h had a density of 1.75 g/cm^3 (45.4 % open porosity), a crystalline phase ratio (as wt%) of $Al_2O_3/A_9B_2/A_2B$ =0.7/97.4/1.9, and an effective thermal conductivity of 2.7 W/m.K. The diametral compression test was used to evaluate mechanical strength (σ_d) and the apparent Young modulus (E_d) of the ceramics. The ceramics with 13 wt% B_2O_3 had σ_d=6.4 MPa and E_d=590 MPa while the ceramics with 26 wt% B_2O_3 and σ_d=9.9

MPa and E_d=980 MPa. Particularly, the ceramics with 26 wt% B_2O_3 was offered for insulating applications due to higher mechanical properties and lower thermal conductivity.

1.5 Objective

Aluminum borate ($Al_{18}B_4O_{33}$) has attractive properties for structural and functional applications due to its low density (2.93 g/cm^3), low thermal expansion coefficient (4.5×10^{-6}/^{o}C axial and 1.9×10^{-6}/^{o}C radial), high Young's modulus (400 GPa), and low dielectric constant (5.6). However, needle-shape $Al_{18}B_4O_{33}$ particles make particle packing and sintering difficult to fabricate dense ceramics. Therefore, various additives such as mullite, glass and CaO were used to facilitate densification of the Al borate ceramics. The aim of this thesis was to synthesize Al borate powders by solid state calcination of Al_2O_3 and domestic source of B_2O_3, and then to fabricate Al borate ceramics with and without CaO additive, Al borate-glass and Al borate-mullite-glass composites by gel casting method, and finally to investigate phase formation, densification, microstructure evolution, mechanical properties (hardness), dielectric properties (dielectric constant and loss) and thermal properties (thermal conductivity). Particularly, Al borate-glass and Al borate-mullite-glass composites were investigated for the first time in literature. Colloidal processing (e.g., gel casting) was preferred to improve powder compaction and enhance densification as well as to fabricate ceramics in complex shapes. Physical properties were evaluated to comply with some potential structural and functional applications such as thermal insulator, filter, radome and low dielectric constant electronic substrates.

CHAPTER 2

EXPERIMENTAL METHODS

Alumina (α-Al_2O_3, Almatis, CT 3000 SG) and boron oxide (B_2O_3, Eti Maden, 98%) were used as starting materials to synthesize aluminum borate ($9Al_2O_3.2B_2O_3$) powders. The physical properties of Al_2O_3 are given in Table 2.1. A binder burnout process for spray-granulated Al_2O_3 powder was applied at 600°C for 30 minutes to remove binder. Then, it was ball milled in ethanol for 24 h using ZrO_2 balls to reduce particle size. Since B_2O_3 has an ability to absorb moisture from air, a TG/DTA (Hitachi STA7300) analysis was done for B_2O_3 and weight loss (or, moisture content) was measured as a function of temperature at a heating rate of 5°C/min before starting experiments. After that, Al_2O_3/B_2O_3 powder mixtures at various mole ratios, determined based on Figure 1.1 and tabulated in Table 2.2, were prepared in ethanol by ball milling for 24 h. Ethanol was evaporated during stirring to avoid preferential settling of the powders due to density differences in the mixtures. Prepared mixtures were dried at 40°C for 24 h, then, the mixtures were calcined at 1300°C for 1 h in open-lid Al_2O_3 crucibles at a heating rate of 5°C/min. Calcination was also performed at 1100, 1200 and 1400°C for 1 h to observe temperature effect on phase evolution for the optimum powder mixture. Weights of the mixtures before and after calcination were measured and weight changes were calculated. Phase formation was determined using an XRD (Rigaku, Miniflex600) with Cu Kα radiation between 20-60° with a step size of 0.02° and scan rate of 2°/min. Calcined loose powders were crushed in ethanol using mortar and pestle, and then dried at 40°C for 24 h. Finally, powders were sieved thru a 70 μm sieve.

Table 2.1 Properties of Al_2O_3 powder [57]

Properties	**Value**
Specific surface area (m^2/g)	7.5
Particle size (μm)	
d_{50}	0.5
d_{90}	2

Table 2.1 (continued) Properties of Al_2O_3 powder [57]

Properties	**Value**
Chemical analysis (%)	
Al_2O_3	99.78
Na_2O	0.08
Fe_2O_3	0.02
SiO_2	0.03
CaO	0.02
MgO	0.07
Ceramic Properties	
Density (at 90 MPa) (g/cm^3)	3.9
Firing temperature (°C) (1 h soak time)	1540
Shrinkage (%)	16.8

Table 2.2 Mole ratios of Al_2O_3/B_2O_3 and amounts of B_2O_3 used in the powder mixtures

Mixture numbers	**Mole Ratios (Al_2O_3/B_2O_3)**	**B_2O_3, wt%**
M1	5.73	10.7
M2	4.41	13.4
M3	3.09	18.1
M4	1.77	27.9
M5	1.30	34.4
M6	0.87	44.0
M7	0.58	54.1

Four different ceramic compositions were prepared;

- a mixture of 2 wt% CaO (in the form of $CaCO_3$) + $Al_{18}B_4O_{33}$ powders (hereafter designated as AB)
- a mixture of 35 wt% $Al_{18}B_4O_{33}$ + 35 wt% mullite (M72, Nabaltec) + 30 wt% glass (Akkim, Turkey) (hereafter designated as AMG)

- as-synthetized $Al_{18}B_4O_{33}$ (hereafter designated as PAB)
- a mixture of 70 wt% $Al_{18}B_4O_{33}$ + 30 wt% glass (hereafter designated as ABG).

The physical properties of the mullite powder are given in Table 2.3. Mullite powder was ball milled in DI water for 24 h using 5 mm ZrO_2 balls to decrease particle size before mixing with $Al_{18}B_4O_{33}$ powders. The composition of the commercial glass is given in Table 2.4. Glass frit was ball milled in ethanol for 48 h using 5 mm ZrO_2 balls. Particle size distribution was measured by a laser particle size analyzer (Mastersizer2000, Malvern). Microstructure and elemental distribution of powders and fractured surfaces of the ceramics were examined by a field emission Scanning Electron Microscopy equipped with an Energy Dispersive Spectroscopy (SEM-EDS, Hitachi SU5000).

Table 2.3 Properties of the mullite powder [58]

Properties	**Values**
Mineralogical composition	90-95 % mullite 5-10 % glassy phase 1 % Al_2O_3
Specific density (g/cm^3)	3.13
Chemical composition	72% Al_2O_3 26% SiO_2 0.3% Fe_2O_3 0.2% TiO_2 0.05% CaO 0.1% MgO 0.2% Na_2O 0.6% K_2O
d_{50}, μm	3-5

Table 2.4 Composition of the glass phase [59]

Composition	**SiO_2**	**Al_2O_3**	**CaO**	**Na_2O**	**K_2O**
wt %	65.8	15.1	11.7	4.0	3.4

Green ceramics were prepared by gel casting method and mixing amounts of chemical constituents used in the AB, AMG, PAB and ABG samples are given in Table 2.5. Firstly, 2 wt% dispersant (40 wt% ammonium salt of polyacrylic acid, Coatex P90)

adjusted to dry weight percent of the total powder and a 14 wt% monomer solution containing Acrylamide (AM) (Sigma, 40 wt% solution, C_3H_5NO) and Methylenebiacrylamide (MBAM) (Sigma-Aldrich, $C_7H_{10}N_2O_2$) prepared at a ratio of AM/MBAM=20 was added to powder mixture and mixed in a speed mixer (SpeedMixer™, DAC 150.1 FVZ) at 3500 rpm for 5 minutes. A 3 wt% Ammoniumpersulfate (APS) ($(NH_4)_2S_2O_8$, Sigma-Aldrich) solution was admixed as a reaction initiator and mixed at 3500 rpm for additional 5 minutes. Finally, tetramethylethylenediamine (TEMED) ($C_6H_{16}N_2$, Sigma-Aldrich) was admixed as a reaction catalyzer and mixed at 1000 rpm for additional 10 seconds. The prepared slurries were slowly poured into the molds made from aluminum foils to shape green samples. The slurries were cured for 3 minutes in air, for between 3 and 20 minutes at 40°C, and finally cured at 70°C for 1 h. Water in the green samples was removed slowly in a drying oven. This process was done between 40°C and 70°C by increasing temperature at a rate of 10°C/12 h. Burnout process was carried out for dried green samples at a rate of 0.1°C/min at 600°C for 60 minutes with an intermediate step, as given in Figure 2.1.

Table 2.5 Amount of chemical constituents used in gel casting

Nomenclature	**AB**	**AMG**	**PAB**	**ABG**
Powders, gr	$Al_{18}B_4O_{33}$: 10 $CaCO_3$: 0.3569	Mullite: 7 $Al_{18}B_4O_{33}$: 7 Glass: 6	$Al_{18}B_4O_{33}$: 10	$Al_{18}B_4O_{33}$: 7 Glass: 3
Monomer solution, gr	4.594	9.188	4.594	4.594
Dispersant, gr	0.4	0.26	0.4	0.4
Initiator, µL	153	306	153	153
Catalyzer, µL	2	2	2	2

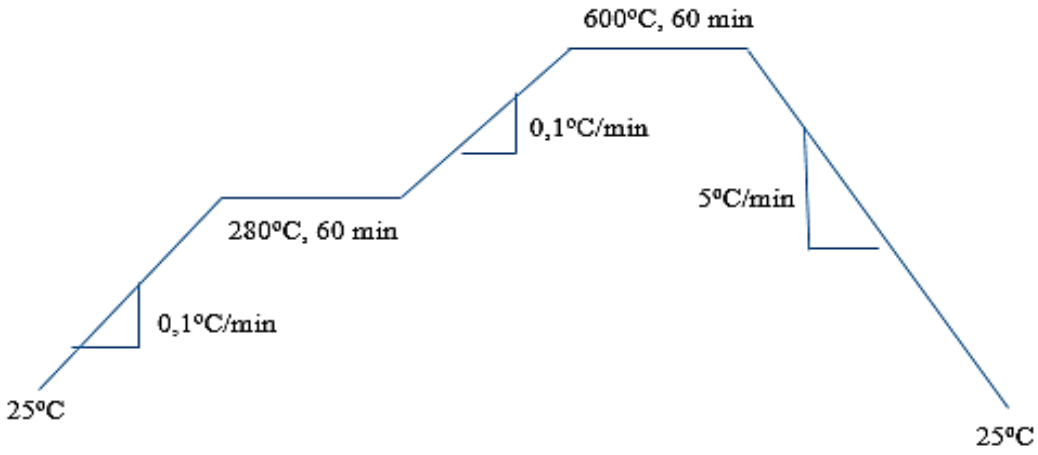

Figure 2.1 Burnout schedule of the green samples

Then, the PAB and ABG samples were sintered at 1350°C, the AB and AMG samples were sintered at 1300°C, 1350°C and 1400°C for 1 h in air at a heating rate of 5C/min. Weights of the samples before and after sintering were measured and weight loss of samples were calculated. Densities of the samples after sintering were calculated by Archimedes' method and equations are given below [60];

$$B.D = [\frac{Wa}{Wb-Wx}] \times d \quad \textbf{(2.1)}$$

$$A.P\ (\%) = [\frac{We-Wa}{We-Wx}] \times 100 \quad \textbf{(2.2)}$$

$$W.A = = \frac{We - Wa}{Wa} \quad \textbf{(2.3)}$$

where W_a is dried weight (gr), W_x is weight of sample in liquid (gr), W_e is weight of sample impregnated with water (gr), and d is density of water at the measurement condition (g/cm^3), B.D. is bulk density, A.P is apparent (open) porosity (%) and W.A is water absorption (%).

Dielectric properties were measured by an impedance analyzer at 5 MHz (Hioki M3570). Firstly, parallel surfaces of the samples were coated with Ag paste and then baked at 600°C for 15 min. The dielectric constant was determined from capacitance measurement at room temperature according to the following formula [61];

$$K = \frac{C.d}{\varepsilon_0.A} \quad (2.4)$$

where K is dielectric constant, C is capacitance (F), d is thickness of specimen (m), ε_0 is permittivity of vacuum (8.8542x 10^{-12} F/m) and A is area of specimen (m^2). Thermal conductivity together with thermal diffusivity and specific heat were directly measured at room temperature using a single-sided testing configuration (Hot Disk, TPS 3500). Single-sided testing method based on transient plane source technique uses a sensor sandwiched in-between two samples halves. Known insulation material is used as sensor support in this technique. Hardness of the sintered samples were measured by Micro Vickers hardness tester (Shimadzu HMV-G) applying 20 N load for 10 seconds. Before measurements, samples were ground at 120, 240, 320, 400, 600, 800, 1000 grit SiC papers by a grinding machine. Finally, samples were polished with 3 μm and 1 μm diamond cloths. Vickers hardness was determined according to ISO 6507-1:2005 standard as given in the below equation;

$$H = 01891 \frac{P}{a^2} \quad (2.5)$$

where H is Vickers hardness, P is test force (N) and a is average length of diagonal lines of the indentation marks (mm).

CHAPTER 3

RESULTS AND DISCUSSION

3.1 Powder Synthesis and Phase Formation

Alumina (Al_2O_3) and boron oxide (B_2O_3) mixtures prepared at various mole ratios were used to synthesize Al borate ($Al_{18}B_4O_{33}$ or $9Al_2O_3.2B_2O_3$ or A_9B_2) powder. The commercial spray-granulated Al_2O_3 powder was first burnout and then ball milled for particle size reduction [60]. The particle size result shown in Figure 3.1 indicates a slightly bimodal distribution. The particle size of Al_2O_3 decreased from d_{50}=0.5 µm to 0.44 µm and from d_{90}=2.0 µm to 1.17 µm when compared with the Al_2O_3 datasheet given in Table 2.1.

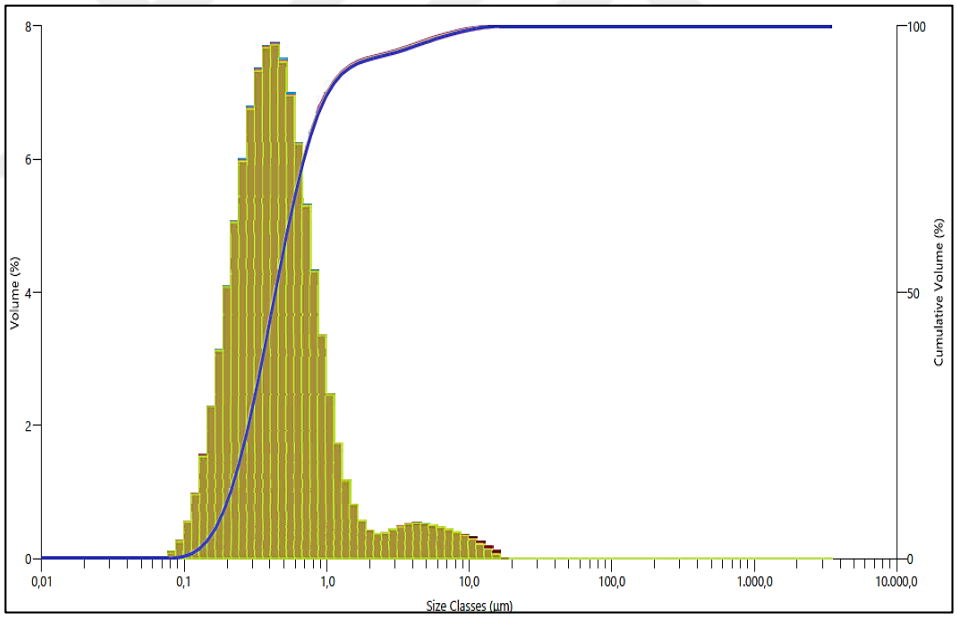

Figure 3.1 Particle size distribution of Al_2O_3 powder after ball milling for 24 hours [59]

A possibility of B_2O_3 to absorb moisture from air was first considered because, when it is exposed to air atmosphere, it absorbs water slowly thereby reverting to boric acid (H_3BO_3).

In the H_3BO_3 structure, H_2O constitutes 43.7 wt%. Figure 3.2 shows XRD pattern of initial B_2O_3 powder. XRD pattern indicated that initial B_2O_3 (Card no: 00-006-0297)

absorbed some moisture, resulting in partial conversion to the H_3BO_3 (Card no: 00-023-1034). A background hump was also evident due to the amorphous glassy nature of B_2O_3 [62]. Therefore, a TG-DTA analysis was then carried out to determine the amount of water absorbed, and the result is shown in Figure 3.3. There were two endothermic peaks located at 106°C and 162°C, corresponding to weight losses due to the multiple-stage decomposition of H_3BO_3 [55];

$$H_3BO_3 \rightarrow HBO_2 + H_2O \quad \textbf{(3.1)}$$

$$4HBO_2 \rightarrow H_2B_4O_7 + H_2O \quad \textbf{(3.2)}$$

$$H_2B_4O_7 \rightarrow 2B_2O_3 + H_2O \quad \textbf{(3.3)}$$

Majority of the weight loss took place below nearly 200°C, and then gradually continued up to nearly 300°C. The total amount of weight loss was measured as 21.38 wt% and then it remained almost constant between 300°C and 800°C. The amount of absorbed H_2O was 21.38 wt%, meaning that H_3BO_3 was partially formed. Therefore, exact amount of B_2O_3 at preparing all batch mixtures given in Table 2.2 was determined excluding the initially absorbed H_2O content.

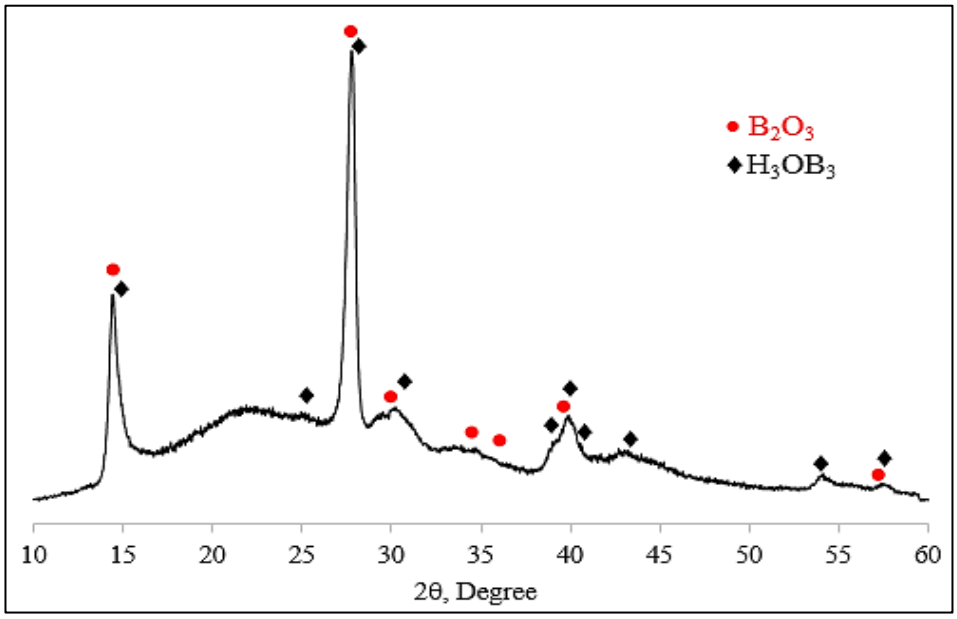

Figure 3.2 XRD pattern of initial B_2O_3 powder

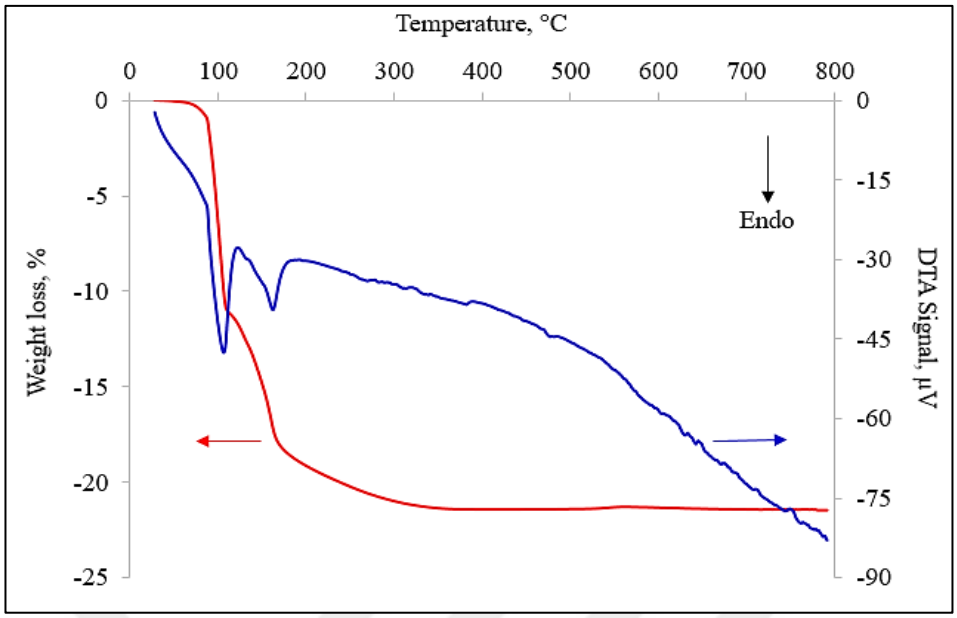

Figure 3.3 The TG-DTA analysis of the initial B_2O_3 powder

Al borate was reported to begin decomposition at temperatures over 1350ºC [56]. It was also reported for the 26.0 wt% B_2O_3 composition that Al_2O_3, $Al_4B_2O_9$ (or A_2B) as an intermediate phase and $Al_{18}B_4O_{33}$ (or A_9B_2) were all present between 800ºC and 1000°C, and a phase-pure $Al_{18}B_4O_{33}$ was obtained at T≥1300°C [55]. Therefore, to achieve complete Al borate formation without decomposition, the calcination temperature was initially set to 1300ºC for 1 h. The prepared powder mixtures are marked on the phase diagram and shown in Figure 3.4 for better comparison of the results. The compositions were chosen to cover the regions of incongruently melting A_9B_2 (13.17 wt% B_2O_3) and/or A_2B (25.45 wt% B_2O_3) phases together with Al_2O_3.

ZrO_2 milling media is mostly used during ball milling due to their higher density and toughness for an effective particle size reduction but it was reported that ZrO_2 contaminated A_9B_2 powder during attrition milling [56]. Therefore, the powder mixture prepared at an Al_2O_3/B_2O_3 mole ratio of 5.73 (10.7 wt% B_2O_3) was first ball milled with ZrO_2 balls and its XRD pattern is shown in Figure 3.5. XRD analysis shows that ZrO_2 (Card no: 17-0923) was present as an impurity phase introduced from the ZrO_2 milling media. The same batch was then prepared using Al_2O_3 balls to eliminate impurity incorporation arising from the ZrO_2 balls and Figure 3.6 shows that ZrO_2 contamination was totally eliminated. Moreover, XRD patterns indicate that both $Al_{18}B_4O_{33}$ (Card no: 00-032-0003) and Al_2O_3 (Card no: 00-010-0173) phases were

obtained, which complied with the stable phases in the binary phase diagram given in Figure 3.4. Then, other Al_2O_3/B_2O_3 mixtures marked on Figure 3.4 were prepared consecutively using Al_2O_3 balls and calcined at 1300°C for 1 h to observe Al borate phase formation in the deficiency and excess of B_2O_3 with respect to the stoichiometric $Al_{18}B_4O_{33}$ phase with a mole ratio of 4.5 (13.17 wt% B_2O_3).

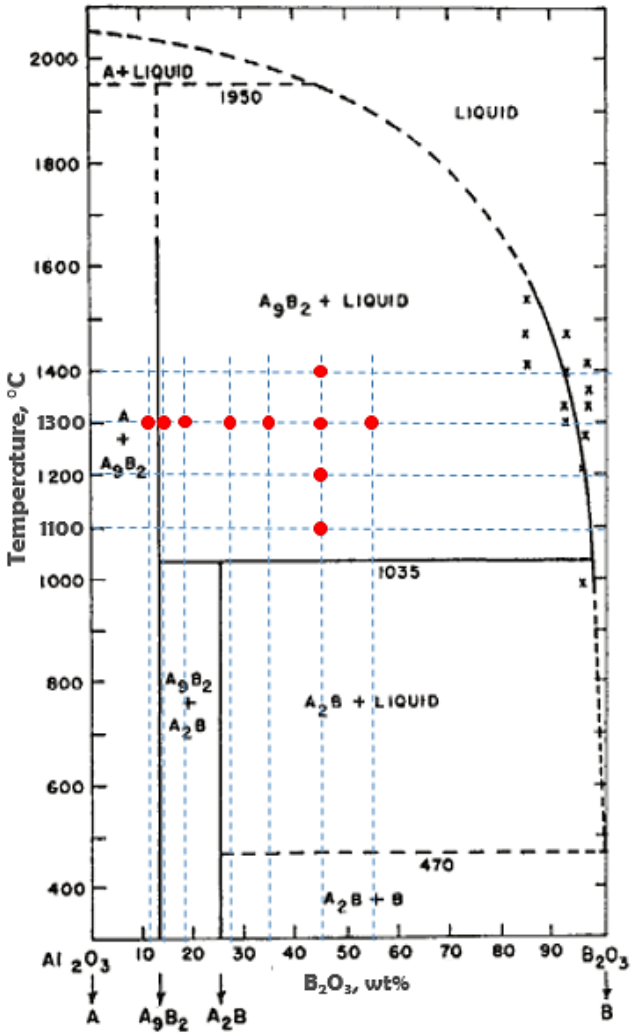

Figure 3.4 The prepared powder mixtures marked on the phase diagram [1]

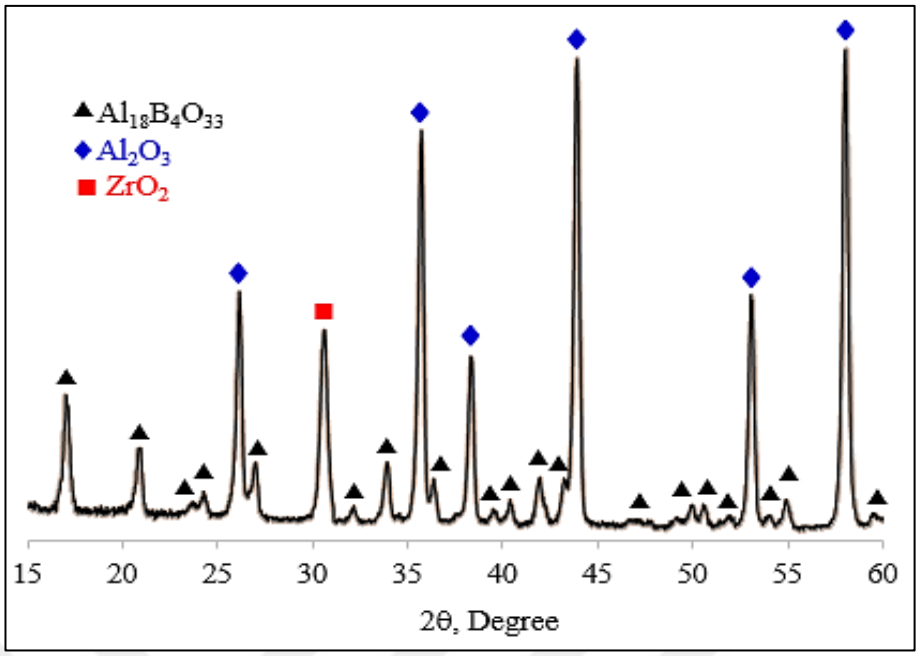

Figure 3.5 XRD pattern of the mixture at a mole ratio of 5.73 (10.7 wt% B_2O_3) prepared by ZrO_2 balls

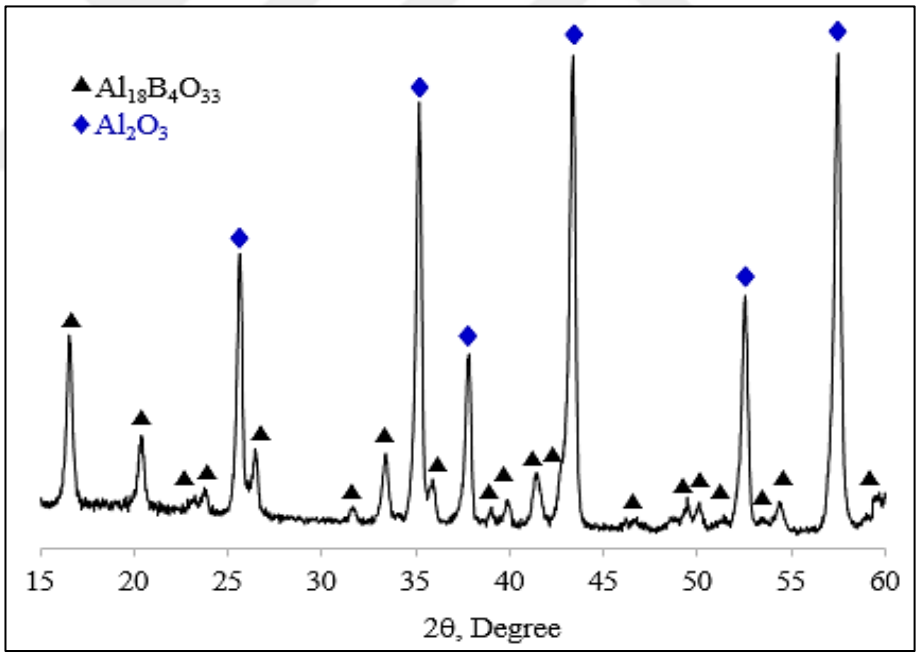

Figure 3.6 XRD pattern of the mixture at a mole ratio of 5.73 (10.7 wt% B_2O_3) prepared by Al_2O_3 balls

Figure 3.7 shows the XRD pattern of the mixture prepared at a mole ratio of 4.41 (13.4 wt% B_2O_3). Although a near-stoichiometric mole ratio was used (e.g., 13.17 wt% B_2O_3), mainly unreacted Al_2O_3 together with $Al_{18}B_4O_{33}$ were obtained, instead of only $Al_{18}B_4O_{33}$ phase according to the phase diagram.

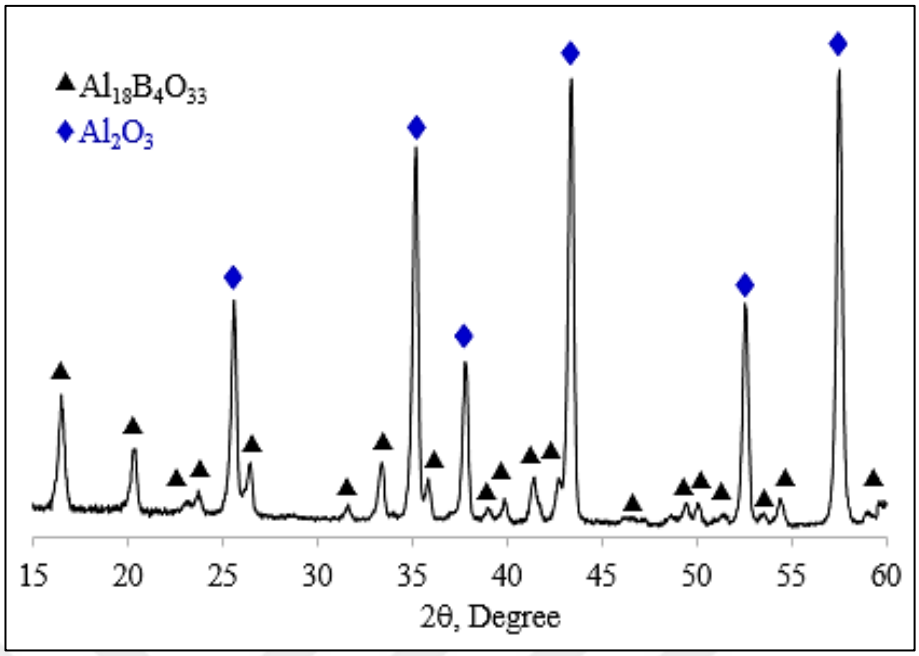

Figure 3.7 XRD pattern of the mixture at a mole ratio of 4.41 (13.4 wt% B_2O_3)

Figure 3.8 shows the XRD pattern of the mixture prepared at a mole ratio of 3.09 (18.1wt% B_2O_3). Intensity of the main $Al_{18}B_4O_{33}$ peak relatively increased and main Al_2O_3 peak begun to decrease when the B_2O_3 amount was increased, but Al_2O_3 was still the dominant phase. In Figure 3.9 (mole ratio 1.77 with 27.9 wt% B_2O_3) and Figure 3.10 (mole ratio 1.3 with 34.4 wt% B_2O_3), the main peaks belonged to $Al_{18}B_4O_{33}$ but some unreacted Al_2O_3 were also present. These results indicate that pure $Al_{18}B_4O_{33}$ phase was not obtained even though they were calcined at 1300°C with excess B_2O_3 up to 34.4 wt%.

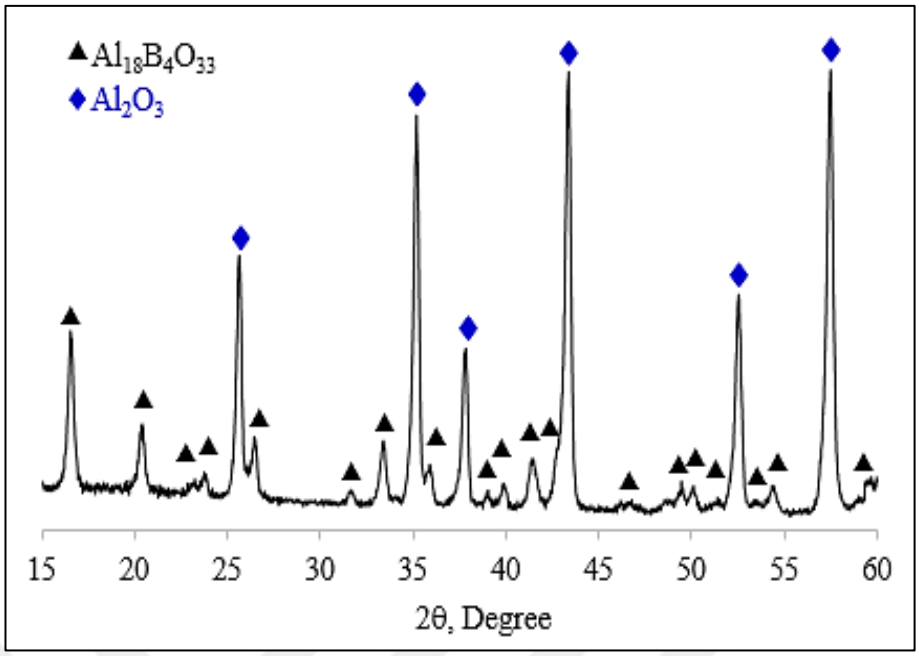

Figure 3.8 XRD pattern of the mixture at a mole ratio of 3.09 (18.1 wt% B_2O_3)

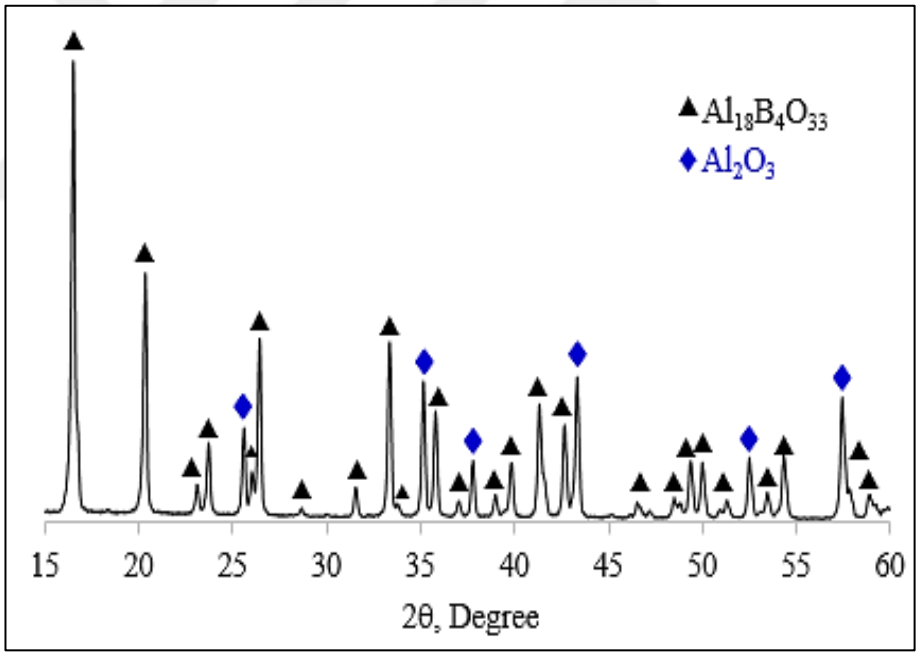

Figure 3.9 XRD pattern of the mixture at a mole ratio of 1.77 (27.9 wt% B_2O_3)

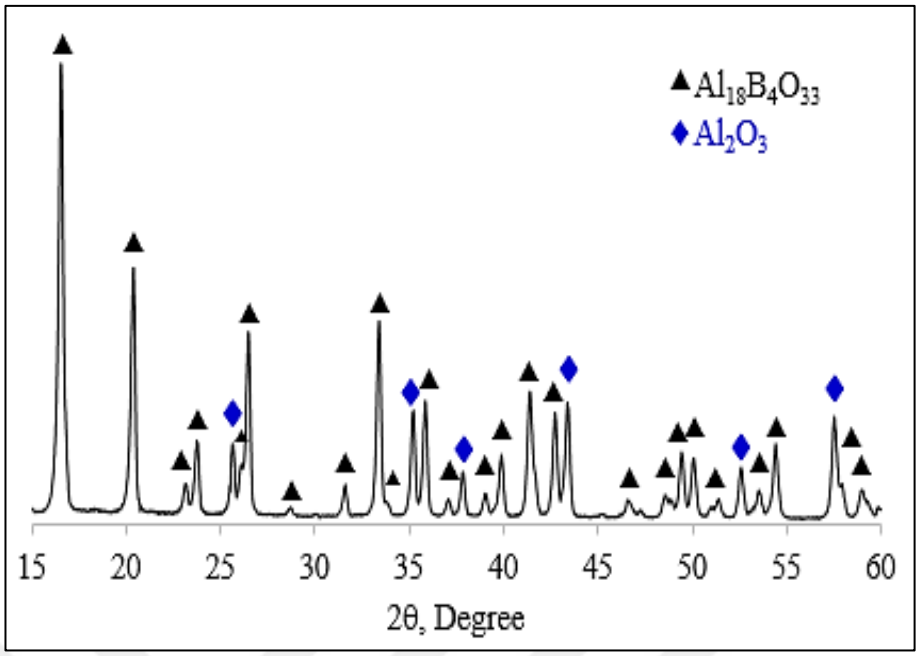

Figure 3.10 XRD pattern of the mixture at a mole ratio of 1.3 (34.4 wt% B_2O_3)

Figures 3.11 and 3.12 show the XRD patterns of the mixtures prepared at a mole ratio of 0.87 (44 wt% B_2O_3) and 0.58 (54.1 wt% B_2O_3), respectively. Although $Al_{18}B_4O_{33}$ was fully formed, a trace amount of B_2O_3 was present but it was more prevalent in Figure 3.12, which indicates that the saturation limit of Al_2O_3 and/or intermediate aluminum borate compounds in the B_2O_3-based liquid is between 34.4 and 44 wt% B_2O_3 present in the initial mixture. In fact, it is better to attribute this phase as a B_2O_3-based liquid phase because its main peaks located at 2θ=27.92-27.94° were slightly different from 2θ=27.77° for pure B_2O_3 (Card no: 00-006-0297).

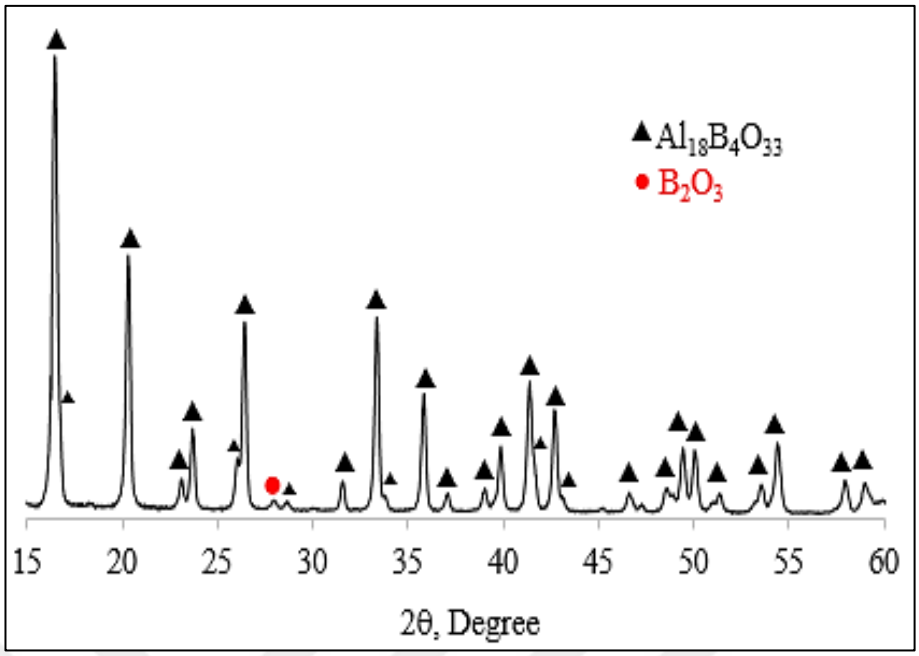

Figure 3.11 XRD pattern of the mixture at a mole ratio of 0.87 (44 wt% B_2O_3)

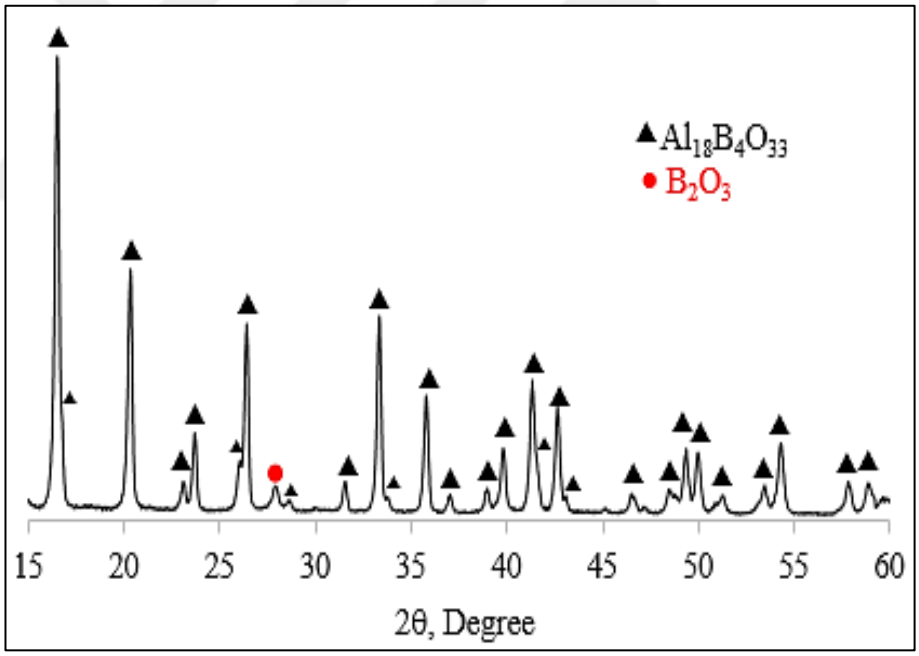

Figure 3.12 XRD pattern of the mixture at a mole ratio of 0.58 (54.1 wt% B_2O_3)

All XRD patterns for the prepared powder mixtures calcined at 1300°C for 1h are compared in Figure 3.13. As the amount of B_2O_3 increased, the amount of unreacted Al_2O_3 decreased and $Al_{18}B_4O_{33}$ phase became the main phase in the mixtures. According to the phase diagram (see Figure 3.4), ($Al_{18}B_4O_{33}$+Liquid) phases are present at 1300°C for all compositions except 10.7 wt% B_2O_3 for which

($Al_{18}B_4O_{33}$+Al_2O_3) phases are present. Solid state synthesis of $Al_{18}B_4O_{33}$ was completed and an optimum Al_2O_3/B_2O_3 mole ratio was determined as 0.87 (e.g., 44 wt% B_2O_3) after calcination at 1300°C for 1 h, which deviated from the stoichiometric mole ratio of 4.5 (e.g., 13.17 wt% B_2O_3). Hernandez et al [55] also reported an incomplete phase formation for the stoichiometric composition (e.g., 13.17 wt% B_2O_3), yielding 58% Al_2O_3 + 42% $Al_{18}B_4O_{33}$ after sintering at 1300°C. Almost pure $Al_{18}B_4O_{33}$ (together with 0.3% Al_2O_3 and 0.2% A_2B) was obtained at T=1400°C for the 26.0 wt% B_2O_3 composition, which indicates that excess B_2O_3 is required for full phase formation.

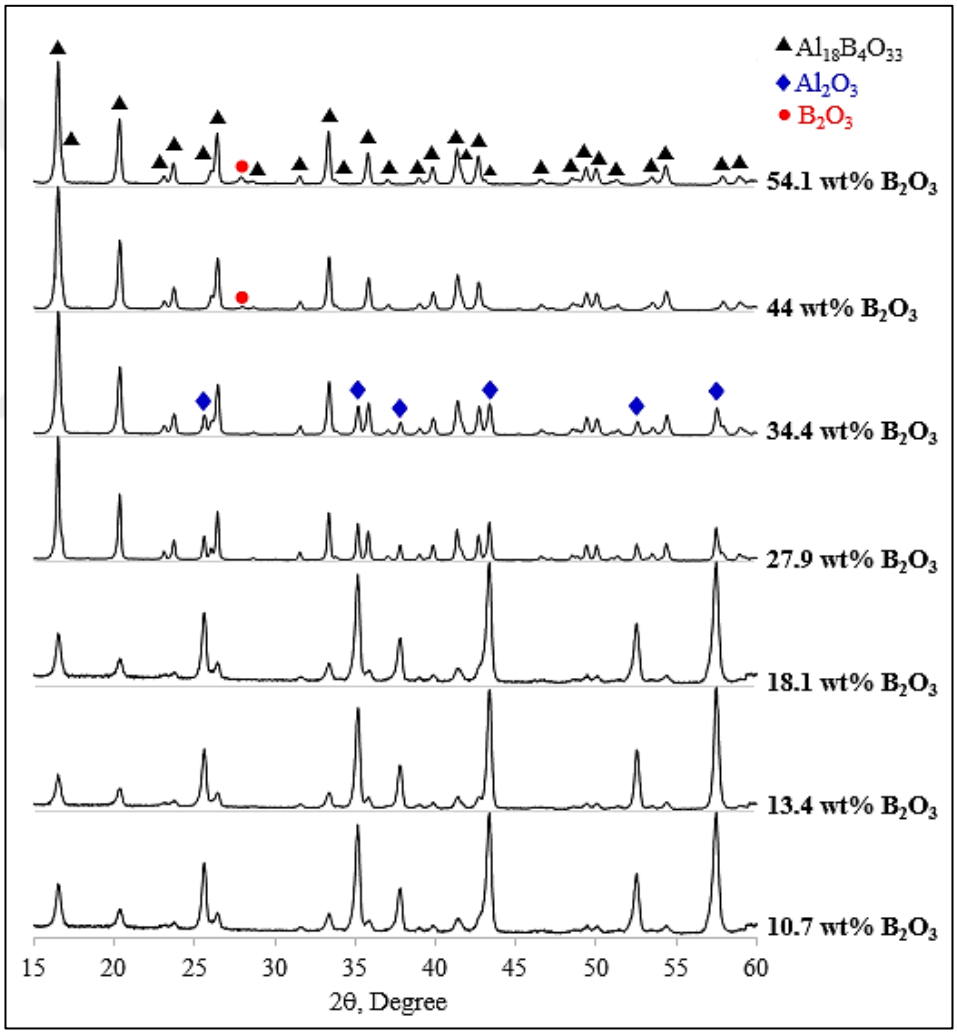

Figure 3.13 XRD patterns of all prepared compositions calcined at 1300°C for 1h.

The powder synthesis experiments were carried out in the Al_2O_3 crucibles without any covering lids to prevent evaporation as well as without a quenching step to freeze out

high temperature phases at room temperature, as compared to the totally closed-lid crucibles followed by a quenching step to determine equilibrium phases in the phase diagrams [1]. Weight loss due to the B_2O_3 evaporation could be possible and hence a TG-DTA analysis of the powder mixture with 44 wt% B_2O_3 was conducted to observe weight change as a function of temperature and is shown in Figure 3.14. The weight loss including absorbed H_2O evaporation (or, alternatively, decomposition of boric acid) was about 18.17% up to 1100°C, and then it started losing weight continuously with increasing temperature. The amount of B_2O_3 (or B_2O_3-based liquid) evaporation during thermal treatment was also reported to be null or negligible up to 1100°C [55]. With respect to the 18.17% base line at 1100°C, the relative weight loss was 0.58% at 1200°C, 1.26% at 1250°C, 2.33% at 1300°C, 3.92% at 1350°C, 6.15% at 1400°C and 7.45% at 1425°C. Note that a weight loss of 21.38% below 800°C for initial B_2O_3 (Figure 3.3) was higher than 18.17% for the 44 wt% B_2O_3 powder mixture (Figure 3.14) because of the evaporation of some absorbed H_2O during oven drying (e.g., 1 day at 40°C) before calcination in the latter. Hoffman et al. [3] also reported the formation of aluminum-rich phases due to loss of highly volatile B_2O_3 upon extended heating period up to 14 days during powder synthesis, even though the synthesis experiments were carried out in covered platinum crucibles.

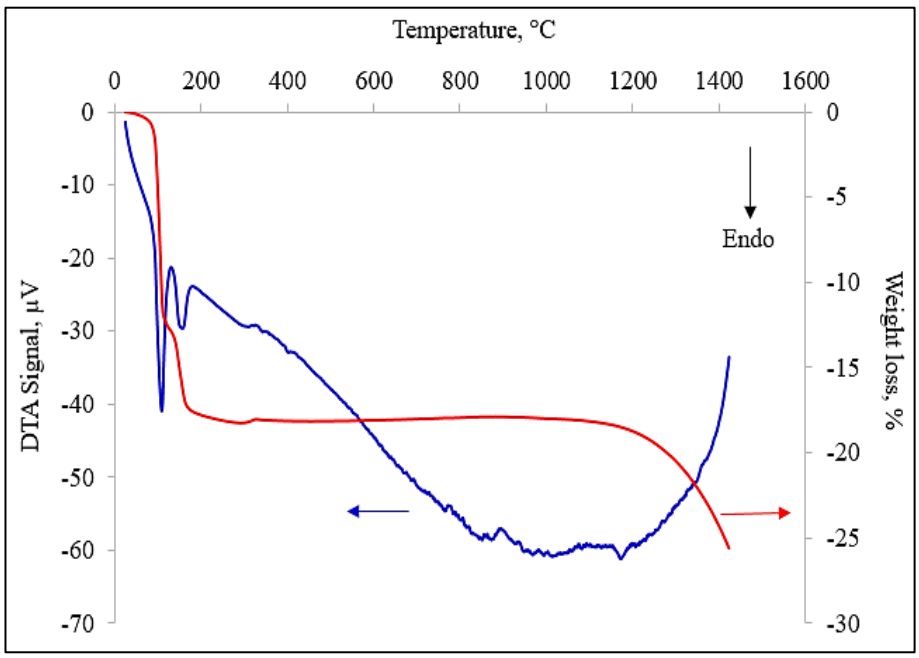

Figure 3.14 TG-DTA analysis of the powder mixture at a mole ratio of 0.87 (44 wt% B_2O_3)

The powder mixture prepared at a mole ratio of 0.87 (44 wt% B_2O_3) were further calcined at 1100°C, 1200°C, 1300°C and 1400°C for 1 h (also marked on Figure 3.4) to investigate calcination temperature effect on the $Al_{18}B_4O_{33}$ phase formation. Figure 3.15 compares their XRD patterns. $Al_{18}B_4O_{33}$ was partially formed at 1100°C and some unreacted Al_2O_3 also remained in the mixture. In addition, intermediate $Al_4B_2O_9$ phases (Card no: 00-029-0010 (■) and Card no: 01-079-1477 (□)) together with some unknown peaks as-shown by arrows also formed, although only $Al_{18}B_4O_{33}$ should form according to the phase diagram given in Figure 3.4. The main peak of the unknown phase was located at 2θ=34.28°. In fact, Hoffman et al. [3] also observed a phase at around 2θ=34.5°for the 5 wt% B_2O_3 composition treated at 950°C for 72 h and could not assign it to any phase. Unknown peaks might be attributed to phase(s) solidified from a B_2O_3-based liquid composition having various amounts of dissolved Al_2O_3 and/or intermediate aluminum borate compounds at different Al_2O_3/B_2O_3 mole ratios because a eutectic B_2O_3-$Al_4B_2O_9$ phase melting at 449 ºC to form a B_2O_3-rich liquid phase was reported [56]. $Al_{18}B_4O_{33}$ formation was completed at T≥1200°C in the resolution limit of the XRD analysis. As temperature increased, intermediate $Al_4B_2O_9$ phases transformed to $Al_{18}B_4O_{33}$ (see Equation 1.1). The unknown phase was totally disappeared most probably by means of either crystallization directly to $Al_{18}B_4O_{33}$ or first forming intermediate $Al_4B_2O_9$ and then transforming to $Al_{18}B_4O_{33}$. The weight losses after calcination with respect to a reference loss value recorded at 1100°C were 0.57% at 1200°C and 6.51% at 1400°C, that are almost compatible with the loss values obtained from Figure 3.14 (e.g., 0.58% at 1200°C and 6.15% at 1400°C) although the former had a dwell time of 1 h at each calcination temperature with respect to a continuous heating under flowing air in the latter at the same heating rate of 5°C/min. Al_2O_3 peaks were not observed even at 1400°C in spite of 6.51% weight loss, indicating that $Al_{18}B_4O_{33}$ was stable at 1400°C. Due to the presence of excess B_2O_3 in the starting powder mixture, the evaporation of B_2O_3 did not cause decomposition of the $Al_{18}B_4O_{33}$ phase; rather, it possibly helped keep its thermodynamic stability. In other words, a certain amount of excess B_2O_3 was initially required against thermal decomposition. In the literature, unreacted Al_2O_3 was explained by a local high Al_2O_3 concentration particularly on particle surfaces due to evaporation of B_2O_3 or by out of equilibrium conditions given in the phase diagram or by the inconsistencies of the

exact stoichiometric Al_2O_3/B_2O_3 mole ratios for the aluminum borate compositions [2, 3, 4, 55]. Hernandez et al. [55] reported similar results (i.e., adding excess B_2O_3) such that the Al_2O_3 /A_9B_2/A_2B ratio was 58/42/0 for the 13.17 wt% B_2O_3, 0.4/99.2/0.4 for 20.5 wt% B_2O_3 and 0.7/97.4/1.9 for 26 wt% B_2O_3 mixtures after sintering at 1300°C. Moreover, the ratio was 0.3/99.5/0.2 for 26 wt% B_2O_3 after sintering at 1400°C, indicating that both excess B_2O_3 and high temperature were required to form almost-pure $Al_{18}B_4O_{33}$ phase. Furthermore, Al_2O_3 amount increased from 58% at 1300°C to 66.9% at 1400C for 13.17 wt% B_2O_3 and 0.4% at 1300°C to 6.3% at 1400°C for 20.5 wt% B_2O_3 compositions due to B_2O_3 evaporation, indicating that high enough excess B_2O_3 was initially required to keep thermodynamic stability of the A_9B_2 phase. Ray [4] reported that even though the powder mixture was prepared at the stoichiometric ratio of A_9B_2 (e.g., 13.17 wt% B_2O_3), other stoichiometric phase A_2B formed at 800°C (about 10%) as the intermediate step during phase formation. A_9B_2 phase formation, upon calcination in air without a closed-lid crucible, was completed at 1100°C with a trace amount of α-Al_2O_3 left. Hoffman et al. [3] characterized mullite-type $Al_{6-x}B_xO_9$ compounds in terms of powder diffraction and spectroscopic methods and also mentioned about the ambiguity of the chemical composition of Al borate phase, but $Al_{18}B_4O_{33}$ was preferred as the exact stoichiometric composition. A complete solid solution series for the $Al_{6-x}B_xO_9$ phases was reported between 13.17 wt% B_2O_3 (x=1.09 for A_9B_2) and 25.45 wt% B_2O_3 (x=2 for A_2B). Fisch et al. [2] synthesized Al borate powders in lid-covered platinum crucibles with adding excess B_2O_3. They mentioned that no indication of the predicted 9% B→Al substitution for the formation of stoichiometric Al borate known as $Al_{18}B_4O_{33}$ was found, using X-ray diffraction, FTIR and Raman spectroscopy. They reported that a low amount of Al vacancies at five-fold coordinated site were balanced by three-fold coordinated B-site and the main compound was determined as Al_5BO_9, rather than $Al_{18}B_4O_{33}$. Note that Al_5BO_9 (Card no: 01-080-2301) and $Al_{18}B_4O_{33}$ (Card no: 00-032-0003) phases have orthorhombic crystal structure with very close lattice parameters and unit cell volumes. Therefore, all peak positions and intensities almost completely match to each other, making the decision of the stable phase composition difficult to determine.

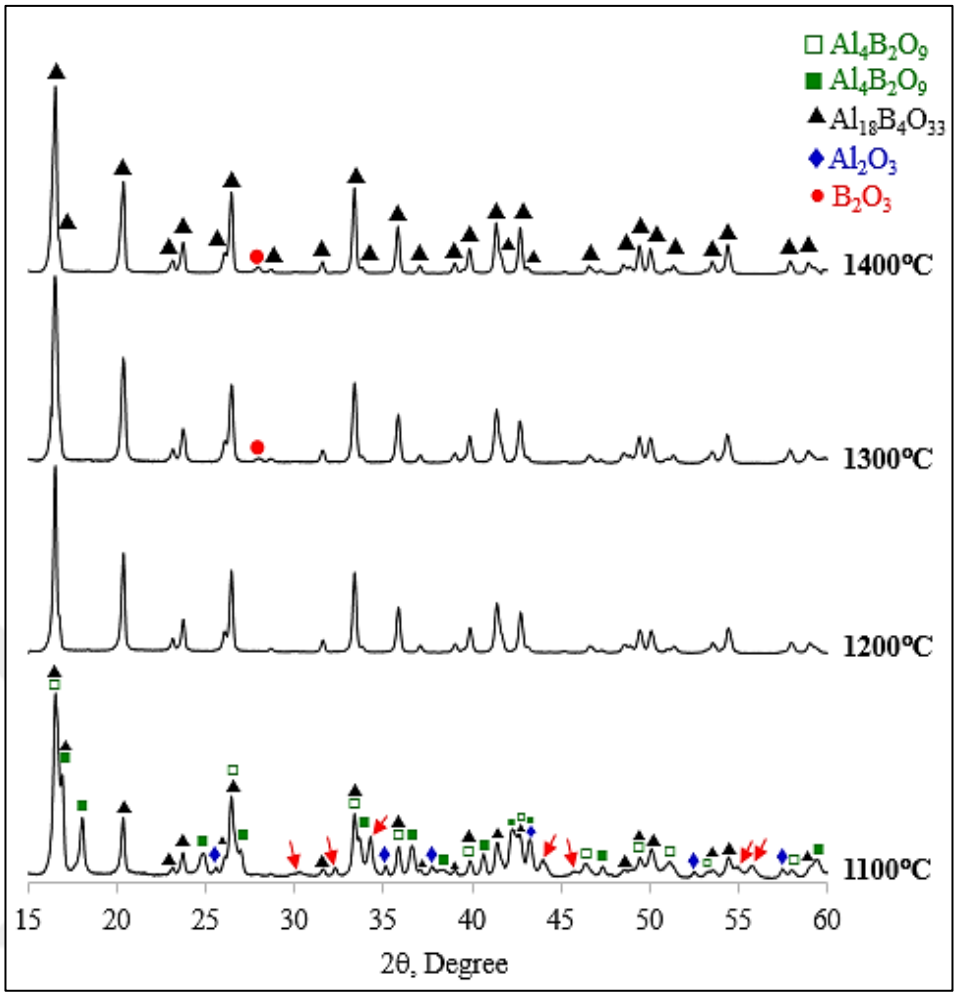

Figure 3.15 XRD patterns of the powders prepared at a mole ratio of 0.87 (44 wt% B_2O_3) and calcined at various temperatures

Figures 3.16 to 3.22 compare SEM pictures of the as-synthetized powders prepared at various molar ratios (see Table 2.2) and calcined at 1300ºC for 1h. Figure 3.13 shows that Al_2O_3 is the main phase up to 18.1 wt% B_2O_3 and Figures 3.16 to 3.18 indicate that particles are mostly rounded and it is difficult to distinguish Al_2O_3 and $Al_{18}B_4O_{33}$ phases. However, brighter particles may be Al_2O_3 because back scattered electron mode in SEM yields atomic number dependent imaging, that is, the higher the atomic number the brighter the particle. Few acicular particles less than about 1 μm rarely started forming with increasing B_2O_3 content such as for the 27.9 wt% B_2O_3 (Figure 3.19) and for the 34.4 wt% B_2O_3 (Figure 3.20) mixtures although the main phase was $Al_{18}B_4O_{33}$ as shown in Figure 3.13. In fact, these results indicate that $Al_{18}B_4O_{33}$ particles were not acicular in shape when first formed. Acicular $Al_{18}B_4O_{33}$ particles were fully obtained for the 44 wt% B_2O_3 (Figure 3.21) and the 54.1 wt% B_2O_3 (Figure

3.22) mixtures when Al_2O_3 was all consumed, or, alternatively, $Al_{18}B_4O_{33}$ phase was fully formed (Figure 3.13) in the resolution limit of the XRD analysis. When the particles are qualitatively considered from the acicular shape point of view, the particles are longer (~3-4 μm) and thicker even up to ~1 μm in the former whereas relatively shorter (~2-3 μm) and thinner (<~0.4 μm) but well-defined in the latter, which might be attributed to a higher nucleation rate of $Al_{18}B_4O_{33}$ particles within the B_2O_3-based melt.

Table 3.1 tabulates calculated stoichiometric elemental weight ratios in the Al borate compounds and the Al/O ratios are less than 1. Figures 3.21 and 3.22 also reveal some non-spherical and non-acicular particles or phases, which can be related to the presence of a B_2O_3-based liquid phase (see also Figures 3.9 and 3.10). Figure 3.21 reveals at high magnification that a nano network structure formed, which was attributed to the re-solidification of the vaporized B_2O_3 liquid phase during cooling down [63]. Therefore, SEM-EDS was used to analyze those particles for the 44 wt% B_2O_3 and 54.1 wt% B_2O_3 mixtures and the results are shown in Figures 3.23 and 3.24, respectively. Elemental weight ratios analyzed from the acicular and non-acicular particles indicate that some particles are rich in Al (numbers 5 and 8 in Figure 3.23; also deficient in B and O), rich in B (numbers 6 and 7 in Figure 3.23, numbers 1-5 in Figure 3.24; also deficient in Al and O) and relatively deficient in Al (numbers 8 and 9 in Figure 3.24). In fact, the B-rich particles are bigger, plate or layer-like and non-acicular in shape, the Al-deficient particles are blade-like in shape, and the Al-rich particles are non-acicular or acicular with square (or faceted) cross section, rather than the acicular particles with circular cross section (i.e., all analysis numbers other than the aforementioned ones). Note that EDS analysis is a qualitative technique to detect elements in the compounds and allows us to compare ratios with the stoichiometric ones. In addition, analysis of the light elements such as B, C, O is difficult due to their low photon energies or low yield X-rays (i.e., absorption of longer wavelength X-rays within the sample) and their K peaks occur in the energy range below 1 keV [64, 65]. For example, the analysis numbers 1, 2 and 3 (Figure 3.23) and analysis numbers 8 and 9 (Figure 3.24) are from the same particle but their elemental ratios are not the same. Therefore, the analysis results (and Al/O ratios) are somewhat different from the calculated results given in Table 3.1.

Table 3.1 Stoichiometric elemental ratios (wt%) in the aluminum borate compounds

Compound	Al	B	O	Al/O
$Al_{18}B_4O_{33}$	45.95	4.09	49.96	0.920
$Al_4B_2O_9$	39.45	7.90	52.64	0.750
Al_5BO_9	46.57	3.73	49.70	0.937
B_2O_3		31.06	68.94	

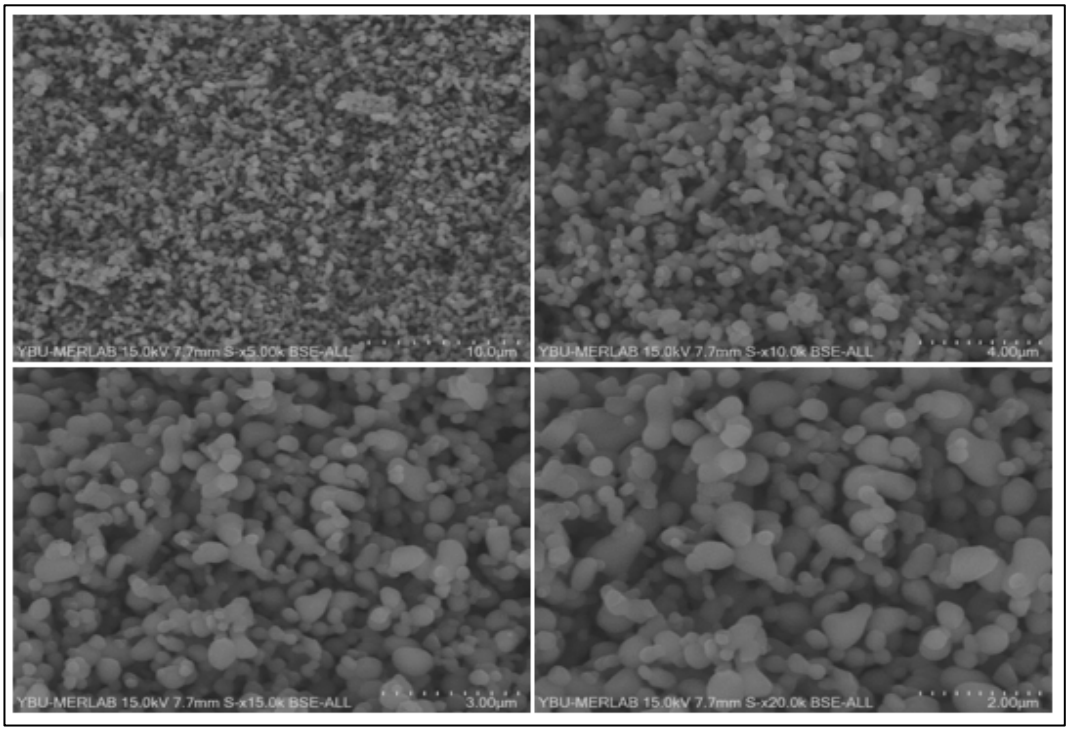

Figure 3.16 SEM pictures of the powder mixture prepared at a mole ratio of 5.73 (10.7 wt% B2O3) and calcined at 1300°C for 1h

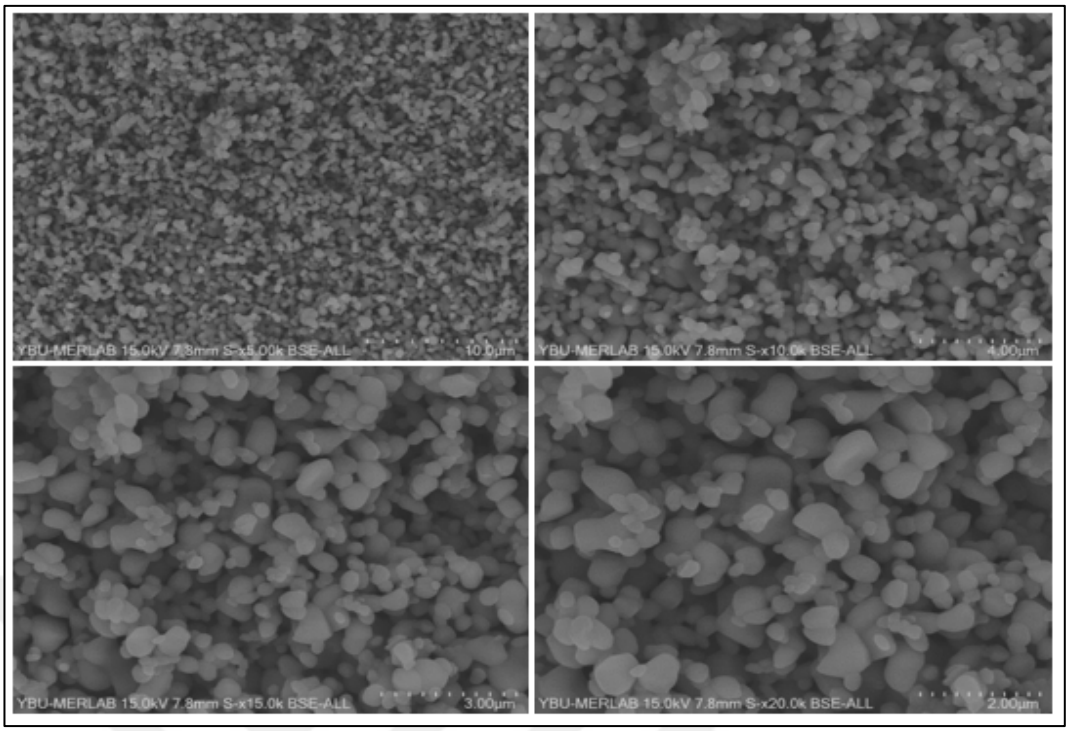

Figure 3.17 SEM pictures of the mixture prepared at a mole ratio of 4.41 (13.4 wt% B_2O_3) and calcined at 1300ºC for 1h

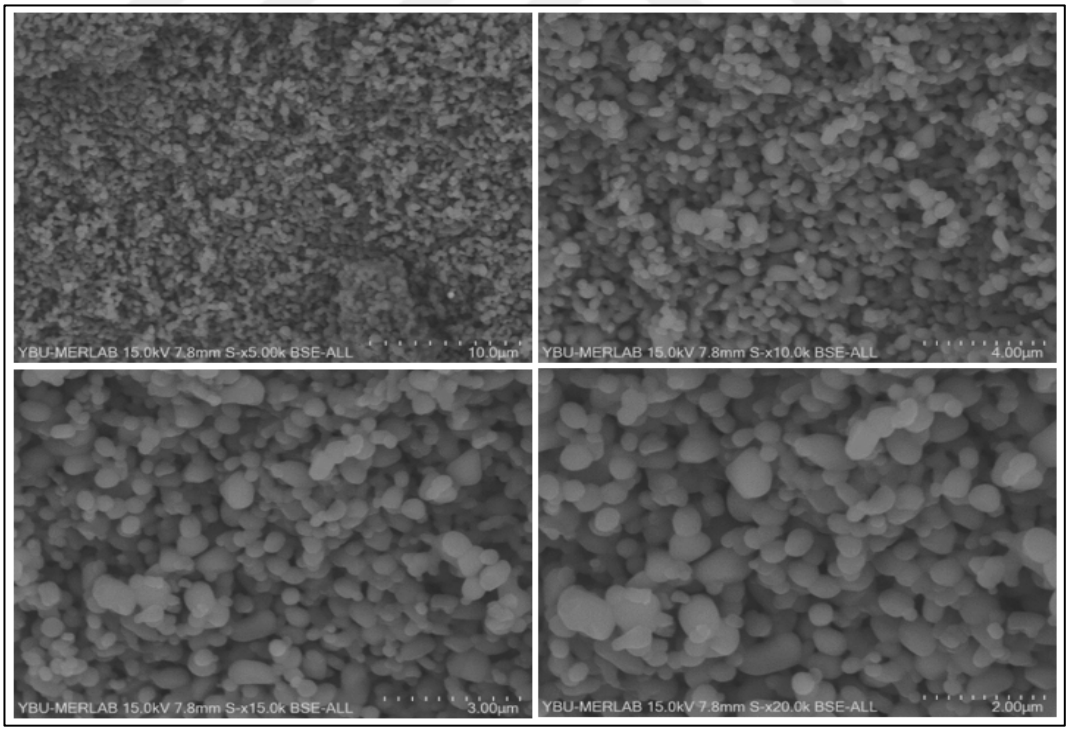

Figure 3.18 SEM pictures of the mixture prepared at a mole ratio of 3.09 (18.1 wt% B_2O_3) and calcined at 1300ºC for 1h

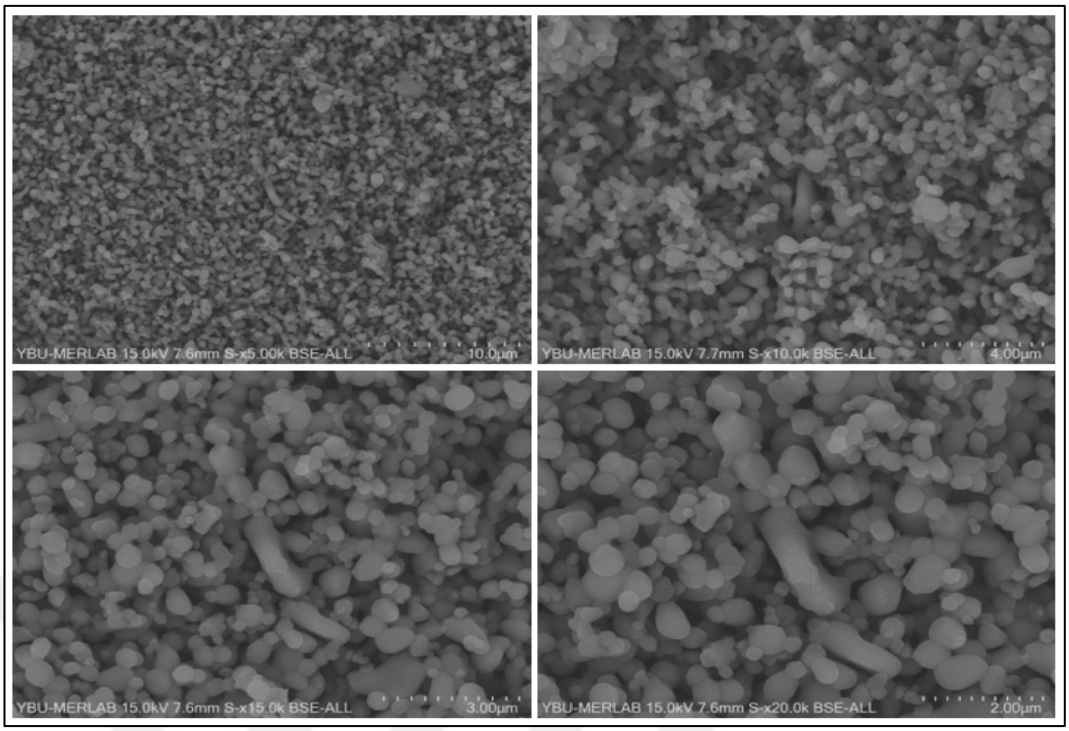

Figure 3.19 SEM pictures of the mixture prepared at a mole ratio of 1.77 (27.9 wt% B_2O_3) and calcined at 1300ºC for 1h

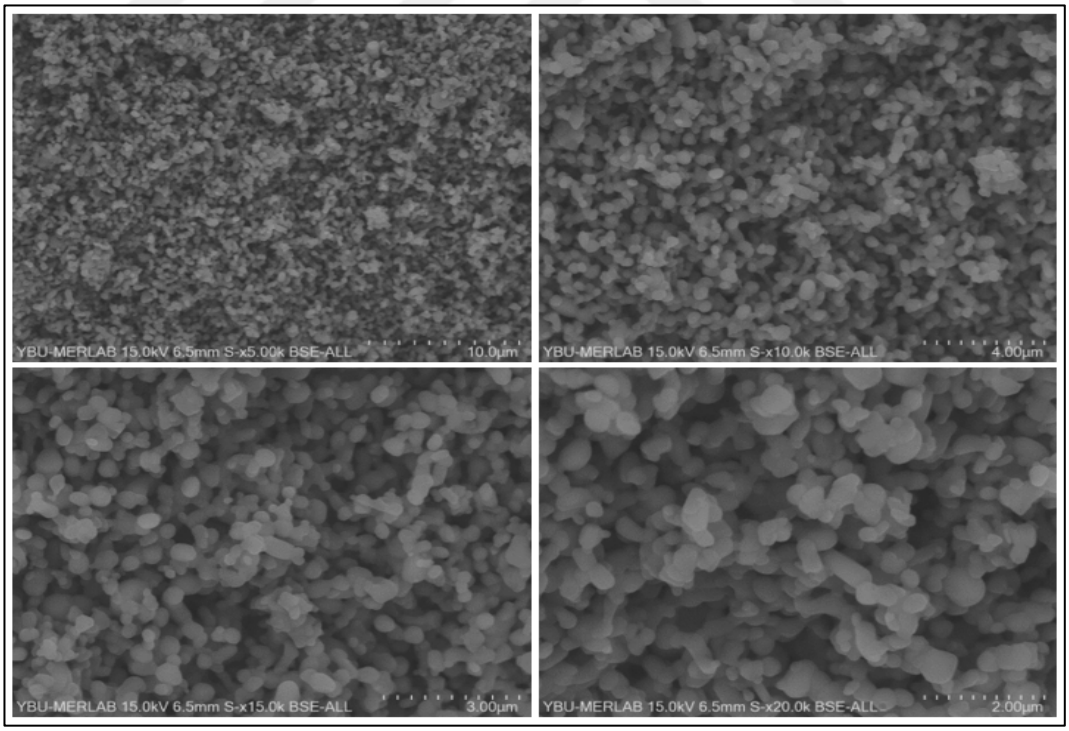

Figure 3.20 SEM pictures of the mixture prepared at a mole ratio of 1.3 (34.4 wt% B_2O_3) and calcined at 1300C for 1h

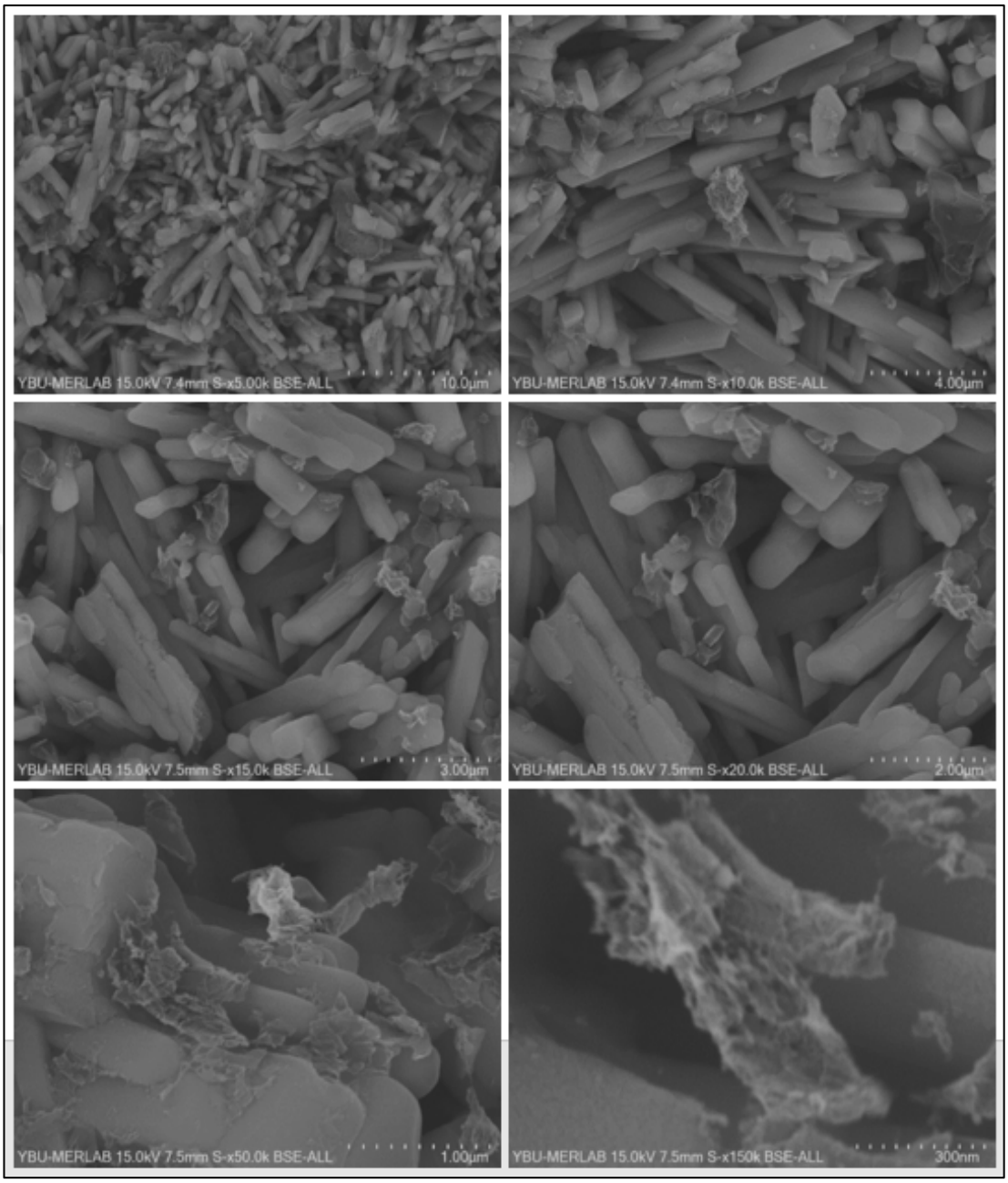

Figure 3.21 SEM pictures of the mixture prepared at a mole ratio of 0.87 (44 wt% B_2O_3) and calcined at 1300ºC for 1h

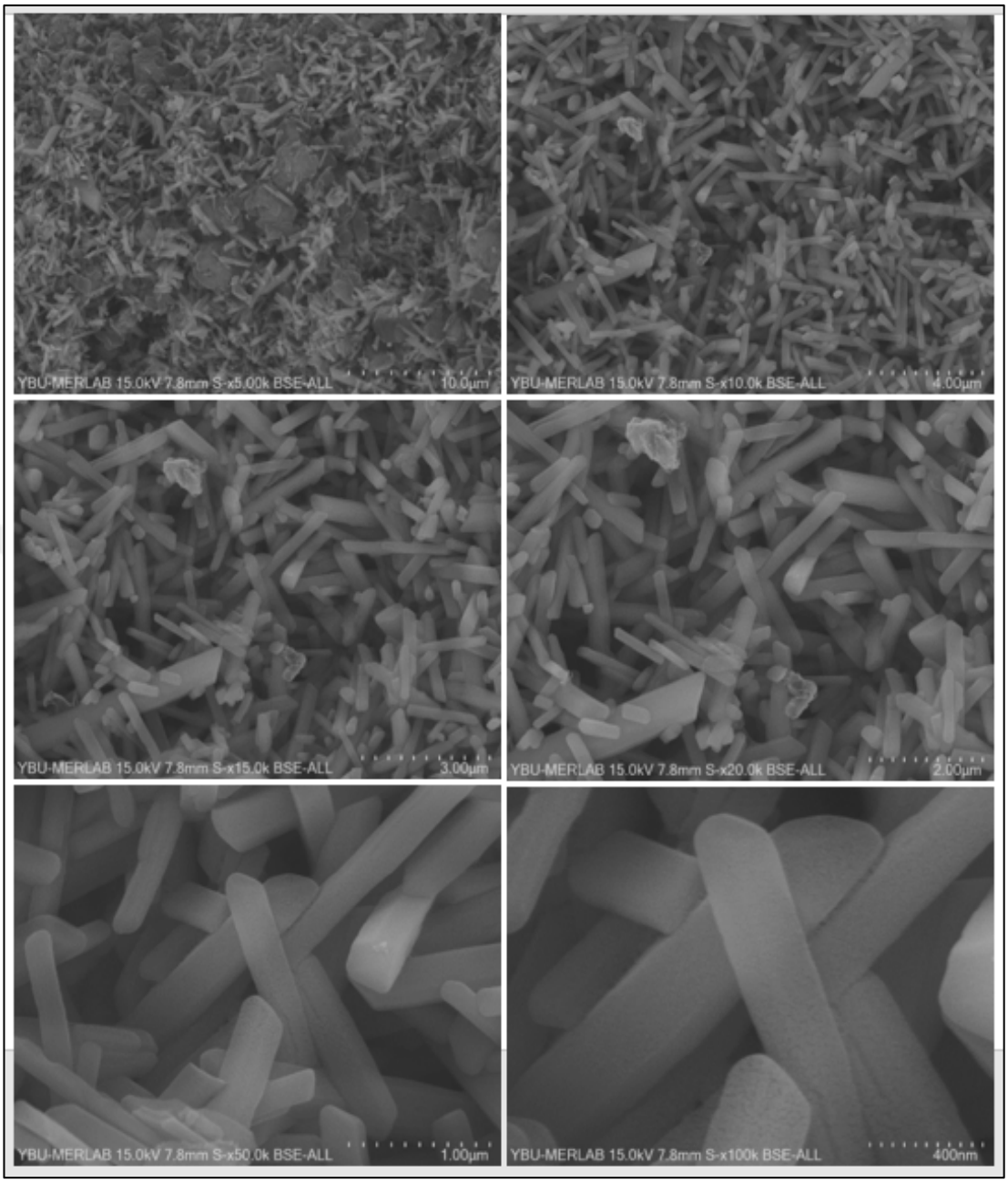

Figure 3.22 SEM pictures of the mixture prepared at a mole ratio of 0.58 (54.1 wt% B_2O_3) and calcined at 1300ºC for 1h

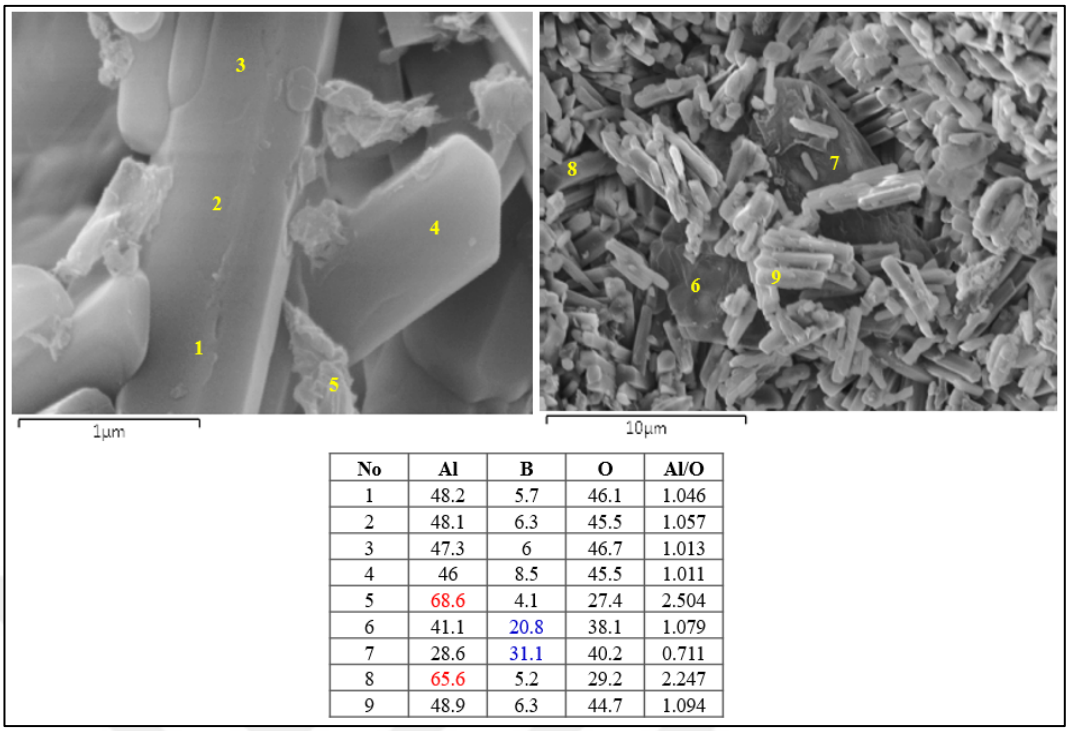

No	Al	B	O	Al/O
1	48.2	5.7	46.1	1.046
2	48.1	6.3	45.5	1.057
3	47.3	6	46.7	1.013
4	46	8.5	45.5	1.011
5	68.6	4.1	27.4	2.504
6	41.1	20.8	38.1	1.079
7	28.6	31.1	40.2	0.711
8	65.6	5.2	29.2	2.247
9	48.9	6.3	44.7	1.094

Figure 3.23 SEM-EDS analysis of the mixture prepared at a mole ratio of 0.87 (44 wt% B_2O_3) and calcined at 1300ºC for 1h

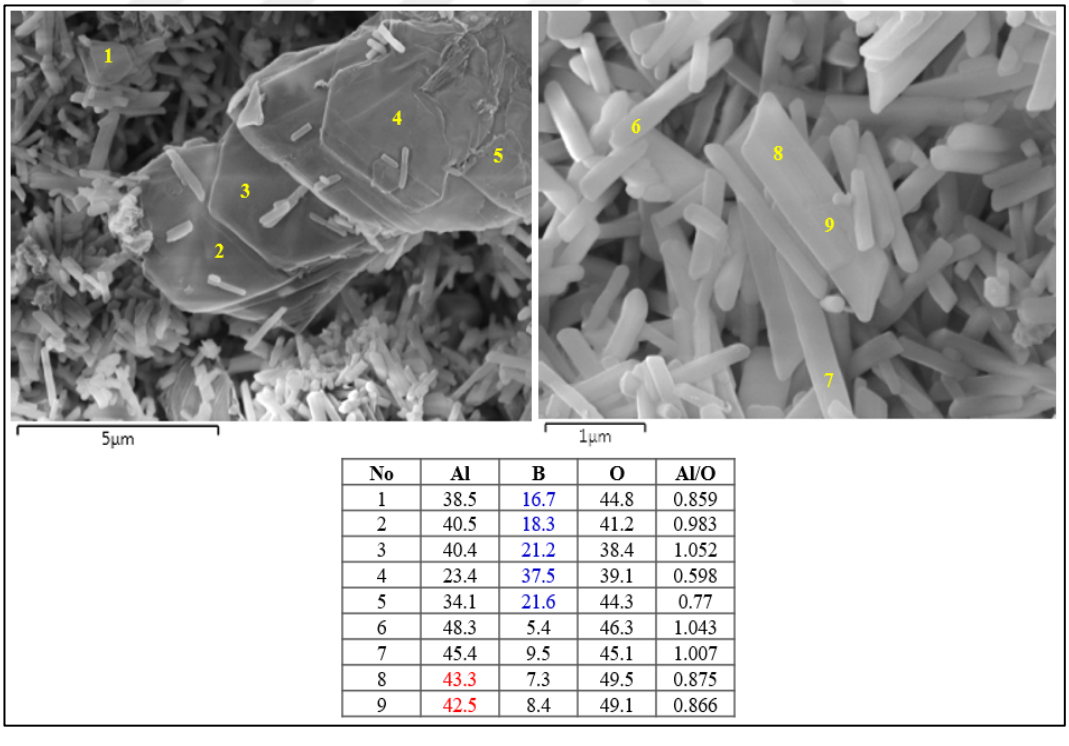

No	Al	B	O	Al/O
1	38.5	16.7	44.8	0.859
2	40.5	18.3	41.2	0.983
3	40.4	21.2	38.4	1.052
4	23.4	37.5	39.1	0.598
5	34.1	21.6	44.3	0.77
6	48.3	5.4	46.3	1.043
7	45.4	9.5	45.1	1.007
8	43.3	7.3	49.5	0.875
9	42.5	8.4	49.1	0.866

Figure 3.24 SEM-EDS pictures of the mixture prepared at a mole ratio of 0.58 (54.1 wt% B_2O_3) and calcined at 1300ºC for 1h

Figure 3.25 compares the SEM pictures of the powders synthetized from the mixture prepared at a mole ratio of 0.87 (44 wt% B_2O_3) and calcined at various temperatures from 1100°C to 1400°C for 1 h. Figure 3.25(a) indicates that particles formed at various shapes and sizes when calcined at 1100°C and it is very difficult to identify phases formed. In fact, the XRD analysis in Figure 3.13 revealed partial formation of $Al_{18}B_4O_{33}$ and some other phases such as unreacted Al_2O_3, intermediate $Al_4B_2O_9$ phases together with some unknown peaks. Figure 3.13 also shows that $Al_{18}B_4O_{33}$ formation was completed at T≥1200°C but Figure 3.25(b) shows that particles are mostly acicular in shape but some non-acicular and a few layer-like particles are also present when calcined at 1200°C. $Al_{18}B_4O_{33}$ particles are not acicular in shape when first formed as explained for Figures 3.19 and 3.20. Although Figure 3.13 does not indicate the presence of the B_2O_3-rich phase in the resolution limit of the XRD analysis, the layer-like particles (shown by arrows) in Figure 3.25(b) are similar to the ones oberved in Figure 3.24. In addition, boron cannot be detected accurately from X-ray powder diffraction data due to its low scattering factor [3]. Therefore, $Al_{18}B_4O_{33}$ particles are mostly acicular and some of them are non-acicular in shape. Figure 3.25(c) and 3.25(d) present the SEM pictures of the powders calcined at 1300°C and 1400°C, respectively. In both powders, $Al_{18}B_4O_{33}$ particles are acicular and some B_2O_3-rich phase is also present as shown by arrows. When the SEM pictures for the powders calcined at 1200°C, 1300°C and 1400°C are compared, both the amount of the B_2O_3-based liquid phase (also shown in Figure 3.15) and thickness of the acicular particles increase with increasing calcination temperature. Higher evaporation rate particularly at 1400°C (weight loss of 6.51%) may promote or facilitate the formation of the B_2O_3-rich phase and increase the growth rate of the acicular particles in thickness direction. A calcination temperature of 1300°C for 1 h yields the optimum temperature to synthetize almost full acicularly shaped $Al_{18}B_4O_{33}$ particles together with minimum amount B_2O_3-based phase in this study.

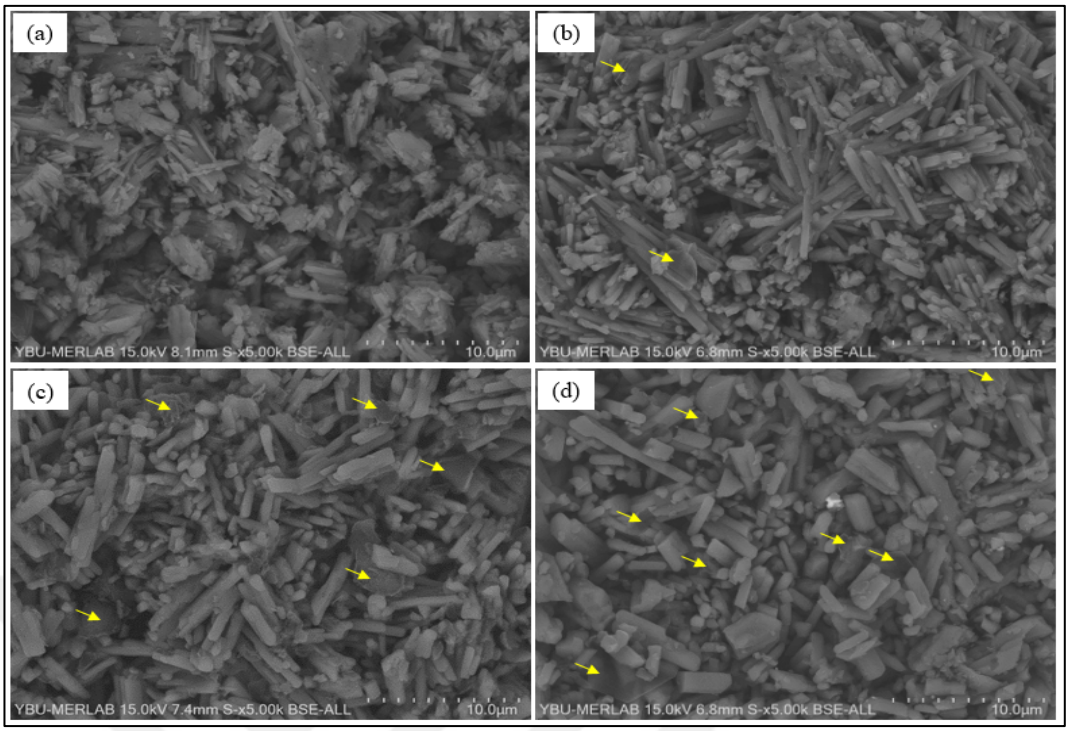

Figure 3.25 SEM pictures of the powders synthetized from the mixture prepared at a mole ratio of 0.87 (44 wt% B_2O_3) at various calcination temperatures; (a) 1100ºC, (b) 1200ºC, (c) 1300ºC and (d) 1400ºC for 1 h

Figure 3.14 also indicates some broad thermal signals between 700ºC and 1100°C, which can be associated with the formation of the Al borate phases (i.e., $Al_4B_2O_9$ and/or $Al_{18}B_4O_{33}$). Hernández et al [55] also observed similar signals for the compositions with 13.0, 20.5 and 26.0 wt% B_2O_3 between 650ºC and 900ºC. They also reported for the 26.0 wt% B_2O_3 composition that Al_2O_3, $Al_4B_2O_9$ and $Al_{18}B_4O_{33}$ were all present between 800ºC and 1000°C, and both some unreacted Al_2O_3 and $Al_{18}B_4O_{33}$ were present between 1100ºC and 1200°C. $Al_{18}B_4O_{33}$ was the only phase at T≥1300ºC. It is also evident from Figure 3.15 that two borate phases coexisted at 1100ºC and $Al_{18}B_4O_{33}$ formation was complete at temperatures ≥1200ºC. In fact, this phase transformation may correspond to a weak endothermic peak observed at 1172°C given in Figure 3.14. Hernandez et al. [55] proposed a mechanism for a mixture of Al_2O_3 and 26 wt% B_2O_3 that Al_2O_3 first dissolved in boron oxide melt, and then crystallization of the borate phases (i.e., intermediate $Al_4B_2O_9$ and $Al_{18}B_4O_{33}$) took place in whisker morphology. The viscosity of the boron-based melt affected the formation of the intermediate borate phase and its viscosity decreased with increasing temperature facilitating dissolution and crystallization of the borates during thermal treatment.

Hoffmann et al. [3] also mentioned about crystallization process in the phase field A_2B-$Al_{18}B_4O_{33}$ such that phase formation studies by high temperature XRD and DSC indicated exothermic signals at 890°C for the 13.17 wt% B_2O_3 and 830°C for the 30 wt% B_2O_3 composition. In other words, higher B_2O_3 content reduced the glass phase viscosity, resulting in enhanced atomic diffusion as well as lower crystallization temperature. Another DTA signal was observed above about 1000°C, belonging to a probable phase transformation of $Al_{6-x}B_xO_9$ into $Al_{18}B_4O_{33}$. However, a signal above 1000°C was not observed for the exact initial composition of $Al_{18}B_4O_{33}$ (13.17 wt% B_2O_3). Therefore, a weak endothermic peak observed at 1172°C in Figure 3.14 could be assigned to a phase formation from $Al_4B_2O_9$ to $Al_{18}B_4O_{33}$, although it is higher than the incongruent melting temperature of $Al_4B_2O_9$ at 1035°C (see Figure 3.4). Similarly, Hernandez et al. [55] also synthetized $Al_{18}B_4O_{33}$ with a phase ratio of 99.2% at 1300°C for the 20.5 wt% B_2O_3 and with a phase ratio of 99.5% for the 26 wt% B_2O_3 at 1400°C.

Temperature and amount of initial B_2O_3 alter the viscosity of the B_2O_3-based liquid such that higher B_2O_3 content and temperature reduce the glass phase viscosity affecting the crystallization and growth processes [3, 55]. In our study, full $Al_{18}B_4O_{33}$ formation was obtained at 44 wt% B_2O_3 (e.g., rather than the stoichiometric ratio of 13.17 wt% B_2O_3), which may be attributed to some factors such as; i) existence of initially present absorbed water (or, existence of boric acid) that first requires boric acid decomposition to B_2O_3, subsequent B_2O_3 melting and dissolution rate of Al_2O_3 in the melt, ii) change in the melt viscosity as a function of excess B_2O_3 and temperature, iii) evaporation rate of $B_2O_3$with increasing calcination temperature particularly from open-lid crucible, which changes the kinetics of crystallization from standpoint of the solute (Al_2O_3 and/or other Al borate compounds at different Al_2O_3/ B_2O_3 mole ratios) saturation in the melt and subsequent phase transformation. Our results suggest that 44 wt% B_2O_3 (e.g., Al_2O_3/B_2O_3 mole ration of 0.87) is required to obtain a melt that has a high enough solute saturation to induce nucleation or crystallization of $Al_{18}B_4O_{33}$ phase as well as low enough viscosity to enhance diffusion rate in order to grow acicular particles at calcination temperatures ≥1200°C for 1h (or, with full acicular particle formation at 1300°C). In brief, synthesis of mullite-type Al borate compounds is highly processing-sensitive because small differences in mole ratio, humidity in the

starting powder (boric acid formation), synthesis conditions (open or lid-covered crucibles), reaction temperature and evaporation rate strongly influence the phases formed, phase formation sequence and resulting thermodynamically stable products.

3.2 Sintering and Densification

$Al_{18}B_4O_{33}$ powder prepared at 44 wt% B_2O_3 (e.g., Al_2O_3/B_2O_3 mole ratio of 0.87) and calcined at 1300ºC for 1h was used for sintering experiments. Gel casting (e.g., colloidal processing) was preferred to improve powder compaction and enhance densification as well as to fabricate Al borate ceramics in complex shapes for specific applications. Sintering is very difficult for Al borate ceramics without sintering additive since sintered Al borate ceramics have naturally porous microstructure due to needle shaped powders/grains [4,55,56]. In this study, four different compositions were decided to compare densification behaviors and physical properties. For the PAB composition, only $Al_{18}B_4O_{33}$ powders without any additive were used. For the AB composition, $Al_{18}B_4O_{33}$ powder with 2 wt% CaO was used because addition of CaO was reported to enhance sintering of $Al_{18}B_4O_{33}$ ceramics successfully [4]. For the AMG composite (35 wt% $Al_{18}B_4O_{33}$ + 35 wt% Mullite + 30 wt% Glass), glass which melts at low temperature (<900°C [59]) and mullite was used. Mullite was selected due to having similar crystal structure and lattice parameters with $Al_{18}B_4O_{33}$. Mullite powder had a d_{50}=0.34 μm and d_{90}=1.21 μm after ball milling (Figure 3.26) [66], which indicates that d_{50}=3-5 μm of the initial mullite powder (see Table 2.3) was successfully decreased for colloidal gel casting method. For the ABG composite (70 wt% $Al_{18}B_4O_{33}$ + 30 wt% glass), glass was selected as a sintering aid, as for the AMG sample. The particle size distribution of glass after ball milling is given in Figure 3.27. The particle size of glass was measured as d_{10}=1.16 μm, d_{50}=2.12 μm, d_{90}=3.91 μm and mode value was measured as 1.99 μm [59].

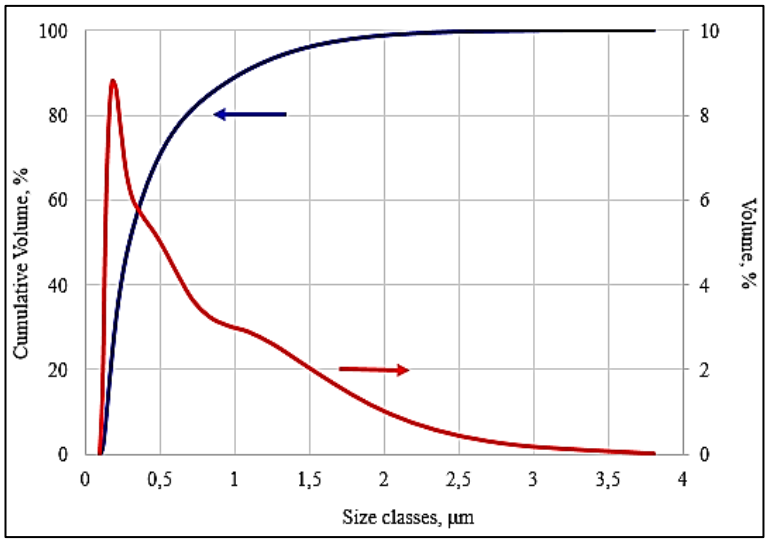

Figure 3.26 Particle size distribution of mullite [66]

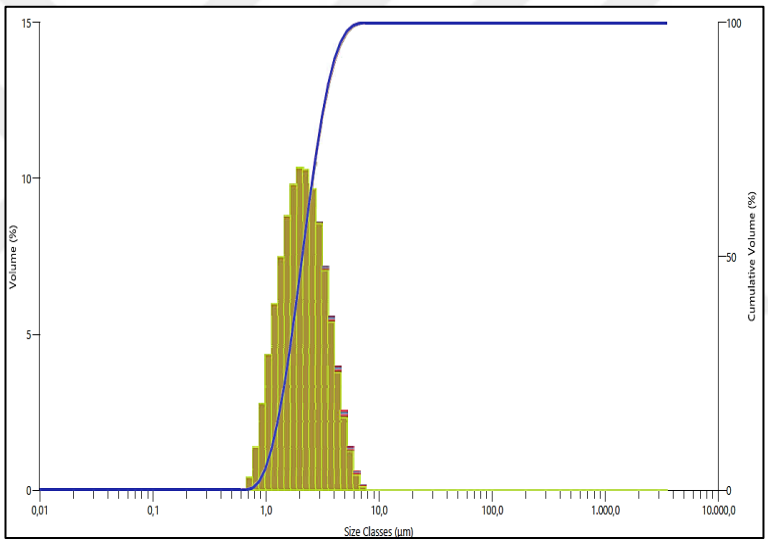

Figure 3.27 Particle size distribution of glass [59]

Gel casting method allows to fabricate ceramics having complex shape with high green strength in a short time. After preparing the gel cast slurries, slurries were casted into the aluminum foil molds and cured with heat (3 min. at 25ºC, 3-20 min at 40ºC, 1h at 70ºC). No cracking or breakage was observed on the samples after controlled drying and following burn out processes. The samples after burnout are shown in Figure 3.28. The main advantage of the gel casting method is the ability to obtain ceramics with high packing homogeneity due to cross linking of monomers [42]. In this regard, samples with high green density and high strength are produced by gel casting process. The samples after burnout were even easily dry-polished to flat the parallel surfaces.

While the AMG and AB samples were sintered at a heating rate of 5°C/min in air at 1300°C, 1350°C and 1400°C for 1 h, the ABG and PAB samples were sintered at a heating rate of 5°C/min in air at only 1350°C for 1 h.

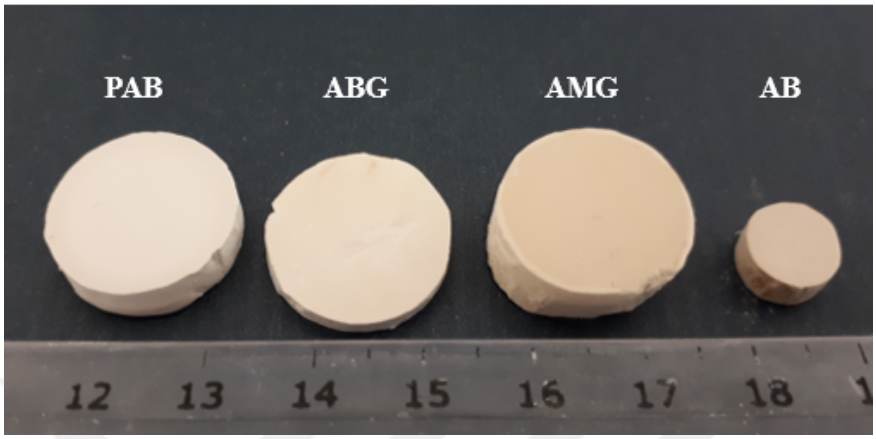

Figure 3.28 Samples after burn out process

Phase analysis was carried out both from as-sintered ceramic surfaces to evaluate surface composition due to possible B_2O_3 evaporation as well as from polished ceramic surfaces to evaluate bulk composition. Figure 3.29 shows the XRD patterns of the AB samples as a function of sintering temperature. All main peaks belonged to Al_2O_3 (JCPDS #10-0173) and dominated the $Al_{18}B_4O_{33}$ peaks at all temperatures when the XRD patterns were taken from the as-sintered ceramic surfaces. However, the $Al_{18}B_4O_{33}$ peaks were almost the only peaks when the surface was polished, revealing that B_2O_3 evaporation was very severe from the surfaces causing decomposition of the $Al_{18}B_4O_{33}$ phase into Al_2O_3. Figure 3.30 shows the XRD patterns of the AMG samples as a function of sintering temperature. There appeared a shallow hump between 2θ~15-35° due to the presence of an amorphous glass phase. In addition, Al_2O_3 phase did not form when XRD was taken from the as-sintered and polished surfaces. However, anorthite ($(Ca,Na)(Si,Al)_4O_8$, JCPDS #00-041-1481) crystallization from the glass was observed, similar to the one observed in the Al_2O_3/glass composite [59]. It was straightforward to index the peaks at 1300°C, although $Al_{18}B_4O_{33}$ (JCPDS #32-0003) and mullite (JCPDS #15-0776) had very close peak positions due to similar crystal structures and lattice parameters [8, 9]. In other words, most $Al_{18}B_4O_{33}$ peaks were like shoulders to the mullite peaks, and all peaks broadened with increasing temperature. It is important to note that a characteristic $Al_{18}B_4O_{33}$ peak at 2θ=20.32°

at 1300°C disappeared with increasing temperature, stating a possible solid solution formation. A solid solution between 3:2 mullite and $Al_{18}B_4O_{33}$ was proposed due to the close similarities between the physical properties of mullite and $Al_{18}B_4O_{33}$ [67, 68]. The mineral boralsilite ($Al_{16}B_6Si_2O_{37}$) belongs to the mullite-type family of crystal structures in the ternary Al_2O_3-B_2O_3-SiO_2 system [69, 70]. Griesser et al [71] reported that mullite incorporates large amounts of B_2O_3 into its structure depending on the bulk composition of the starting materials. B_2O_3 was substituted for SiO_2 in the sol–gel-derived 3:2 and 2:1 mullite compositions and then calcined at 950°C and 1300°C. Up to 20 mole% B_2O_3 incorporation in the 3:2 mullite (e.g., 60 mole% Al_2O_3+20 mole% SiO_2+20 mole% B_2O_3) and 15 mole% incorporation in the 2:1 mullite (e.g., 70 mole% Al_2O_3+15 mole% SiO_2+15 mole% B_2O_3) resulted in mullite structure at both calcination temperatures. Boron was incorporated into the mullite structure in planar three-fold coordination. Lührs et al [72] also studied B_2O_3 addition into sol-gel derived 3:2 mullite, based on the 1:1 substitution of Si by B. A boron-mullite below 10 mole% B_2O_3 formed, boron-mullite together with different Al_2O_3 phases were present between 10 and 18 mole % B_2O_3, and $Al_{18}B_4O_{33}$ and Al_2O_3 formed above 23 mole% B_2O_3 after calcination at 1200°C for 5h. Long heat treatment at 1400°C for 90h leaded to the decomposition of boron-mullite to boron-free mullite and the formation of α-Al_2O_3. The presence of boron in threefold rather than in fourfold coordination was verified by FTIR spectroscopy. Therefore, the phase formed at 1350°C and 1400°C was named as a solid solution between mullite and $Al_{18}B_4O_{33}$. Furthermore, when the XRD pattern taken from the polished surface was considered, the characteristic $Al_{18}B_4O_{33}$ peak at 2θ=20.32° was very strong in intensity together with sharp mullite and $Al_{18}B_4O_{33}$ main peaks. This result proves that mullite dissolved more in the glass phase and then precipitated on the $Al_{18}B_4O_{33}$ particles (i.e., epitaxial nucleation of mullite on $Al_{18}B_4O_{33}$ particles, also observed in literature [73, 74-76] with the formation of a solid solution at the interface. Limited solid solution could be attributed to a short sintering time of 1h.

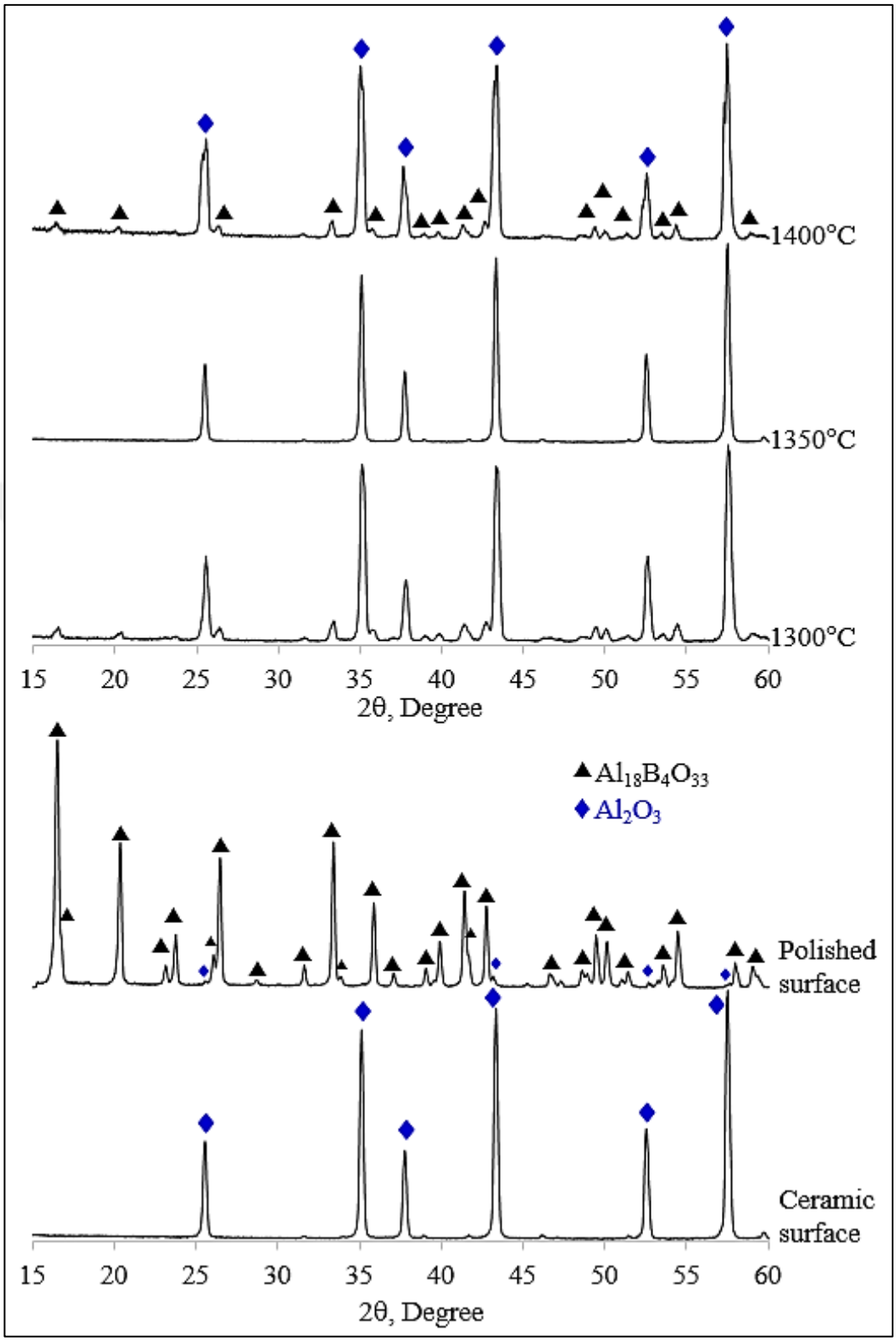

Figure 3.29 XRD patterns of the AB samples; (top) XRD patterns taken from the as-sintered ceramic surfaces as a function of sintering temperature, (bottom) comparison of the XRD patterns taken from the as-sintered and polished surfaces of the ceramic sintered at 1350°C.

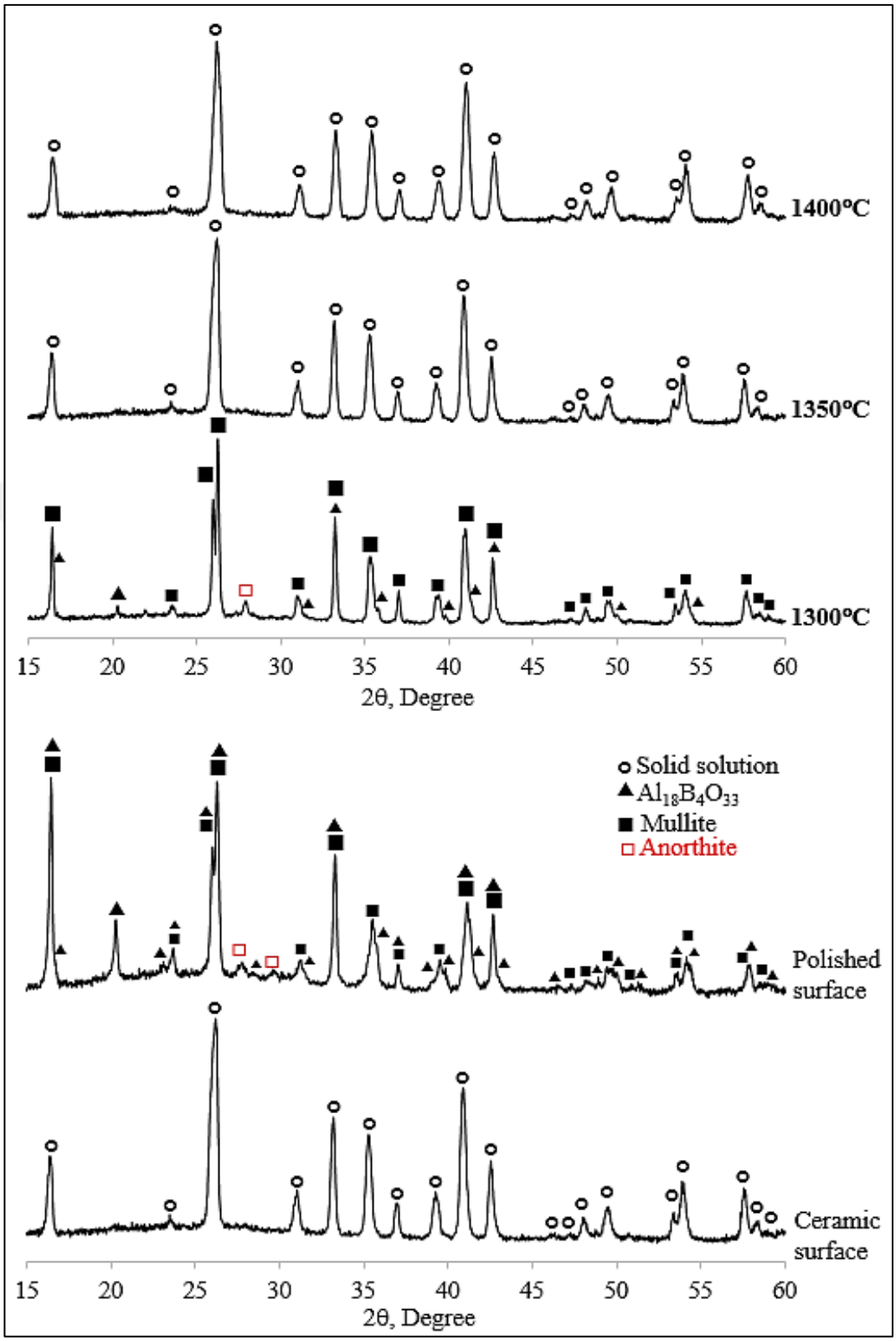

Figure 3.30 XRD patterns of the AMG samples; (top) XRD patterns taken from the as-sintered ceramic surfaces as a function of sintering temperature, (bottom) comparison of the XRD patterns taken from the as-sintered and polished surfaces of the ceramic sintered at 1350°C.

The XRD patterns of the ABG sample sintered at 1350°C for 1h is given in Figure 3.31. There appeared a shallow hump between 2θ~15-35° due to the presence of an amorphous glass phase in both surface and polished XRD patterns. All peaks belonged to $Al_{18}B_4O_{33}$ phase together with weak peaks of anorthite crystallized from the glass. Figure 3.32 shows the XRD pattern of the PAB sample sintered at 1350°C for 1h. The main peaks belonged to $Al_{18}B_4O_{33}$ in both surface and polished XRD patterns but other minor phases such as Al_2O_3, an unknown and B_2O_3-based liquid phases were also present. The peak intensities of the Al_2O_3 and unknown phases were relatively higher in the surface XRD pattern due to B_2O_3 evaporation.

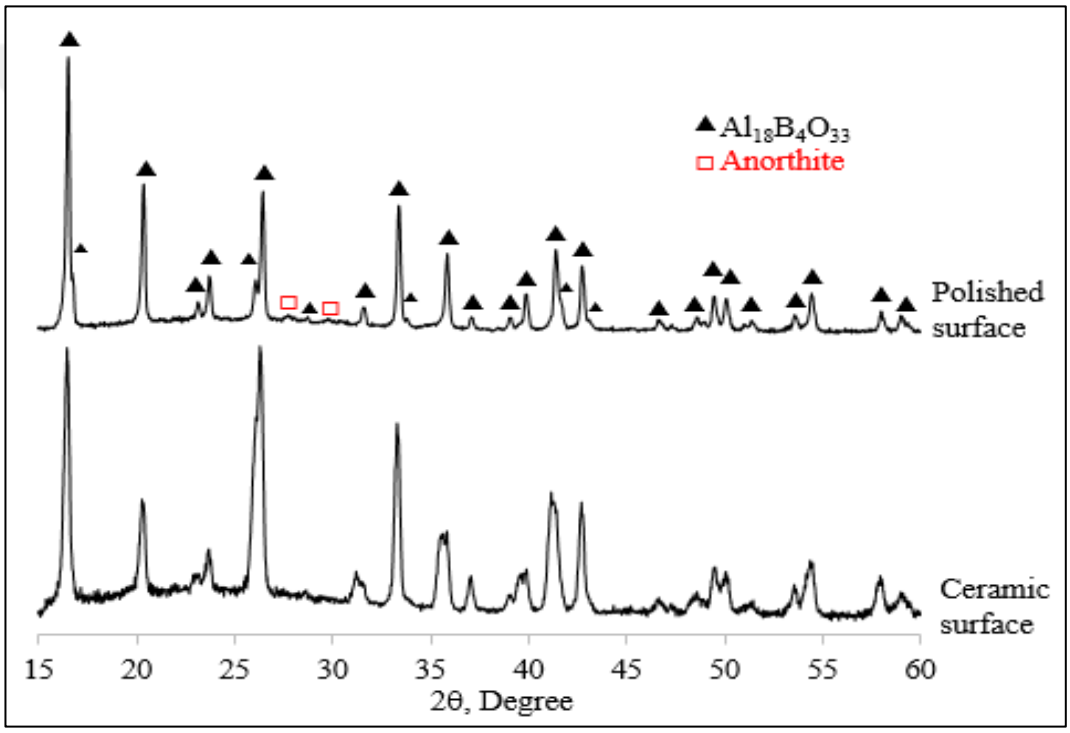

Figure 3.31 XRD patterns of the ABG sample sintered at 1350°C for 1h

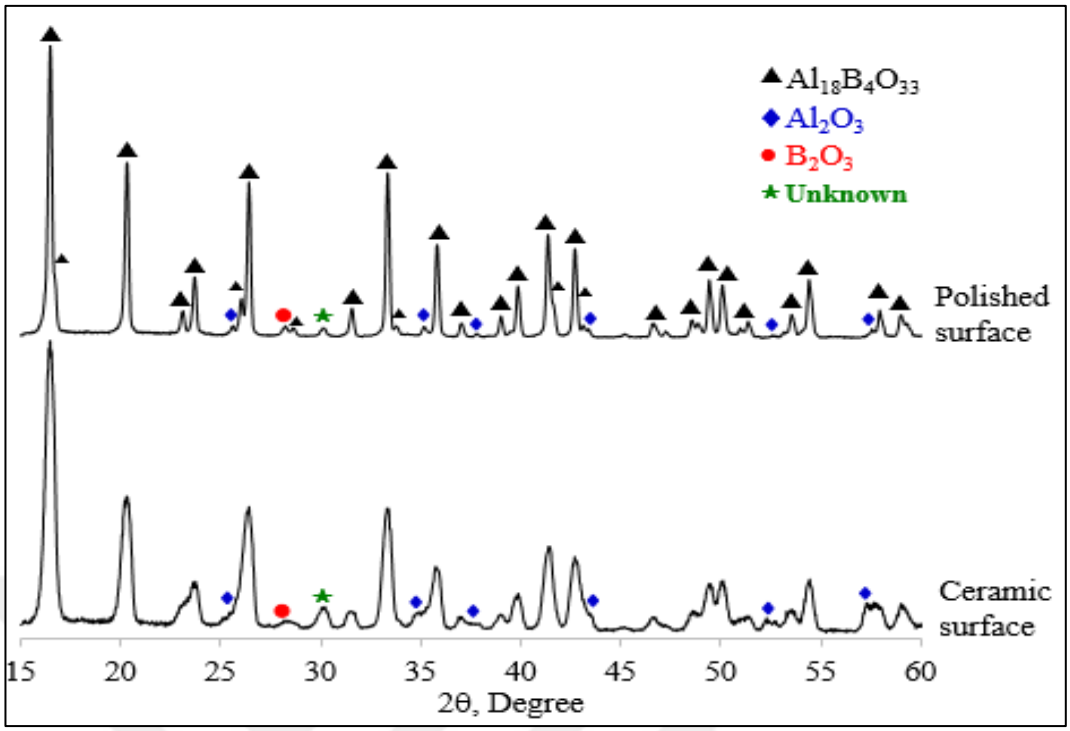

Figure 3.32 XRD patterns of the PAB sample sintered at 1350°C for 1h

Figure 3.33 compiles and compares the as-sintered and polished surface XRD patterns of the ceramics sintered at 1350°C for 1h. B_2O_3 evaporation mainly takes place from the free surfaces and it is highly possible to have a slight compositional gradient between surface and inner volume. Bulk densities of the sintered ceramics were determined by Archimedes' method. Serial, parallel and logarithmic models [77, 78] were used to calculate respective theoretical densities of the AMG and ABG composites as shown below;

Parallel modelling, $d = d_A.V_A + d_M.V_M + d_G.V_G$ **(3.4)**

Serial modelling; $1/d = V_A/d_A + V_M/d_M + V_G/d_G$ **(3.5)**

Logarithmic modelling; $\log d = V_A.\log d_A + V_M.\log d_M + V_G.\log d_G$ **(3.6)**

Where d is calculated density (g/cm^3), d_i is the theoretical densities of the phases comprising of the composite structure (e.g., A: $Al_{18}B_4O_{33}$, M: mullite and G: glass), V_i is the volume ratios of each phase. The calculated density values were based on the relative proportions of the starting amounts. The logarithmic model is between the serial and parallel models and it is generally used as a calculated theoretical density.

Therefore, theoretical density was considered as 2.8 gr/cm^3 and 2.75 gr/cm^3 for the AMG and ABG composites, respectively. The anorthite phase was very low in intensity and hence neglected at calculations. Theoretical density of $Al_{18}B_4O_{33}$ (e.g., 2.93 gr/cm^3 [4]) was considered for the AB and PAB ceramics, neglecting minor Al_2O_3 and/or unknown phases.

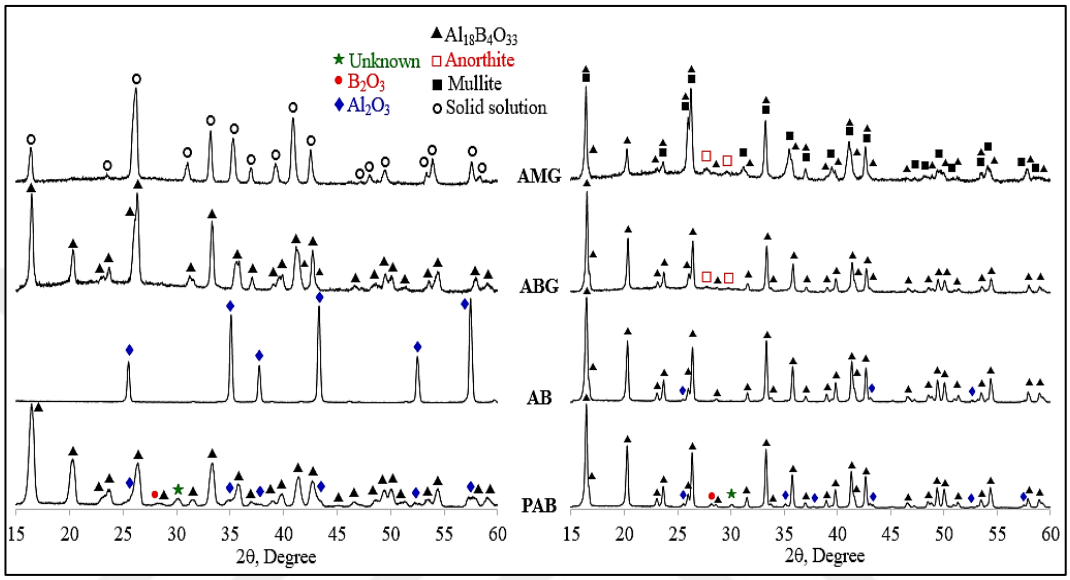

Figure 3.33 Comparison of the XRD patterns of the ceramics sintered at 1350ºC for 1 h; (left) XRD patterns taken from the as-sintered ceramic surfaces, (right) XRD patterns taken from the polished ceramic surfaces

Table 3.2 summarizes sintering and densification parameters for the sintered samples. The highest densification was achieved at 1350ºC for the AB (95.4% relative density) and AMG (94.8% relative density) samples. In fact, de-densification started at 1400ºC for both compositions. At 1350ºC, the ABG sample had a relative density 89.4% and the PAB sample had a relative density of 59.7%. Note that the apparent (or open) porosity is different from the true porosity (i.e., it is equal to 100-relative density) in that the former includes the volume of the open pores only but the latter includes the volume of both the closed and open pores. Furthermore, apparent porosity should be less than the true porosity. The true porosity is 40.3%, which is less than the apparent porosity of 44.3% for the PAB sample. This inconsistency stems from an error tolerance due to wiping of water-saturated ceramic surfaces with a moist cloth in the Archimedes' method, particularly in highly porous materials. Weight losses were

relatively low for the glass-containing AMG and ABG compositions but it was very high for the PAB composition.

Table 3.2 Sintering and densification parameters for the sintered samples

Nomenclature	Sintering conditions	Weight loss, %	Bulk density, g/cm^3	Relative density, %	Open porosity, %	Water absorption, %
AB	1300°C-1h	2.80	2.76	94.2	0.86	0.313
	1350°C-1h	4.16	2.80	95.4	2.86	1.021
	1400°C-1h	3.63	2.77	94.5	1.84	0.664
AMG	1300°C-1h	1.66	2.61	93.2	0.25	0.096
	1350°C-1h	1.13	2.65	94.8	0.04	0.016
	1400°C-1h	1.63	2.63	94.0	0.007	0.003
ABG	1350°C-1h	1.67	2.46	89.4	5.77	2.35
PAB	1350°C-1h	25.08	1.75	59.7	44.3	25.38

Figure 3.34 compares the fracture-surface SEM pictures of the PAB, AB, ABG and AMG ceramics sintered at 1350°C for 1h. Figure 3.34(a) shows the microstructure of the PAB ceramic. Solid state sintering of the acicular shape $Al_{18}B_4O_{33}$ particles resulted in partial densification due to inhomogeneous (or, irregular) particle packing in the green state, which is consistent with the sintering and densification parameters (Table 3.2) such as a relative density of 59.7% with an open porosity of 44.3% and resulting 25.08 % weight loss due to higher open channels in the microstructure. In general, all acicular particles/grains were uniform in size and less than about 2 μm, and there was no grain growth except for neck formations at the contact points. Figure 3.34(b) shows a dense microstructure for the AB ceramic. Because initial acicular particles were uniform in size (see Figure 3.34(a)) for particle/grain size distribution), abnormal grain growth was not observed, except for larger grains in the range of about 5-10 μm and a few in excess of 10 μm, which is typical for liquid phase sintered ceramics by means of the solution of smaller particles in the liquid and precipitation on larger particles. The liquid phase was likely $CaAl_2B_2O_7$ phase that melted at 1098°C [4]. The fracture type was mostly transgranular, and anisotropic grains were also

evident due to initial acicular particles. Figure 3.34(c) shows for the ABG ceramic that 30 wt% glass was insufficient to effectively penetrate through the pores among irregularly-packed Al borate particle network because Al borate ceramics had naturally porous microstructure due to its acicular particle shape (see Figure 3.34(a)). However, glass melted at 1180°C [59] and wetted the Al borate particles, and then provided 3D interconnections by filling up the open pore network up to certain extent. In addition, the Al borate grains (not exactly acicular in shape as compared to those in Figure 3.34(a) were embedded within the continuous glassy phase network without any grain growth, which may indicate a dominant early stage liquid phase sintering (i.e., rearrangement) and localized solution-precipitation stage due to porous network and limited diffusion distances, although exact Al borate solubility in glass is not known. Figure 3.34(d) shows a dense microstructure for the AMG ceramic. The same amount of the glass phase (e.g., 30 wt%) induced a similar effect as in the ABG sample (Figure 3.34(c)) but filled up the open pore network more efficiently because of the less amount of acicular Al borate particles (35 wt%) as well as presence of mullite powders (35 wt%), preventing the formation of irregular pore networks as seen in Figure 3.34(a). Therefore, flow of molten glass was expected to be easier, resulting in an efficient rearrangement of the Al borate and mullite powders as well as subsequently leading to densification by means of liquid phase sintering. In addition, liquid phase sintering facilitated a solid solution formation between Al borate and mullite grains, as also reflected in Figure 3.30. The fracture type is transgranular and abnormal grain growth is not observed. The same glass composition was used to prepare glass+Al_2O_3 composites and it was reported that 20 and 40 wt% glass induced a liquid phase sintering (sintering temperatures of 1350°C and 1200°C, respectively) and 50-60 wt% glass induced viscous sintering (sintering temperature of 850°C) [59].

The presence of similar elements such as Al and Si in glass, Al borate and mullite makes the grain analysis difficult although backscatter electron mode in SEM yields atomic number dependence contrast. Therefore, an SEM-EDS elemental mapping of the AMG ceramic sintered at 1350°C for 1h was carried out and the result is shown in Figure 3.35. Table 3.3 shows the calculated elemental ratios in the AMG composition. Mullite has also some other phases such as CaO, Na_2O, K_2O together with 5-10% glassy phase (see Table 2.4) but some oxides (e.g., Fe_2O_3, TiO_2, MgO) are excluded

in the analysis. Note again that EDS analysis is a qualitative technique and analysis of the light elements such as B, C, O is difficult to precisely detect, as explained before. Therefore, relatively uniform and strong B distribution all over the microstructure (e.g., without any regional abundance like other elements) could be wrong or misleading when B content in the composition is considered in Table 3.3. In addition, the EDS analysis surface was a fracture surface and was not perfectly flat. The elemental mapping of Ca, Na and K enables us to locate the glass and mullite phases such that the regions much richer in Ca, Na and K together with relatively bigger grains can belong to the glassy phase because the d_{50} (d_{90}) size is 2.12 μm (3.91 μm) for glass (see Figure 3.27) and 0.34 μm (1.21 μm) for mullite (see Figure 3.26). In addition, when the ratios in Table 3.3 are considered, glass is much richer in Si and more deficient in Al, and vice versa for mullite. Therefore, Si-rich regions particularly reveal the glassy phase and Si-deficient (or Al-rich) regions can belong to the mullite grains (in fact, a solid solution phase between mullite and $Al_{18}B_4O_{33}$, as explained for Figure 3.30 and Figure 3.34(d)).

Table 3.3 Calculated elemental ratios in the AMG composition

Phases	Elements, wt%						
	Al	B	O	Si	Na	K	Ca
$Al_{18}B_4O_{33}$	16.08	1.43	17.48	-	-	-	-
Glass	2.54	-	13.73	9.46	1.09	0.81	2.36
Mullite	13.34	-	16.77	4.25	0.05	0.17	0.01

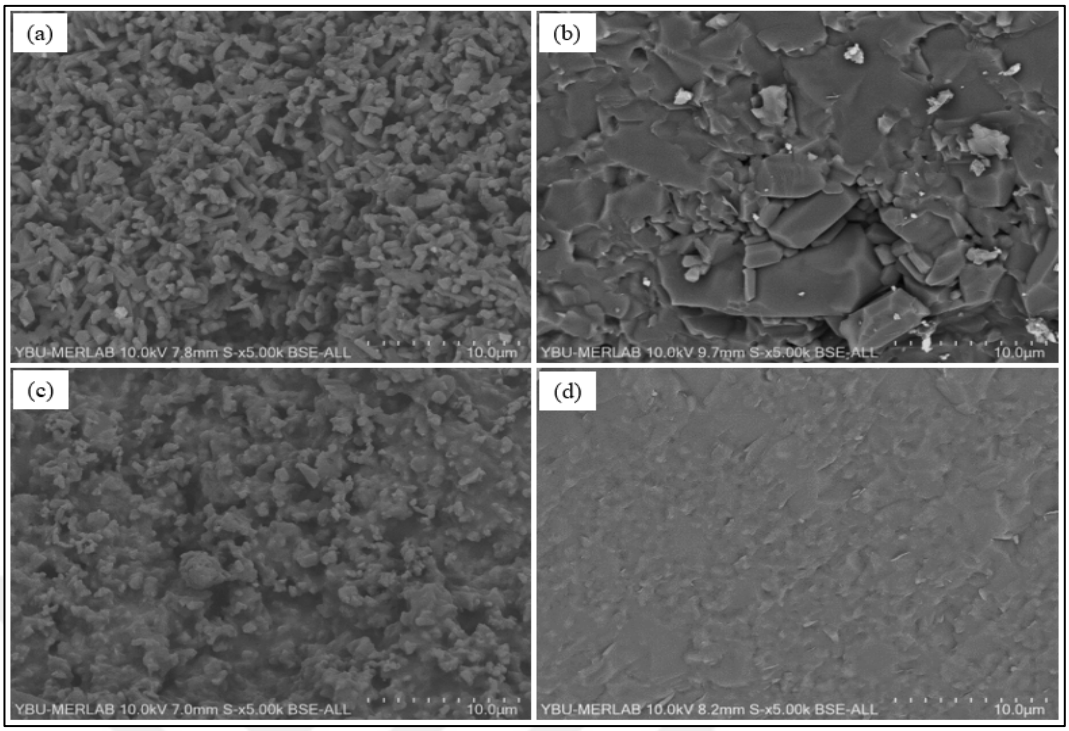

Figure 3.34 SEM pictures of the (a) PAB, (b) AB, (c) ABG and (d) AMG ceramics sintered at 1350°C for 1h.

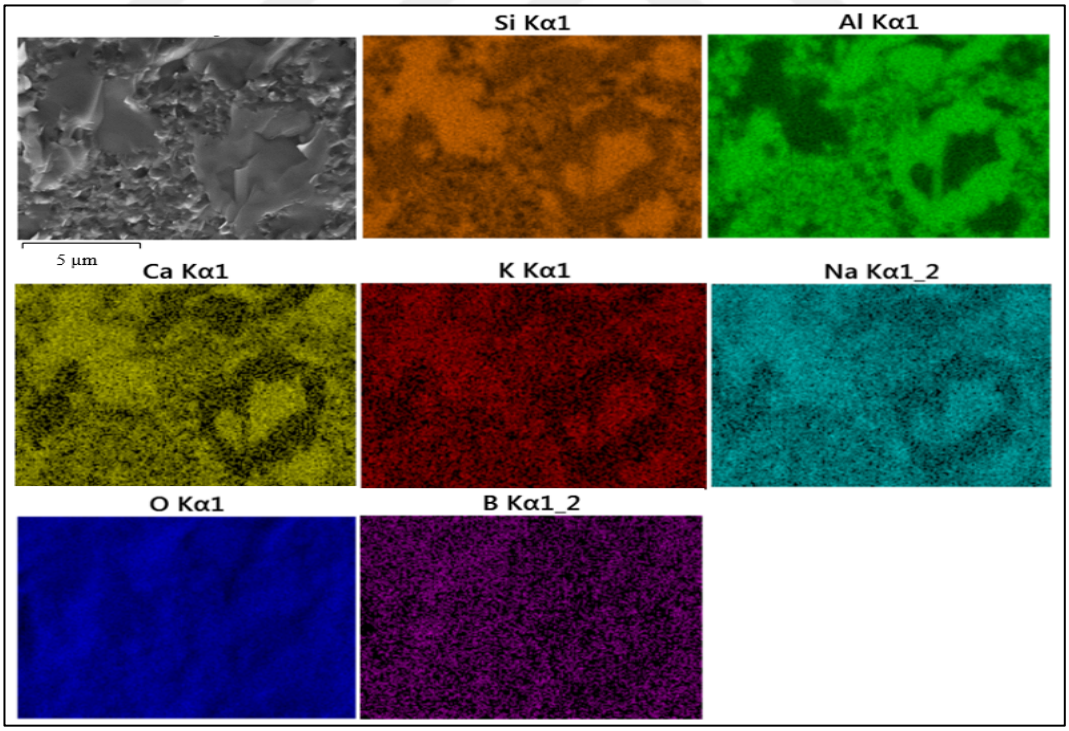

Figure 3.35 SEM-EDS elemental mapping of the AMG ceramic sintered at 1350C for 1h.

There is a correlation between weight loss (Table 3.2) and XRD results (Figure 3.33). Weight losses in the ABG and AMG samples are much lower as compared to other

ceramics, which may result from the presence of glassy phase in the structure in that glassy phase covers the $Al_{18}B_4O_{33}$ particles and prevents evaporation of B_2O_3 from the particle or grain surfaces (see Figures 3.34(c) and 3.34d). In other words, $Al_{18}B_4O_{33}$ decomposition to Al_2O_3 can be restricted because glass phase has a low melting temperature of 1180°C [59], embracing the $Al_{18}B_4O_{33}$ particles before reaching to the sintering temperature. Weight loss in the AB sample is relatively higher as compared to other ceramic samples except for the PAB, which may stem from CaO added as a sintering additive accelerating weight loss due to liquid phase sintering. In other words, relatively easier evaporation of B_2O_3 from $Al_{18}B_4O_{33}$ phase occurs when $Al_{18}B_4O_{33}$ dissolves in a liquid during solution stage of the liquid phase sintering. However, densification of the microstructure then limits B_2O_3 evaporation due to elimination of open or free surfaces (i.e., replacement of solid-vapor interfaces with solid-solid interfaces). For the PAB sample, the weight loss is the highest as compared to other ceramic samples but its XRD shows that main peaks belong to $Al_{18}B_4O_{33}$. Particularly, Al_2O_3 peak intensities are very low, which indicates limited $Al_{18}B_4O_{33}$ decomposition. A very low relative density of 59.7%, or correspondingly very high open porosity of 44.3% (see Figure 3.34(a)), supposedly yields more open or free surfaces, facilitating B_2O_3 evaporation but it seems that 1350ºC is not a high enough temperature to cause accelerated evaporation during solid state sintering. The phase analysis of the AB and PAB compositions indicate that additives are very important to control $Al_{18}B_4O_{33}$ decomposition (or, B_2O_3 evaporation). Several results were reported in literature regarding the decomposition temperature of $Al_{18}B_4O_{33}$ in air due to evaporation of B_2O_3 such as temperatures higher than 1350 ºC or 1400ºC [3,4,56], 1440ºC [68] and at 1450ºC [79]. Furthermore, its decomposition started as low as 1200ºC when it was heated at 2ºC/min [80]. Gönenli and Messing [73] studied thermal stability of commercial $Al_{18}B_4O_{33}$ whiskers by heating them in air from 1400 to 1600ºC for 6 h, and reported that it was stable at 1400ºC, decomposed to α-Al_2O_3 at 1500ºC with some residual $Al_{18}B_4O_{33}$ phase, and α-Al_2O_3 was the only phase at 1600ºC, as determined by XRD. Figure 3.15 shows that $Al_{18}B_4O_{33}$ did not decompose until 1400ºC during powder synthesis but partial decomposition from the surface for the PAB and AB ceramics took place during sintering at 1350ºC for 1h. Note that XRD detects the phases on the surface or sub-surface. Therefore, Al_2O_3 detected from the as-sintered

surfaces is due to the formation of Al_2O_3-rich layers on the particle or grain surfaces due to B_2O_3 evaporation. Furthermore, the XRD peak intensities depend on volumetric quantities and mass absorption coefficients of the constituent phases. Materials with high atomic numbers have high absorption coefficients [81]. Therefore, the $Al_{18}B_4O_{33}$ peaks have lower intensities as compared to the Al_2O_3 peaks in the XRD patterns due to its lower mass absorption coefficient (e.g., 8.27 cm^2/g for B_2O_3, 28.68 cm^2/g for $Al_{18}B_4O_{33}$, 31.78 cm^2/g for Al_2O_3, 33.08 cm^2/g for mullite and 52.7 cm^2/g for anorthite ($Al_2CaO_8Si_2$) [82]).

Sintering is very difficult for the Al borate ceramics without sintering additive since sintered Al borate ceramics have naturally porous microstructure due to needle shaped powders/grains [4,55], as also observed in this study. $Al_{18}B_4O_{33}$ sample sintered at 1350°C for 1h without any sintering additive had a relative density of 61.2 %, but CaO addition improved densification. A relative density of 77.9 %, 87.8 % and 96.6 % were achieved for the CaO amount of 0.25 wt%, 0.5 wt% and 1-2 wt%, respectively, because CaO caused a liquid phase sintering (likely by forming $CaAl_2B_2O_7$ phase that melts at 1098°C) and enhanced densification. The relative densities were 94.1% and 96.6% for the samples prepared with 4 wt% $CaAl_2B_2O_7$ (sintered at 1350°C for 1h) and 1 wt% MgO (sintered at 1450°C for 1h), respectively [4]. $Al_{18}B_4O_{33}$ ceramics had open porosities between 35% and 50% after being reaction-sintered between 1100°C and 1400°C due to needle-like form of the Al borate powders [55]. Dry-pressed ceramics prepared from attrition-milled $Al_{18}B_4O_{33}$ powder with aspect ratios between 1 and 4 reached a relative densification level of 85.1 % with an open porosity of 10.91 % after sintering at 1300°C for 5 h [56]. The ceramics had a density of 1.91 g/cm^3 (39.3 % open porosity) and a crystalline phase ratio of 58 wt% Al_2O_3 and 42 wt% $Al_{18}B_4O_{33}$ after reaction sintering of calcined Al_2O_3 and H_3BO_3 (13 wt% B_2O_3) at 1300°C for 2h. Similarly, the ceramics had a density of 1.75 g/cm^3 (45.4 % open porosity) and a crystalline phase ratio 0.7 wt% Al_2O_3 and 97.4 wt% $Al_{18}B_4O_{33}$ and 1.9 wt% A_2B, after reaction sintering of calcined Al_2O_3 and H_3BO_3 (26 wt% B_2O_3) at 1300°C for 2 h [16]. Therefore, the densification and phase analysis of the ceramics are compatible with the literature values with (AB) and without CaO addition (PAB). The anorthite-based glass addition as a sintering additive was applied in this study. The AMG ceramics (together with mullite phase) reached about 95% relative density

with near-zero open porosity and water absorption levels. The ABG ceramics reached a limited densification of 89.4% due to insufficient filling of glass phase thru the pores. In other words, modification of the microstructure with glass and mullite allowed us to fabricate a fully dense microstructure (AMG) with near-zero open porosity and water absorption levels.

3.3 Dielectric, Mechanical and Thermal Properties

Table 3.4 shows the dielectric properties of the ceramics as function of composition and sintering temperature. Dielectric constants varied in between 4 and 6.6 at 5 MHz for all ceramics. The dielectric constant of the Al borate sample sintered at 1350°C for 1h with 2 wt% CaO and with a porosity of 0.3% was reported as 5.6 at 2 MHz [4], which is close to the dielectric constant of the AB ceramics (e.g., 5.35-6.01 at 5 MHz). The PAB ceramic had a lower value due to its low densification. A dielectric constant of 6.39 was calculated using the logarithmic mixture rule (see Equation 3.6) for the AMG composite, using dielectric constants of 6.37 for glass [59], 7.4 for mullite [83] and 5.6 for Al borate [4]. The ABG ceramic had a relatively higher dielectric constant with respect to its higher porosity level, although the logarithmic mixture rule gave a dielectric constant of 5.85, which might be attributed to the 3D glass network with both open and closed porosities in the microstructure (see Figure 3.34(c) and Table 3.2). It is important to note that minor phases such as Al_2O_3, B_2O_3-based and unknown phases (Figure 3.33), in addition to the densification levels, definitely affect the dielectric properties, resulting in some variations in the measured values.

Table 3.4 Dielectric properties of the ceramics measured at 5 MHz

	AMG		PAB		ABG		AB	
Temperature, °C	**Dielectric constant**	**Dielectric loss**	**Dielectric constant**	**Dielectric loss**	**Dielectric constant**	**Dielectric loss**	**Dielectric constant**	**Dielectric loss**
1300	5.54	0.0237	-	-	-	-	5.35	0.0542
1350	5.13	0.0542	4.05	0.0463	6.58	0.0028	6.01	0.0915
1400	5.47	0.0188	-	-	-	-	5.38	0.0065

The Vickers hardness of the samples were measured from the polished surfaces of the ceramics and are given in Table 3.5. Standard deviations were also included to show hardness variations. The hardness values directly followed the densification levels (see Table 3.2). Therefore, the maximum hardness values were obtained at a sintering temperature of 1350ºC at which maximum density was achieved for the AB (relative density of 95.4%) and AMG (relative density of 94.8%) samples. Ray et al. [4] sintered Al borate ceramics with 2 wt% CaO at 1350ºC (a relative density of 96.6%) and reported a hardness value of 1263 HV. Note that the hardness values of $Al_{18}B_4O_{33}$ wires were measured to be 12.8 GPa (or, 1280 HV) [84]. In our study, hardness value of the AB sample sintered at 1350ºC with a relative density of 95.4% was measured as 998±52 (max. 1077 HV). Lower hardness can be attributed to the relatively lower densification. For the AMG sample, the hardness (924±118 and max. 1163 HV) was lower as compared to reported pure Al borate hardness value of 1263 HV [4] due to presence of mullite (1089±9 HV [66], [83]) and particularly glassy phase (591 HV [59]) despite its high densification level of 94.8%. A hardness value of 925 for the AMG sample was calculated using the logarithmic mixture rule (see Equation 3.6). Hardness values of the PAB and ABG samples were lower as compared to other ceramic samples due to their lower density values. Particularly, the PAB ceramic had a very low hardness of 98 ± 10 due to almost no densification in the microstructure (Figure 3.34(a)). In addition, glassy phase gave rise to a lower hardness level for the ABG sample (825±120). A hardness value of 975 for the ABG sample was calculated

using the logarithmic mixture rule (see Equation 3.6). Porosity-hardness relationship was reported for the A_9B_2 ceramics prepared by dry pressing. The samples with open porosity levels of 20.53% (sintered at 1250°C for 2h), 17.54% (sintered at 1300°C for 2h) and 10.91% (sintered at 1300°C for 5h) had hardness values of 421 HV, 453 HV and 612 HV, respectively. The sample sintered at 1300°C for 10h with an open porosity of 16.52% had a hardness value of 656 HV due to presence of some Al_2O_3 phase resulting from B_2O_3 evaporation [56]. These results indicate that densification and phases present determine the hardness of the ceramics (AB and PAB) and composites (AMG and ABG).

Table 3.5 The Vickers hardness values (HV) of the ceramic samples

Temperature, °C	**AMG**	**AB**	**PAB**	**ABG**
1300	718 ± 26	792 ± 160	-	-
1350	924 ± 118	998 ± 52	98 ± 10	825 ± 120
1400	901 ± 134	893 ± 84	-	-

Thermal conductivity of the samples sintered at 1350°C are compared in Table 3.6. The thermal conductivity of the AB sample was higher when compared to other samples due to both higher densification (95.4% relative density) and high thermal conductivity of the Al borate phase. The thermal conductivity was measured as nearly 6.5 and 8 W/m.K at 25°C, 3.8 and 3.4 W/m.K at 1000°C for the hot-pressed (99.6% relative density) and cold-pressed samples (96.6% relative density), respectively [4]. Hence, thermal conductivity of the AB sample is higher among all samples and compatible with the literature values. In the ABG and AMG samples, the thermal conductivity was the lowest due to presence of a glassy phase (0.85 W/m.K [59]). The crystalline phases in the microstructures were embraced by amorphous glassy phase, which caused a sharp decrease in overall thermal conductivity of the AMG and ABG samples. In literature, the same glass phase also dramatically decreased the thermal conductivity of the glass+Al_2O_3 composites from 36 W/m.K for Al_2O_3 [85] to 1.25 W/m.K for 40 wt% glass and to 1.31 W/m.K for 55 wt% glass [59]. As a result, glass phase decreased thermal conductivity of the samples. A thermal conductivity value of 3.7 W/m.K for the ABG sample and 3.3 W/m.K for the AMG sample was calculated

using the logarithmic mixture rule (see Equation 3.6). Lower values can be attributed to the relatively lower densification levels. The PAB sample had a thermal conductivity of 2.70 W/m.K in spite of its very high open porosity of 44.3% (Table 3.2). Similarly, reactive sintering of calcined Al_2O_3 and H_3BO_3 in air (initial B_2O_3 amount was 26 wt%) at 1300°C for 2h resulted in 45.4 % open porosity and had an effective thermal conductivity of 2.7 W/m.K (i.e., calculated using parallel mixing rule) [16], which indicates that porosity level is critical for thermal properties.

Table 3.6 Thermal conductivity values of the samples measured at room temperature

Sample	Thermal Conductivity, W/m.K	Heat Capacity, C_p $mJ/m^2.K$	Thermal Diffusivity, mm^2/s
AMG	1.73 ± 0.087	4.217	0.417
AB	7.26 ± 0.033	3.626	2.021
PAB	2.70 ± 0.065	1.205	2.767
ABG	1.73 ± 0.066	4.289	0.401

3.4 Possible Applications

Full measured properties of the ceramics sintered at 1350°C are summarized in Table 3.7. First of all, acicular Al borate particles can be used as a reinforcement agent for metals and metal alloys. For example, AC8A aluminum alloy was reinforced with 20 vol% Al borate whiskers, and significant mechanical and thermal property improvements were achieved in the resulting composite [11]. In addition, Al borate whiskers were used to texture mullite ceramics [73] and mullite-ZrO_2 composites [74,75] with significant anisotropic mechanical property improvements [76].

The PAB ceramic is suitable for applications such as filter and metal matrix ceramic composite by means of metal infiltration into sintered open-network preform. The preform can also be prepared in a complex 3D shape for specific products by additive manufacturing method. Acicular shape grains/particles and highly open network structure (see Figure 3.34 (a)) make the PAB ceramics suitable for those applications. Similar properties to the metal matrix ceramic composites are expected.

Table 3.7 shows that the AB and AMG ceramics have low dielectric constants and similar mechanical (e.g., hardness) properties, which suggests that these ceramics can be suitable candidates for radome applications. In addition to the densification, open porosity and water absorption levels (i.e., both as low as possible to satisfy impermeability to water) are important factors for selection to protect radome from mechanical and electrical failures [86, 87]. Low dielectric constant and loss are desired for radome applications to widen frequency band [86] and to decrease insertion losses [26]. In other words, the total energy loss must be minimum due to reflection of energy [86,88], which necessitates lower dielectric constant and loss. Furthermore, transmission speed of signal increases with decreasing dielectric constant [89,90]. Thermal conductivity is also a critical parameter to facilitate rapid heat dissipation and improve thermal shock resistance [87]. Therefore, a high thermal conductivity of the AB ceramic is particularly a great asset from the thermal shock resistance point of view although its dielectric constant is slightly higher. The AMG composite has an advantage of a lower dielectric constant but has also a lower thermal conductivity with respect to the AB ceramic although they have similar densification levels. In general, dielectric loss values should be modified to reach lower values for better electromagnetic performance (or, minimize power loss) for all ceramics. It was reported that porosity decreases dielectric constant (desired) but at the same time increases dielectric loss (undesired) [87], which states that densification as well as composition are critical for dielectric properties. Glass phase lowers thermal conductivity, but it can be easily overcome by adding nano-fillers such as hBN [91]. A thorough review of radome ceramics are compiled in a recent article [91]. In brief, radome applications requires an optimization of dielectric, mechanical and thermal properties as a function of sintering parameters such as densification and microstructure. The current results indicate that the AB and AMG ceramics can be suitable candidates for radome applications. In addition, the AMG ceramics can also be used as thermal insulators due to their low thermal conductivity values. The AB ceramic can also be used as a substrate material due to its high thermal conductivity and low dielectric constant.

The ABG composites need either higher glass content to increase densification for radome and substrate applications similar to the AB and AMG ceramics or lower glass

content to increase porosity for filter and metal matrix ceramic composite applications similar to the PAB ceramics. They can also be used as thermal insulators.

Table 3.5 Properties of all ceramics sintered at 1350°C for 1h

Sample	Bulk Density, g/cm^3	Relative Density (Open Porosity), %	Thermal Conductivity at 25°C, W/m.K	Dielectric Constant at 5 MHz	Dielectric Loss at 5 MHz	Vickers Hardness
AB	2.8	95.4 (2.86)	7.26	6.01	0.0915	998 ±52
PAB	1.75	59.7 (44.3)	2.7	4.05	0.0463	98 ±10
ABG	2.46	89.4 (5.77)	1.73	6.58	0.0028	825 ±120
AMG	2.65	94.8 (0.04)	1.73	5.13	0.0542	924 ±118

CHAPTER 4

CONCLUSION

Aluminum borate is a suitable ceramic for structural applications due to its low thermal expansion coefficient (4.5×10^{-6}/°C), high elastic modulus (400 GPa), low density (2.93 gr/cm^3). In particular, it is considered as thermal insulator due to its low thermal conductivity (4 - 6 W/m.K up to 1000°C). However, its acicular particle shape makes densification difficult during sintering. In this thesis, Al_2O_3 and domestic B_2O_3 source were utilized to synthetize Al borate powders by solid state calcination technique and then basic characterizations (phase formation, microstructural evolution, mechanical, thermal, dielectric properties) were completed. Al_2O_3/B_2O_3 powder mixtures were prepared at mole ratios of 5.73, 4.41, 3.09, 1.77, 1.3, 0.87 and 0.58. Excess B_2O_3 was used to assist crystallization of Al borate phase in a B_2O_3-rich liquid phase. Al borate was synthesized at a mole ratio of 0.87 (44 wt% B_2O_3) which deviated from the stoichiometric mole ratio of 4.5 (e.g., 13.17 wt% B_2O_3), which may be attributed to some factors such as; i) existence of initially present absorbed water (or, existence of boric acid) that first requires boric acid decomposition to B_2O_3, subsequent B_2O_3 melting and dissolution rate of Al_2O_3 in the melt, ii) change in the melt viscosity as a function of excess B_2O_3 and temperature, iii) evaporation rate of B_2O_3 with increasing calcination temperature particularly from open-lid crucible. These factors changed the kinetics of crystallization from standpoint of the solute (Al_2O_3 and/or other Al borate compounds at different Al_2O_3/ B_2O_3 mole ratios) saturation in the melt and subsequent phase transformation. $Al_{18}B_4O_{33}$ formation was completed at T≥1200°C in the resolution limit of the XRD analysis. SEM images indicated that $Al_{18}B_4O_{33}$ particles were not acicular in shape when first formed. Acicular $Al_{18}B_4O_{33}$ particles were fully obtained for the 44 wt% and the 54.1 wt% B_2O_3 mixtures when Al_2O_3 was all consumed and/or $Al_{18}B_4O_{33}$ was totally formed. A calcination temperature of 1300°C for 1h yielded the optimum temperature to synthetize almost full acicular $Al_{18}B_4O_{33}$ particles together with minimum amount B_2O_3-based phase.

It is difficult to densify Al borate ceramic due to its needle-like particle shape during sintering. Therefore, its densification was controlled by a composite approach. Mullite was selected due to its similar crystal structure and properties to the Al borate. Glass and CaO were selected to induce liquid phase sintering. Al borate+2 wt% CaO (AB), %100 Al borate (PAB), %35 Al borate+%35 mullite+%30 glass composite (AMG) and %70 Al borate+%30 glass composite (ABG) were prepared by gel casting method and sintered at 1300ºC, 1350ºC and 1400ºC for 1h. Gel casting was preferred to improve powder compaction and enhance densification as well as to fabricate Al borate ceramics in complex shapes for specific applications. The highest densification was achieved at 1350ºC for the AB (95.4% relative density) and AMG (94.8% relative density) samples. The ABG sample had a relative density of 89.4% due to the presence of insufficient glass content. The PAB sample has the lowest bulk density of 1.75 g/cm^3 (59.7% relative density) due to acicular Al borate particles forming open network in the microstructure. Weight losses were relatively low for the AMG (1.13 %) and ABG (1.67%) compositions in that glassy phase covered the $Al_{18}B_4O_{33}$ particles and prevented evaporation of B_2O_3 from the particle or grain surfaces. The weight loss was the highest for the PAB sample (25.08%) due to its open-network microstructure facilitating B_2O_3 evaporation.

Phase analysis was carried out both from as-sintered ceramic surfaces to evaluate surface composition due to possible B_2O_3 evaporation as well as from polished ceramic surfaces to evaluate bulk composition. All main peaks belonged to Al_2O_3 when the XRD patterns were taken from the as-sintered AB ceramic surface. However, the $Al_{18}B_4O_{33}$ peaks were almost the only peaks when the surface was polished, revealing that B_2O_3 evaporation was very severe from the surfaces causing decomposition of the $Al_{18}B_4O_{33}$ phase into Al_2O_3. There was a shallow hump between 2θ~15-35° due to the presence of an amorphous glass phase in the AMG and ABG composites. In addition, Al_2O_3 phase did not form when XRD was taken from the as-sintered and polished surfaces, but anorthite ($(Ca,Na)(Si,Al)_4O_8$) crystallization from the glass was observed in both composites. In the AMG sample, mullite dissolved more in the glass phase and then precipitated on the $Al_{18}B_4O_{33}$ particles (i.e., epitaxial nucleation of mullite on $Al_{18}B_4O_{33}$ particles) with the formation of a solid solution at the interface. In the ABG sample, the main peaks belonged to $Al_{18}B_4O_{33}$ in both surface and polished XRD

patterns but other minor phases such as Al_2O_3, an unknown and B_2O_3-based liquid phases were also present.

Dielectric, mechanical and thermal properties of the samples were investigated and possible application areas were evaluated. The PAB ceramic had the lowest dielectric constant (4.05) due to its low densification. The ABG ceramic had the highest value (6.58) with respect to its higher porosity level, which might be attributed to the 3D glass network with both open and closed porosities in the microstructure. The Vickers hardness values were 998 ±52 for the AB, 924 ±118 for the AMG, 825 ±120 for the ABG and 98 ±10 for the PAB ceramics, which indicated that densification and phases determined the hardness of the samples. Similarly, the AB sample had a thermal conductivity of 7.26 W/m.K but the PAB sample had 2.7 W/m.K due to its low densification. The crystalline phases (e.g., Al borate and/or mullite) in the microstructures were embraced by amorphous glassy phase, which caused a sharp decrease in overall thermal conductivity of the AMG and ABG (1.73 W/m.K) samples. The PAB ceramic is suitable for applications such as filter and metal matrix ceramic composite by means of metal infiltration into sintered open-network preform. The AB and AMG ceramics have high densification and low dielectric constants, making them suitable candidates for radome and substrate applications. Particularly, a high thermal conductivity of the AB ceramic is a great asset from the thermal shock resistance point of view. The AMG ceramics can also be used as thermal insulators due to their low thermal conductivity values. The ABG composites need either higher glass content to increase densification for radome and substrate applications similar to the AB and AMG ceramics or lower glass content to increase porosity for filter and metal matrix ceramic composite applications similar to the PAB ceramics. They can also be used as thermal insulators.

In this study, acicular Al borate particles were successfully synthetized by solid state method. These particles can be used as a reinforcement agent for metals and metal alloys, and also to texture structural ceramics such as mullite-based ceramics with significant anisotropic mechanical property improvements. The anorthite-based glass addition as a sintering additive was applied for the first time in literature. The AMG ceramics reached 94.8% relative density with near-zero open porosity and water

absorption levels due to mullite addition. The ABG ceramics reached a limited densification of 89.4% due to insufficient filling of glass phase thru the porous network. In other words, modification of the microstructure with glass and mullite allowed us to fabricate a fully dense microstructure (AMG) with near-zero open porosity and water absorption levels.

REFERENCES

[1] Gliesse, P.J.M. & Foster, W.R., "The System Al2O3–B2O3", Nature, 195, 69–70, 1962.

[2] Fisch, M., Armbruster, T., Rentsch, D., Libowitzky, E. & Pettke T., "Crystal-chemistry of mullite-type aluminoborates Al18B4O33 and Al5BO9: A stoichiometry puzzle", Journal of Solid State Chemistry, 184, 70-80, 2011.

[3] Hoffmann, T.J.N., Hooper, M.M., Murshed, O. Dolotko, Revay, Z., Senyshyn, A., Schneider, H., Hanna, J.V., Gesing, Th.M. & Fischer, R.X., "Formation, stability and crystal structure of mullite-type Al6xBxO9", Journal of Solid State Chemistry, 243, 124-135, 2016.

[4] Ray S. "Preparation and Characterization of Aluminum Borate", Journal of the American Ceramic Society", 75(9), 2605-6049, 1992.

[5] Mazza, D., Vallino, M. & Busca G., "Characterization of microporous amorphous alumina–boria", J.Am.Ceram.Soc.75(7), 1929–1934, 1992.

[6] Garsche, M., Tillmanns, E., Almen, H., Schneider, H. & Kupcik, V., "Incorporation of chromium into aluminium borate", Eur.J.Mineral, 3(5), 793–808, 1991.

[7] Sokolova, E.V., Azizov, A.V., Simonov, M.A., Leoniuk, N.I. & Belov N.V., "Crystal-structure of synthetic ortho 3-borate" , Dokl.Akad.Nauk SSSR, 243(3), 655–658, 1978.

[8] Ihara, M., Imai, K., Fukunaga, J. & Yoshida, N., "Crystal structure of boroaluminate", 9Al2O3.2B2O3. J. Ceram. Soc. Jpn., 78(2), 1014, 1980.

[9] Yla-Jaaski, J. & Nissen, H.U., "Investigation of superstructures in mullite by high resolution electron microscopy and electron diffraction", Phys. Chem. Minerals, 10(2), 47–54, 1978.

[10] El-Hakam, S.A. & El-Sharkawy, E.A., "Structural characterization and catalytic properties of aluminum borates–alumina catalysts", Mater. Lett., 36(1), 167–173, 1998.

[11] Suganuma, K., Fujita, T. & Sasaki G., "Evaluation of strength and heat-resistance for aluminum-borate whisker reinforced AC8A aluminum alloy composite", J Jpn Inst Light Met., 41(3), 270–275, 1991.

[12] Wang, K., Zhou, H., Liu, X., Sun, Chen, X. & Ruan H., "A lithium aluminium borate composite microwave dielectric ceramic with low permittivity, near-zero shrinkage, and low sintering temperature", Journal of the European Ceramic Society, 39(4), 1122-1126, 2019

[13] Pandey, N., Chakrabarty, I., Barkane, K., Mehta, M. R. & Majhi R., “Microstructure, mechanical and wear properties of aluminum borate whisker reinforced aluminum matrix composites”, Trans. Nonferrous Met. Soc. China, 30(4), 1731−1742, 2020.

[14] Geng, L., Guan, L. & Lü, K., “Effects of whisker surface treatment on microstructure and properties of Al18B4O33w/6061Al composites”, Trans. Nonferrous Met. Soc. China, 20(2), 349-354, 2010.

[15] Wang, L., Hu, J. & Fei, W.D, “Fracture Behaviour of aluminum borate whisker, reinforced aluminum alloy 6061 composite”, Material Science and Engineering 497(5), 358-362, 2008.

[16] Hernández, F., Suárez, G., Cipollone, M., Esteban, F. & Rendtorff, M., “Mechanical behavior and microstructure of porous needle: Aluminum borate (Al18B4O33) and Al2O3-Al18B4O33 composites”, Ceramics International, 43(2), 11759–11765, 2017.

[17] Elssfah, E., Song, H. & Tang, C., “Synthesis of aluminum borate nanowires via a novel flux method”, Mater Chem Phys., 101(4), 499–504, 2007

[18] Cheng, C., Ding, X. & Shi, F., “Preparation of aluminum borate nanowires”, J Cryst Growth., 263(2), 600–604, 2004.

[19] Peng, L., Li, X. & Li, H.,. “Synthesis and microstructural characterization of aluminum borate whiskers”, Ceram Int., 32, 365–368, 2006.

[20] Li, Y. & Chang, R., Synthesis and characterization of aluminum borate (Al18B 4O33, Al4B2O9) nanowires and nanotubes. Mater Chem Phys., 97, 23–30, 2006

[21] Yoshida, M., Takeuchi, S. & Pan, J., “Preparation and characterization of aluminum borate whisker reinforced magnesium alloy composites by semi-solid process”, Adv Compos Mater., 8(1), 259–268, 1999.

[22] Zhou, J., Su, D., Luo, J. & Zhong, M., “Synthesis of aluminum borate nanorods by a low-heating-temperature solid-state precursor method”, Materials Research Bulletin, 44(2), 224-226, 2009.

[23] Wang, J., Ning, G. & Yang X., “Large-scale synthesis of Al4B2O9/Al18B4O33 whiskers via a novel method ”, Mater Lett., 62(8–9), 1208–1211, 2008.

[24] Gonzalez-Martinez, I., Bachmatiuk, A., Gorantla, S., Bezugly, J., Gemming, B., Cuniberti, G. & Ru¨mmeli, M. H., “Defect assisted thermal synthesis of crystalline aluminum borate nanowires”, Journal of Applied Physics, 112(5), 024308, 2012.

[25] Schneider, H., Schreuer, J. & Hildmann, B., “Structure and properties of mullite”—A review, Journal of the European Ceramic Society, 28(3), 329–344, 2008.

[26] Schneider, H., Okada, K., Pask, J. A. & Rahman, S. H., “Mullite and mullite ceramics”. New York: J. Wiley. 1994

[27] Schneider, H., Fischer, X. & Schreuer J., “Mullite: Crystal Structure and Related Properties”, J. Am. Ceram. Soc., 98(10), 2948–2967, 2015.

[28] Bowen, N. & Greig, J., "The System: AI2O3-SiOl," J. Am. Ceram. SOC, 54(4), 238-254, 1924.

[29] Aksay, I. & Pask, J., "Stable and Metastable Equilibria in the System SiO2-AI2O3," J. Am. Ceram. SOC., 58(11), 507, 1975.

[30] Angel, R. & Prewitt, C., Crystal structure of mullite, Amer. Min., 71(3), 1476-1482, 1986.

[31] Mullite-review. (n.d). Retrived April 14, 2022, from http://shodhganga.inflibnet.ac.in/bitstream/10603/77324/9/09_chapter%202.pdf

[32] Aksay, I. A., Dabbs, D. M. & Sarikaya, M. “Mullite for structural, electronic, and optical applications”, Journal of the American Ceramic Society”, 74(10), 2343-2358, 1991.

[33] Ruh, R. & Chizever, H. M. “Permittivity and Permeability of Mullite-SiC-Whisker and Spinel-SiC-Whisker Composites”, Journal of the American Ceramic Society, 81(4), 1069-1070, 1998.

[34] AZO materials- Mullite. (n.d.). Retrieved Apr 14, 2022, from https://www.azom.com/properties.aspx?ArticleID=925

[35] Memsnet- material: Mullite, bulk. (n.d). Retrieved Apr 14, 2022, from https://www.memsnet.org/material/mullite3al2o32sio2bulk/

[36] Accuratus-mullite ceramic properties. (n.d). Retrieved Apr 14, 2022, from https://www.accuratus.com/mullite.html

[37] Ferro Ceramic INC. -mullite properties. (n.d). Retrieved Apr 14, 2022, from https://ferroceramic.com/mullite/

[38] Guo, X., “Gel casting of high strength ceramics”, Diploma work in Master programme, Chalmers University of Technology, 2011.

[39] Hooshmand, A., Nordin, J. & Akhtar, F., “Porous alumina ceramics by gel casting: Effect of type of sacrificial template on the properties”, International Journal of Ceramic Engineering & Science, ISSN, 2578(10), 77-84, 2019.

[40] Koçlar, G., “Gelcasting of alumina ceramics with gelatin and carrageenan gum and investigation of their mechanical properties “, MS thesis, İzmir Institute of Technology, 2013.

[41] Young, A., Omatete, O., Janney, M. & Menchhofer, P., "Gelcasting of alumina", Journal of the American Ceramic Society, 74(3), 612-618, 1991.

[42] Tari, G., " Gel casting ceramics: A review", Am. Ceram. Soc. Bull, 82(4), 43-46, 2003

[43] Polyacrylamide Matrix (n.d). Retrieved Apr 14, 2022, from https://www.nationaldiagnostics.com/electrophoresis/article/polyacrylamide-matrix

[44] Jain,R., "Gel Electrophoresis". Retrieved Apr 14, 2022, from https://www.slideshare.net/RishabhJain413/lectut-btn202pptl13-gelelectrophoresis.

[45] Electrophoresis Acrylamide Polymerization- A practical approach. (n.d). Retrieved Apr 14, 2022, from http://www.biorad.com/webroot/web/pdf/lsr/literature/Bulletin_1156.pdf

[46] Sun, S., Cao, H., Su, H. & Tan, T., "Preparation and characterization of a novel injectable in situ cross-linked hydrogel", Polymer bulletin , 62(5), 699-711, 2009.

[47] Janney, M., Nunn, S., Claudia, A., Ogbemi O., Randy, B. & Glen, H. K, Gel casting: The Handbook of Ceramic Engineering (552-590), 1998.

[48] Hong, Y. & Mao, Z. & Wang, H. & Gao, C.& Shen, J., "Covalently crosslinked chitosan hydrogel formed at neutral pH and body temperature", Journal of Biomedical Materials Research Part A, 79(4), 913-922, 2006

[49] Drying and Binder removal. (n.d). Retrieved Apr 14, 2022, from http://old.vscht.cz/sil/keramika/Ceramic_Technology/SM-Lect-3-A.pdf

[50] Liu, P., Li, Z., Xiao, P., Liu, Z., Luo, H. & Huang, Y."Effect of the molecular weight and concentration of PEG solution on microstructure and mechanical properties of Si3N4 ceramics fabricated by gelcasting", Ceramics International, 44(8), 8800-8808, 2018.

[51] Tassilo M. & Maleksaeedi S., 'Additive manufacturing of ceramic components', Additive Manufacturing Materials, Processes, Quantifications and Applications, 53 (4), 105-161, 2018.

[52] Krause, C. (Ed). Gelcasting Molding the Future of Ceramic Forming, ORNL's. United States of America, Lockheed Martin Press. 1995.

[53] Lakhdar, Y., Tucka, C., Binner, J., Terry, A. & Goodridge, R., "Additive manufacturing of advanced ceramic materials", Progress in Materials Science, 116(3), 100736, 2021.

[54] Deckers, J., Vleugels, J. & Kruth, P., "Additive Manufacturing of Ceramics: A Review", J. Ceram. Sci. Tech., 5(4), 245-260, 2014.

[55] Hernández, M., Suárez, G., Cipollone, M., María, S. & Rendtorff N., "Formation, microstructure and properties of aluminum borate ceramics obtained from alumina and boric acid", Ceramics International 43(2), 2188-2195, 2017.

[56] Hernández, M., Suárez, G., Baudin, C., Aglietti, E.F. & Rendtorff N., "Densification of lightweight aluminum borate ceramics by direct sintering of milled powders", Journal of Asian Ceramic Socities, 6(4) 374–383, 2018

[57] Almatis datasheet. (n.d.). Retrieved Apr 14, 2022, from http://www.almatis.com/media/67477/rp_eu_rcp_006_calcines_and_reactives_for_ceramics_0115.pdf

[58] SYMULOX- Synthetic sintered mullite. (n.d). Retrieved Apr 14, 2022, from https://nabaltec.de/fileadmin/user_upload/03_produkte/03-5_synthetischer-mullit/nabaltec_tds_symulox-m72.pdf

[59] Gülsüm Meryem Dursun, Cihangir Duran, "Glass alumina composites for functional and structural applications", Ceramics International, 45(9), 12550-12557, 2019.

[60] Standard Test Methods for Apparent Porosity, Water Absorption, Apparent Specific Gravity, and Bulk Density of Burned Refractory Brick and Shapes by Boiling Water. (n.d). Retrieved Apr 14, 2022 from https://edisciplinas.usp.br/pluginfile.php/4254532/mod_resource/content/0/Norma%20determina%C3%A7%C3%A3o%20densidade%20a%20verde.pdf

[61] Callister W., "Materials science and engineering: An introduction".7th ed. USA: John Wiley & Sons. 2007

[62] Boron Trioxide. (n.d). Retrieved Apr 14, 2022, from https://en.wikipedia.org/wiki/Boron_trioxide.

[63] Luo, H., Li, Y. & Xiang R., . "Microstructural evolution and kinetics analysis of aluminum borate ceramics via solid-state reaction synthesis", Int J Appl Ceram Technol., 16(2), 2457– 2466, 2019.

[64] SEM-EDX of Boron. (n.d). Retrieved Apr 14, 2022, from http://fy.chalmers.se/~f10mh/Halvarsson/EM_intro_course_files/SEM_EDX%20Boron.pdf.

[65] Element Brochures. (n.d). Retrieved Apr 14, 2022, from https://tools.thermofisher.com/content/sfs/brochures/TN52523_E_0713M_LightElement_H.pdf.

[66] Duran, C. & Ecebaş, N, "Gel Casting Of Mullite For Radome Applications ", MS thesis, Ankara Yıldırım Beyazıt University, 2018.

[67] Dietzel, A., Scholze, H., "Investigations in the system B2O3-Al2O3-SiO2". Glastech. Ber.- Glass, 28(2), 47-51, 1955

[68] Scholze, H. & Anorg, Z., “About aluminum borates”, Allg. Chem., 284(18), 273-277, 1956.

[69] Grew, E., McGee, J., Yates, M., Wiedenbeck, M. & Thost, D., “Boralsilite (Al16B6Si2O37): a new mineral related to sillimanite from pegmatites in granulite-facies rocks”, Am Mineral, 83(5), 638–651, 1998.

[70] Peacor, D., Rouse, R. & Grew, E., “Crystal structure of boralsilite and its relation to a family of boroaluminosilicates, sillimanite, and andalusite”, Am Mineral 84(8), 1152–1161, 1999.

[71] Griesser, K., Beran, A., Voll, D. & Schneider H., “Boron incorporation into mullite, Mineralogy and Petrology”, 92(5), 309–320, 2008.

[72] Lührs, H., Fischer, X. & Schneider, H., “Boron mullite: Formation and basic characterization”, Materials Research Bulletin, 47(2), 4031–4042, 2012.

[73] Gönenli I. & Gary L., “Texturing of mullite by templated grain growth with aluminum borate whiskers” Journal of the European Ceramic Society, 21(3), 2495–2501, 2001.

[74] Duran, C. & Tür Y.K., “Templated Grain Growth of Textured Mullite/Zirconia Composites” Materials Letters, 59(2), 245-249, 2005

[75] Duran, C. & Tür Y.K., “Phase Formation and Texture Development in Mullite/Zirconia Composites Fabricated by Templated Grain Growth”, Journal of Materials Science, 41(2), 3303-3313, 2006.

[76] Öztürk, C. & Tür, Y.K., “Processing and mechanical properties of textured mullite/zirconia composites”, Journal of the European Ceramic Society 27(2), 1463–1467, 2007.

[77] Lo, C. L., Duh, J. G., Chiou, B. S. & Lee, W. H., “Low-temperature sintering and microwave dielectric properties of anorthite-based glass-ceramics,” J. Am. Ceram. Soc., 85(9), 2230–2235, 2002.

[78] Camerucci, M. A., Urretavizcaya, G., Castro, M. S. & Cavalieri, A. L., “Electrical properties and thermal expansion of cordierite and cordierite-mullite materials,” J. Eur. Ceram. Soc., 21(16), 2917–2923, 2001.

[79] Okada, K., Mutoh, H., Otsuka, N. & Yano, T., “Formation of Al2O3 whiskers by thermal decomposition of 9Al2O3.2B2O3 whiskers”, J. Mater. Sci. Let., 10(3), 588–590, 1991

[80] Rymon-Lipinski, T., Hennicke, H. W. & Lingenberg, W., “Zersetzung von 9Al2O3.2B2O3 bei hohen Temperaturen”, Keram. Z., 37(9), 450–453, 1985

[81] Noghreiyan, A., Aliakbari, E., Ebrahim-Khankook, A. & Ghasem, M., "Theoretical and experimental determination of mass attenuation coefficients of lead-based ceramics and their comparison with simulation", Nuclear Technology and Radiation Protection, 31(2), 142-149, 2016

[82] Element Datas. (n.d). Retrieved Apr 14, 2022, from https://physics.nist.gov/PhysRefData/FFast/html/form.html.

[83] Ecebaş, N., Dursun, G.M., Yeşilova, A.H. & Duran, C., "Gel casting of mullite for radome applications", Int J Appl Ceram Technol., 17(4), 264–273, 2020.

[84] Tao, X., Wang, X. & Li, X., "Nanomechanical characterization of one-step combustion-synthesized Al4B2O9 and Al18B4O33 nanowires", Nano Lett., 7(2), 3172–3176, 2007.

[85] Shackelford, J. F. & Doremus, R. H., Ceramic and glass materials: Structure, properties and processing (2008)

[86] Cary, R. H., "Avionic radome materials", Royal Radar establishment Malvern, AGARD, AR-75, 1974

[87] Abanti, N., Ramachandra, R. & Panda, P.K., "High temperature ceramic radomes (HTCR) – A review", Ceramics International, 47(15), 20793–20806, 2021.

[88] Volakis, J. L. & Burks, D. G., "Antenna engineering handbook". (53-1, 53-18), (4th. Ed.). New York, McGraw-Hill, 2007.

[89] Imanaka Y., "Multilayered low temperature cofired ceramics (LTCC) technology", JAPAN: Fujitsu Laboratories Press; 2005.

[90] D.M. Mattox, S.R. Gurkovich, A.M.K. Olenick, "Low dielectric constant, alumina-compatible, Co-Fired multilayer substrate", Ceram Eng Sci, 9(11), 1567–1578, 1988.

[91] Bilaç, O., Dursun, G.M. & Duran, C., "Processing and properties of nanohBN-added glass/ceramic composites for low-temperature co-fired ceramic applications," Journal of the Korean Ceramic Society, 59(2), 283-290, 2022.

CURRICULUM VITAE

PERSONAL INFORMATION

Name Surname : Başak ÖZGÜR

Date of Birth :

Phone :

E-mail :

EDUCATION

High School : **Kırkkonaklar Anadolu Lisesi**

Bachelor : **Ankara Yıldırım Beyazıt University,** Ankara, Turkey, Metallurgical and Materials Engineering

Master Degree : **Ankara Yıldırım Beyazıt University,** Ankara, Turkey, Materials Engineering

WORK EXPERIENCE

Year Corporation Position

2019- Turkish Aerospace Inc. NDT Process Engineer

TOPICS OF INTEREST

- Ceramic Materials
- Powder synthesis
- Composite Materials
- NDT Methods

PRESENT ORGANIZED SOURCES / PRESENTATION

5th International Conference on Engineering Sciences (2019). Production of Aluminum Borate and Aluminum Borate- Mullite Ceramics for Radome Applications. Ankara, TURKEY: Başak ÖZGÜR